Upsilon Spectroscopy and Leptonic Decays using Fully Unquenched Lattice QCD

Thesis submitted to the University of Glasgow

for the degree of Doctor of Philosophy

Alan Gray

Department of Physics and Astronomy

University of Glasgow

September 2003

for my new wife Fiona

Acknowledgements

I would like to thank my supervisor Christine Davies for her help and support throughout my Ph.D. and I also greatly appreciated the helpful discussions I have had with the other Glasgow PPT staff (Mark, Gordon, David, Andrew, Colin, Sandy and Ron) and my collaborators at Cambridge, Edinburgh, Cornell, SFU and OSU.

Additionally, I would like to thank the Glasgow postdocs (Sara, Gunnar, Eduardo, and Martin) and my fellow students (Laurence, Greig, Jack, Pete, Jo, Ian, and Alessandro) for all the assistance they have given me during my research.

I want also to thank my family for their support and Fiona for, amongst everything else, the organisation of the rest of my life for the last 4 months without which I would not have finished on time.

Declaration

With the exception of chapters 1 and 2, all work in this thesis was composed by the author unless otherwise stated.

Abstract

The theory of Non Relativistic QCD (NRQCD) is used to obtain the bottomonium spectrum on configurations (snapshots of the vacuum on the lattice) which incorporate 2+1 flavour of dynamical quarks, where 1 flavour is at around the strange quark mass and the other 2 flavours vary from around the strange quark mass to around one fifth of the strange quark mass. These configurations were provided by the MILC collaboration. Comparison is made to quenched (where dynamical quarks are absent from the theory) and 2 flavour results also on MILC configurations, and to experiment.

Correlation functions are fitted using new Bayesian multi-correlation fitting methods yielding energies and amplitudes. The lattice spacing (which in a correct theory should have only one value no matter how it is determined) is determined using both the $h_b(1P) - \Upsilon(1S)$ and $\Upsilon(2S) - \Upsilon(1S)$ energy splittings. These different determinations show clear signs of convergence with unquenching. The lattice spacing is determined using the static quark potential also and the results agree with those from the Υ spectroscopy provided that the parameter $r_0 = 0.466(9)$fm.

Values are given for radial and orbital splittings, including a result for the recently observed ${}^3D_2$ state. Excellent agreement with experiment is observed in the unquenched case. Results are given for the hyperfine splitting, in the form of the ratio of the 1st excited state of the Υ to that of the ground state.

A value for the strong coupling constant in the $\overline{MS}$ scheme is obtained using the Υ lattice spacing determinations and a comparison of a lattice determination of the plaquette (the shortest closed loop of gluon fields on the lattice) with its third order perturbative expansion.

Results are given for the leptonic width (width of decay to leptons), also in the form of the ratio of the 1st excited state of the Υ to that of the ground state. The unquenched result is still some way from experiment.

Details of a calculation to perturbatively match the heavy-heavy annihilation currents from lattice NRQCD to the continuum, which will enable results for absolute values of the leptonic width, are given along with results for a simpler preliminary calculation.

Contents

List of Figures

List of Tables

Chapter 1

Introduction

1.1 Motivation and Overview

The present understanding of particle physics is classed in what is called The Standard Model. The Standard Model states that the basic building blocks of matter, the quarks and leptons, exist along with their antiparticles and interact through 3 different types of force carriers: electromagnetic, strong, and weak. The particles have a wide range of masses. In particular, the u and d quarks are the lightest quarks at a few MeV/c^2, followed by the s at around 150MeV/c^2, the c at 1.5GeV/c^2, the b at 4.7GeV/c^2 and finally the t at 176GeV/c^2.

Many successful calculations have been done to high accuracy using quantum field theory [1, 2] to test the Standard Model with a method known as perturbation theory. This involves using an expansion in the coupling constant of the theory. For these calculations to succeed, the coupling constant must be small (e.g. for processes involving the electromagnetic force or the strong force at high energies). However, for calculations involving hadrons (bound states of quarks and/or antiquarks) perturbation theory is not permitted. This is because in these situations the strong force dominates while the coupling constant of its governing theory, Quantum Chromodynamics, is large.

Lattice QCD is the only first principles non-perturbative method for solving the equations of QCD. Although invented in the 1970s, it has only relatively recently been utilised for calculations of physical quantities. This is due to the fact that its statistical methods are extremely computationally expensive and only now with present day supercomputing resources can calculations be done reliably. Much work is done in the field to optimise (in the CPU time sense) such calculations and to determine the systematical errors involved with such optimisations. With recent developments it is now becoming possible to do calculations and obtain answers accurate to the required level of a few % in the extraction of the elements of the Standard Model Cabbibo-Kobayashi-Maskawa (CKM) matrix (which relates the mass and weak eigenstates for quarks).

This determination is presently of high importance in physics as it may well highlight a discrepancy of the Standard Model with experiment in the area of CP violation [3, 4].

The operator C replaces particles with their antiparticle equivalent, and the operator P reverses spatial coordinates. The laws of physics are known not to be symmetric under both C and P transformations, otherwise the amounts of antimatter and matter in the universe, thought to be equal at the big bang, would still be equal.

The Standard Model CKM matrix incorporates a mechanism for allowing this symmetry breaking but this provides nowhere near enough CP violation to account for cosmological arguments such as the extent of baryogenisis. It is widely thought that the amount of CP violation allowed by the Standard Model may be less than what is observed.

The CKM elements cannot be measured directly but must be extracted from experiment. In particular, the decay rate of B mesons (hadrons containing as valence particles a heavy b or $\bar{b}$ (anti b) and a light quark), gives a good handle on the CKM parameters. For the extraction, a lattice calculation must be done to account for the behaviour of the quarks as they are bound inside the meson by the strong force.

To confirm the validity of the CKM calculations, it is important to do other similar calculations which can be easily experimentally verified. In fact, the experimental group based in Cornell have designed the CLEO accelerator program specifically to obtain accurate experimental results for lattice comparison [5, 6].

Spectroscopy in the bottomonium system is an excellent area where such comparisons can be done. A bottomonium meson is a bound state of b and $\bar{b}$. Bottomonium spectroscopy is relatively simple to perform since the quarks in the meson can be treated nonrelativistically greatly reducing the complexity of the calculations and enabling precise results. Precise experimental measurements of the bottomonium spectrum already exist, allowing good comparison to experiment for the results presented in this thesis.

In this thesis, I will show how the quantum field theory of the strong force, Quantum Chromo Dynamics (QCD) can be applied using techniques of lattice field theory to calculate such experimentally comparable quantities and will present results from doing so.

1.2 Quantum Field Theory

In 1948, Feynman showed that a *path integral* approach can be used to calculate the expectation values of all the physical observables of a quantum field theory [7] [1]. This is done via the computation of *correlation functions* which are time ordered products of the fields in the theory. This approach is based on the fundamental postulate of quantum mechanics stating that when determining a physical quantity, one must include contributions from all possible paths and fields of the theory.

Let $\phi(x)$ represent the degrees of freedom of a theory at the arbitrary spacetime point x. Then the correlation function $\langle 0|T(\phi(x_1)\cdots\phi(x_n))|0\rangle$ is given in the path integral formulation as

$$\langle 0|T(\phi(x_1)\cdots\phi(x_n))|0\rangle = \frac{1}{Z}\int(\mathcal{D}\phi)\phi(x_1)\cdots\phi(x_N)e^{iS}, \tag{1.1}$$

where $T(\cdots)$ denotes time-ordering, N is the number of fields in the theory and the partition function Z is defined as

$$Z = \int(\mathcal{D}\phi)e^{iS}, \tag{1.2}$$

where S is the *action* of the theory. The *Lagrangian density* of the theory, $\mathcal{L}(\phi_r, \partial_\mu\phi_r)$, relates to the action via

$$S = \int d^4x\mathcal{L}(\phi_r, \partial_\mu\phi_r). \tag{1.3}$$

The path integral $\mathcal{D}\phi$ is over all values of $\phi(x)$ over all values of x, and is hence over an infinite number of degrees of freedom since spacetime is continuous. The theory must be

[1] In this, Feynman states in reference to his path integral formulation that 'there is always the hope that the new point of view will inspire an idea for the modification of present theories, a modification necessary to encompass experiment.' It is interesting to note that this thesis contains experimentally comparable results using the Lattice approach which is entirely based on the path integral formulation.

regularised to remove these infinities before calculations can proceed. In this thesis, the theory of Quantum Chromo Dynamics (QCD) is regularised using Lattice Field Theory. Physical observables are computed via the calculations of QCD correlation functions.

1.2.1 The QCD Lagrangian

In the Standard Model, members of the special class of theories called *gauge theories* are used to describe the fundamental interactions between particles. The Lagrangian of the theory is constructed by demanding that the theory is symmetric under *gauge transformations*. These gauge symmetries are treated using mathematical *group theory*, with the Standard Model electrodynamic, weak, and strong forces each being formulated using a certain mathematical group.

The gauge theory of the strong force is QCD [1, 2, 8, 9, 10] which is based on the SU(3) gauge group of phase transformations on the quark colour fields. The QCD Dirac Lagrangian for non interacting fermions is

$$\mathcal{L} = \bar{\Psi}^i(x)(i\gamma^\mu\partial_\mu - m)\Psi^i(x), \tag{1.4}$$

where $i = 1, 2, 3$ denotes the colour of the quark field, and $\mu = 0 \cdots 3$ is the usual Minkowski spacetime index, Ψ is a 4-component spinor and the adjoint field $\bar{\Psi}(x)$ is given by

$$\bar{\Psi}(x) = \Psi^\dagger(x)\gamma^0. \tag{1.5}$$

Varying the action integral Eqn. 1.3 independently with respect to the fields of the theory leads to the *Euler-Lagrange* equations [1]

$$\frac{\partial\mathcal{L}}{\partial\phi_r} - \frac{\partial}{\partial x^\alpha}\frac{\partial\mathcal{L}}{\partial\phi_{r,\alpha}} = 0,\ \ r = 1, ...N. \tag{1.6}$$

These are the classical equations of motion of the fields. In the case of QCD, they lead to the Dirac equations

$$\begin{aligned}(i\gamma^\mu\partial_\mu - m)\Psi^i(x) &= 0, && (1.7)\\ (i\gamma^\mu\partial_\mu + m)\bar{\Psi}^i(x) &= 0. && (1.8)\end{aligned}$$

To extend this theory to include interactions, it is demanded that $\mathcal{L}$ is invariant under local phase transformations.

Let $\lambda^a : a = 1\cdots 8$ be the Gell Mann matrices; the generators of the fundamental representation of SU(3). They are then a set of linearly independent traceless 3×3 matrices satisfying the commutation relations

$$\left[\frac{\lambda_i}{2}, \frac{\lambda_j}{2}\right] = i f_{ijk}\frac{\lambda_k}{2} \tag{1.9}$$

where f_{ijk} are the structure constants of QCD [10]. The Gell Mann matrices are normalised such that

$$\mathrm{Tr}\lambda_i\lambda_j = 2\delta_{ij}. \tag{1.10}$$

Let $\alpha_a(x) : a = 1\cdots 8$ be arbitrary SU(3) group parameters. Then, dropping the colour indices on the quark fields, under the local phase transformation

$$\Psi(x) \to \Psi'(x) \equiv e^{i\alpha_a(x)\frac{\lambda^a}{2}}\Psi(x), \tag{1.11}$$

$$\bar{\Psi}(x) \to \bar{\Psi}'(x) \equiv \bar{\Psi}(x)e^{-i\alpha_a(x)\frac{\lambda^a}{2}}, \tag{1.12}$$

the Lagrangian transforms as

$$\mathcal{L} \to \mathcal{L}' = \mathcal{L} - \bar{\Psi}\gamma^\mu\frac{\lambda^a}{2}\Psi\partial_\mu\alpha_a(x). \tag{1.13}$$

The extra term is cancelled by the introduction of 8 vector Yang Mills gauge fields

$$A_\mu = A_\mu^a\frac{\lambda_a}{2} \;\; (= (\phi, \mathbf{A})) \tag{1.14}$$

and the covariant derivative

$$D_\mu = \partial_\mu - igA_\mu, \tag{1.15}$$

where g is the coupling of the theory. Then the Lagrangian

$$\mathcal{L} = \bar{\Psi}(x)(i\gamma^\mu D_\mu - m)\Psi(x) \tag{1.16}$$

is invariant under the transformation Eqns. 1.11-1.12 if A_μ transforms as

$$A'_\mu \equiv A_\mu - \frac{i}{g}\partial_\mu\alpha_a(x). \tag{1.17}$$

To obtain propagating gauge fields, the field-strength tensor $F_{\mu\nu} = F^a_{\mu\nu}\frac{\lambda_a}{2}$ is defined as [8]

$$F_{\mu\nu} = \partial_\mu A_\nu - \partial_\nu A_\mu - ig[A_\mu, A_\nu] \tag{1.18}$$

and the kinetic term

$$\mathcal{L}_K = -\frac{1}{4}F_{\mu\nu}F^{\mu\nu} \tag{1.19}$$

is added to give the final QCD Lagrangian

$$\mathcal{L} = \bar{\Psi}^i(x)(i\gamma^\mu D_\mu - m)\Psi^i(x) - \frac{1}{4}F_{\mu\nu}F^{\mu\nu}. \tag{1.20}$$

This Lagrangian is of course gauge invariant but it is often useful to *fix the gauge* by way of imposing constraints on the field A_μ. Several gauges, defined by the constraints imposed, are commonly used and those particular to work in this thesis are the *Coulomb Gauge* defined by the constraint

$$\partial_i A_i = 0, \tag{1.21}$$

where i represents the spatial indices only, and the *Landau gauge*

$$\partial_\mu A_\mu = 0. \tag{1.22}$$

1.2.2 Consequences of the Nature of QCD

One consequence of the nature of QCD is the phenomenon of *confinement* - quarks are confined into colourless bound states called *hadrons* by virtual gluon exchange. Confinement explains why no object with an overall colour charge has ever been observed.

Colourless combinations of quarks can be formed by either the binding of 3 quarks each possessing a separate one of the 3 colour charges or a coloured quark bound to an antiquark charged with the appropriate anticolour. These hadrons are known as *baryons* and *mesons* respectively.

Another important QCD feature is the phenomenon of *asymptotic freedom.* In contrast to QED where the coupling of the theory decreases as distance increases, the coupling of QCD decreases as the distance *decreases.* This results in quarks becoming free particles at high energies.

In QED, perturbation theory, a method of calculation involving an expansion in the coupling of the theory about the free field solutions, has been used to great effect in calculating many quantities, for example the anomalous magnetic moments of the electron [11] and muon [12]. Perturbation theory is made possible in QED because the coupling of the theory $\alpha_{em} \sim \mathcal{O}(1/137)$. However as a consequence of asymptotic freedom in QCD, although perturbation theory can be used for processes involving large momenta (small distances), at the energies of bound states the coupling of QCD $\alpha_S \sim \mathcal{O}(1)$ and perturbation theory is not applicable. A non-perturbative approach is required, and the only such approach is to use the numerical methods of Lattice QCD.

1.2.3 Continuation from Minkowski to Euclidean Space

Unfortunately, the imaginary exponents in Eqn. 1.1 and Eq. 1.2 result in oscillations which make numerical simulations impossible. However, we can perform an *Wick Rotation*, which is an analytic continuation into imaginary time, which removes these oscillations.

A quantum field theory is defined on a certain spacetime geometry specified by the metric tensor $\eta_{\mu\nu}$ [1]. Up to this point the Minkowski metric

$$\eta^{(M)}_{\mu\nu} = \mathrm{diag}(1, -1, -1, -1) \tag{1.23}$$

has been used. Under a Wick rotation, the $(0, 0)$ component of the Minkowski metric is negated giving the (identity matrix) Euclidean metric

$$\eta^{(E)}_{\mu\nu} = \mathrm{diag}(1, 1, 1, 1). \tag{1.24}$$

The following relations relate Euclidean quantities to their Minkowski form;

$$x^0_{(M)} = -ix^4_{(E)} \tag{1.25}$$

$$\partial^0_{(M)} = i\partial^0_{(E)} \tag{1.26}$$

$$D^0_{(M)} = iD^4_{(E)} \tag{1.27}$$

$$\gamma_{0(M)} = \gamma_{4(E)} \tag{1.28}$$

$$\gamma_{i(M)} = -i\gamma_{i(E)} \tag{1.29}$$

$$A^0_{(M)} = -iA^4_{(E)}. \tag{1.30}$$

Then, the Lagrangian in Eq. 1.20 becomes

$$\mathcal{L}^{(E)} = \bar{\Psi}(x)(\gamma^\mu D_\mu + m)\Psi(x) - \frac{1}{4}F_{\mu\nu}F^{\mu\nu} \tag{1.31}$$

and Eq. 1.1 and Eq. 1.2 become

$$\langle 0|T(\phi(x_1)\cdots\phi(x_n))|0\rangle^{(E)} = \frac{1}{Z}\int(\Pi\mathcal{D}\phi)\phi(x_1)\cdots\phi(x_n)e^{-S^{(E)}}, \tag{1.32}$$

$$Z^{(E)} = \int(\Pi\mathcal{D}\phi)e^{-S^{(E)}} \tag{1.33}$$

respectively, allowing numerical simulations to proceed.

For the rest of this chapter, all quantities will be in Euclidean space with the (E) label dropped.

1.3 Lattice QCD

Equation 1.1 involves path integrations over a continuously infinite number of degrees of freedom (every point of spacetime) and therefore it must be regularised.

Wilson first showed in 1974 [13] that such regularisation can proceed via the method of lattice QCD [14, 15, 16, 17, 18] in which spacetime is discretised onto a finite hypercubic lattice Λ of points with spacing a:

$$\Lambda = \{x \in a\mathbb{Z}^4 | \frac{x^{1,2,3}}{a} = 0,\cdots,L-1; \frac{x^4}{a} = 0,\cdots,T-1\} \tag{1.34}$$

Figure 1.1: The lattice link fields $U_\mu(x)$ from site x to $x + a\hat{\mu}$ and $U_\mu^\dagger(x)$ from $x + a\hat{\mu}$ to x.

Thus, the fields $\Psi(x)$ are defined only on the lattice points

$$x_i = na, n = 0, \cdots, L-1 \tag{1.35}$$

$$x_4 = ma, m = 0, \cdots, T-1 \tag{1.36}$$

and derivatives become finite differences[2]

$$\partial_\mu \Psi(x) \to \frac{1}{2a}(\Psi(x + a\hat{\mu}) - \Psi(x - a\hat{\mu})). \tag{1.37}$$

It is convenient to define forward and backward lattice derivatives

$$\nabla_\mu \Psi(x) = \frac{1}{a}(\Psi(x + a\hat{\mu}) - \Psi(x)) \tag{1.38}$$

$$\nabla_\mu^* \Psi(x) = \frac{1}{a}(\Psi(x) - \Psi(x - a\hat{\mu})) \tag{1.39}$$

and the lattice Laplacian

$$\Delta\Psi(x) \equiv \sum_\mu (\nabla_\mu^* \nabla_\mu)\Psi(x). \tag{1.40}$$

1.3.1 Lattice Gauge Fields

The continuum QCD gauge field A_μ from Eqn. 1.14 is transcribed to the lattice in a more subtle way than fermion field discretisation. The definition of the lattice gauge field is motivated by the fact that, in the continuum, a fermion moving from spacetime point x to y in the presence of gauge field $A_\mu(x)$ picks up the phase factor

$$\mathcal{P} e^{ig \int_y^x A_\mu dx^\mu}, \tag{1.41}$$

[2]Gluon fields should be present in these derivatives to allow coupling from quarks to gluons, but this is neglected until later for simplicity

where $\mathcal{P}$ denotes path ordering.

Lattice gauge fields are thus defined in terms of a discrete version of the above path ordered product; the $SU(3)$ *parallel transport* fields

$$U(x, x+\hat{\mu}) = U_\mu(x) = e^{iagA_\mu(x+a\hat{\mu})}. \tag{1.42}$$

The field $U_\mu(x)$ is associated with the link from the site x to the site $x + a\hat{\mu}$. The field $U_\mu^{(-1)}(x) = U_\mu^{(\dagger)}(x)$ (U is unitary) is then associated with the link from $x + a\hat{\mu}$ to x (see Figure 1.1).

In undergoing a gauge transformation,

$$U_\mu(x) \quad \rightarrow \quad U_\mu^g(x) = G(x)U_\mu G^{-1}(x + a\hat{\mu}) \tag{1.43}$$

$$\psi(x) \quad \rightarrow \quad \psi^g(x) = G(x)\psi(x) \tag{1.44}$$

$$\overline{\psi}(x) \quad \rightarrow \quad \overline{\psi}^g(x) = \overline{\psi}(x)G^{-1}(x) \tag{1.45}$$

where $G \in SU(3)$. Then any closed string of U fields on the lattice is gauge independent as is any string with a quark at one end and an antiquark at the other (see e.g. Figure 1.2).

The pure gauge part of the action should then be written in terms of closed loops of U fields. It is most common to use the *Wilson gauge action*

$$S_G = \beta \sum_p \left(1 - \frac{1}{3}\text{Re}[\text{Tr}U_p]\right), \tag{1.46}$$

where $\beta = \frac{6}{g^2}$ and U_p is a *plaquette* which is an $SU(3)$ matrix formed by sequentially multiplying the U fields which form the smallest possible closed loops on the lattice (see figure 1.3). In the continuum limit ($a \rightarrow 0$), S_G tends to the continuum form

$$\frac{1}{4}\int d^4x F_{\mu v}F^{\mu v}. \tag{1.47}$$

1.3.2 Improvement

Symanzik's Improvement Program

In the early 1980s Symanzik showed [19] that lattice theories could be described by an effective continuum theory with the action

$$S_{eff} = \int d^4x \sum_{k=0}^{\infty} a^k \mathcal{L}_k(x), \tag{1.48}$$

where $\mathcal{L}_0$ is the continuum QCD Lagrangian, and $\mathcal{L}_k$, $k > 0$ are linear combinations of local operators of dimension $4 + k$. This explicitly shows the lattice spacing dependence of the lattice theory. Symanzik proposed that the theory be improved by adding irrelevant operators to the action such to cancel terms dependent on the lattice spacing which essentially accelerates the theory toward the continuum limit.

Of course, of all possible higher order ($k > 0$) terms, only those possessing the symmetries of the lattice action will appear in 1.48.

Improved Gauge Action

The Wilson gauge action 1.46 (as does any lattice action written as a linear combination of Wilson loops) tends to the correct continuum form as $a \to 0$ but at finite lattice spacing errors appear at $\mathcal{O}(a^2)$.

As is discussed in [20], these $\mathcal{O}(a^2)$ errors can be romoved by the addition of two six link Wilson-loop terms; the first a rectangle U_{rt} and the second a 'parallelogram' U_{pg}. Then the improved Wilson action becomes

$$\begin{aligned} S_G &= \beta \sum_p \left(1 - \frac{1}{3}\mathrm{Re}[\mathrm{Tr} U_p]\right) \\ &+ \beta_{rt} \sum_p \left(1 - \frac{1}{3}\mathrm{Re}[\mathrm{Tr} U_{rt}]\right) \\ &+ \beta_{pg} \sum_p \left(1 - \frac{1}{3}\mathrm{Re}[\mathrm{Tr} U_{pg}]\right) \end{aligned} \tag{1.49}$$

The couplings β_{rt} and β_{pg} then can be determined by enforcing the results of a calculation using the improved action to match the continuum results.

Since the improvement terms are needed due to the lattice cutoff, they must be due to QCD physics at large momenta, $p > \pi/a$ and can be determined using perturbation theory. Highly improved gauge actions need perturbative calculations for these coefficients not just to tree-level but to one-loop order and beyond.

Perturbation Theory and Tadpole Improvement

Lattice perturbation theory is essential in accounting for phenomena due to the physics at distance scales shorter that the lattice spacing.

A naive perturbative expansion would be in terms of the bare lattice coupling $\alpha_{latt} \equiv g^2_{lat}/4\pi$. However, experience has shown that such expansions tend to be poor [21] .

It has been proven better to expand in terms of a better defined coupling such as the coupling α_V defined in terms of the static quark potential

$$V_{QQ}(q) = -4\pi C_F \frac{\alpha_V(q)}{q^2}. \tag{1.50}$$

since this can be directly related to a similar coupling in the continuum.

The reason that α_V expansions work better is that α_{latt} is too small, especially at small lattice spacings. For example, for lattice spacings smaller than 1fm, α_{latt} is around half the size of α_V, and expansions in α_{latt} at this scale badly underestimate perturbative effects causing the expansions to converge poorly.

The small bare lattice coupling is a symptom of the 'tadpole contributions' which are present in the lattice theory but not the continuum [22].

These arise due to the presence of higher order terms in the exponential in Eqn. 1.42 which result in vertices between quarks and multiple gluons, whereas only a single quark can couple to a gluon in the continuum. These extra lattice theory vertices are not suppressed by powers of the lattice spacing as would be expected since gluons coupled to one another generate ultraviolet divergent factors of $1/a^2$. Therefore these tadpole contributions cause large renormalisations and spoil naive perturbation theory. However, they can be cancelled out with the procedure of *tadpole improvement.*

Let the 'mean link' u_{0L} be defined as

$$u_{0L} = \overline{\frac{1}{3}\mathrm{ReTr}U_\mu} \tag{1.51}$$

in the Landau gauge, where such a gauge has been chosen for its smooth properties. u_{0L} consists entirely of tadpoles, so if we divide every link by u_{0L};

$$U_\mu \to \frac{U_\mu}{u_0}, \tag{1.52}$$

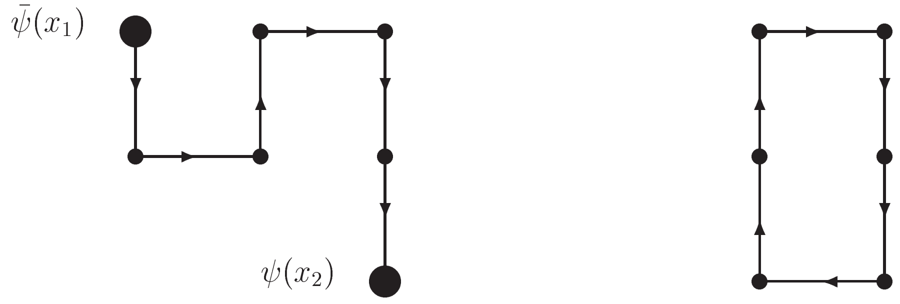

Figure 1.2: Gauge independent quantities on the lattice; a string of U_μ fields terminated by quarks (left) and a closed (Wilson) loop of U_μ fields.

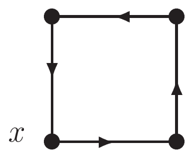

Figure 1.3: The smallest Wilson loop on the lattice, a *plaquette*.

where u_0 is computed in a simulation, the tadpole contributions largely cancel.

An alternative convention is to take u_0 from the fourth root of the measurement of the plaquette:

$$u_0 =< \frac{1}{3}\mathrm{Tr}U_{plaq} >^{1/4} . \tag{1.53}$$

The Landau link and plaquette conventions for tadpole improvement have been compared by means of several tests in [23] and the Landau convention performed favourably, particularly for tests involving the scaling of hyperfine splittings which will be important in this work.

1.3.3 Monte Carlo Simulations for Gluons

After lattice quantisation, when only considering gauge fields, Eqn. 1.1 becomes

$$\langle \mathcal{O} \rangle = \frac{\int [\mathcal{D}U_\mu] \mathcal{O} e^{-S_g(U)}}{Z}, \tag{1.54}$$

$$Z = \int [\mathcal{D}U_\mu] e^{-S_g(U)} \tag{1.55}$$

where $\mathcal{O}$ is a correlation function consisting of U fields and $\mathcal{D}U_\mu = \prod_{x\in\Lambda} dU_\mu(x)$. Thus the integration is now over a finite number of degrees of freedom.

A numerical approach in solving 1.54 is stimulated by the similarities that the system has with the theory of classical statistical mechanics (for a good comparison, see [17]).

If N_{conf} configurations of U fields are created randomly equation 1.54 can be calculated numerically as

$$\langle \mathcal{O} \rangle = lim_{N_{conf}\to\infty} \frac{\sum_{conf} \mathcal{O} e^{-S_g}}{\sum_{conf} e^{-S_g}}. \tag{1.56}$$

However, the sum is strongly peaked around configurations which minimise S so it makes economical sense to use *importance sampling* to, instead of randomly create configurations, create an *ensemble* of configurations with probability distribution e^{-S_g}. Then

$$\langle \mathcal{O} \rangle = lim_{N_{conf}\to\infty} \frac{1}{N_{conf}} \sum_{conf} \mathcal{O}, \tag{1.57}$$

where the sum is over the N_{conf} configurations. Thus observables are, in analogy to experimental analysis, *measured* as the ensemble average. Of course, in practice these ensembles must be finite so a statistical error is introduced which is proportional to $1/\sqrt{N_{conf}}$.

This Monte Carlo method involves generating configurations $\mathcal{C}$ with likelihood

$$P(\mathcal{C}) = e^{-S_g(C)}. \tag{1.58}$$

For illustration, the straightforward *Metropolis* algorithm follows the procedure [24]:

- begin with a certain $\mathcal{C}$
- suggest a random slight change $\mathcal{C} \to \mathcal{C}'$
- compute $S(\mathcal{C})$ and $S(\mathcal{C}')$

- randomly generate $R \in [0,1]$ and accept the new $\mathcal{C}$ as part of the ensemble if and only if

$$R \leq \frac{e^{-S(C')}}{e^{-S(C)}} \tag{1.59}$$

- go back to 1st step (with $\mathcal{C}$ replaced by $\mathcal{C}'$ if accepted)....

The Metropolis algorithm works well for configurations of, say, $U(1)$ fields but is slow in dealing with SU(3) fields and other more elaborate algorithms must be used, as is discussed in section 1.3.7.

1.3.4 Discretisation of Fermion Fields

Naive Quarks

The Lattice formulation of quark fields is unfortunately much less straightforward than for gauge fields. Straightforward discretisation of the Dirac Lagrangian Eqn. 1.31 leads to the *naive fermion lattice action*

$$S_N[\Psi, \bar{\Psi}] = a^4 \sum_x \bar{\Psi}(x) M \Psi(x) \tag{1.60}$$

where

$$M = \frac{1}{2}\gamma_\mu(\nabla_\mu + \nabla^*_\mu) + m_0. \tag{1.61}$$

This discretisation preserves *chiral symmetry*, the invariance of the action under

$$\begin{aligned} \Psi(x) &\rightarrow e^{i\theta\gamma_5}\Psi(x) \\ \bar{\Psi}(x) &\rightarrow \bar{\Psi}(x)e^{i\theta\gamma_5} \end{aligned} \tag{1.62}$$

in the massless limit $m_0 = 0$, where θ is a global parameter.

However, this discretisation has a fundamental problem. The Fourier transform of this action is given by by

$$\tilde{\Psi}(p) = a^4 \sum_x e^{-ipx}\Psi(x) \tag{1.63}$$

$$S_N = \frac{1}{(2\pi)^4}\int_{-\pi/a}^{\pi/a} d^4p \bar{\tilde{\Psi}}(p)(i\gamma^\mu \frac{\sin p_\mu a}{a} + m)\tilde{\Psi}(p) \tag{1.64}$$

The inverse of the propagator $G(x-y) = \langle|\overline{\psi}(x)\psi(y)|\rangle$ in momentum space in the free field case can be obtaied via

$$S_N = \frac{1}{(2\pi)^4}\int_{-\pi/a}^{\pi/a} d^4p\tilde{\bar{\Psi}}(p)G^{-1}(p)\tilde{\Psi}(p). \tag{1.65}$$

Thus, on the lattice this is given by

$$G^{-1}_{latt}(p) = i\gamma^\mu \frac{\sin p_\mu a}{a} + m \tag{1.66}$$

compared to the continuum

$$G^{-1}_{cont}(p) = i\gamma^\mu p_\mu + m. \tag{1.67}$$

Particle masses are defined through the poles of the propagator, i.e. on the lattice near $\frac{1}{a}sin(ap_\mu) = 0$ for $m_0 << p_\mu$. This condition is satisfied as expected for $p_\mu = 0$ but also for $p_\mu = \pi/a$. Thus, in the 4 dimensional theory there are $2^4 = 16$ poles instead of 1, leading to 16 degenerate quarks, or *doublers*. Since this degeneracy is not physical and merely an artifact of discretisation, the doublers are not distinguished as different physical flavours but instead referred to as different *tastes*. There are 16 degenerate tastes for every continuum flavour.

In reality, there are only 2 quarks, u and d, which because of their similar masses could be with any degree of accuracy treated as being degenerate. Much of the work done in Lattice QCD involves dealing with this problem whilst retaining, to the maximum possible degree, the symmetries of the continuum theory.

1.3.5 Wilson Quarks

Wilson proposed [25] adding an extra term to the naive action which vanishes as $a \to 0$ such that the quark operator transforms as

$$M \to M_W \equiv \frac{1}{2}\gamma_\mu(\nabla_\mu + \nabla^*_\mu) + m_0 - \frac{ra}{2}\nabla^*_\mu\nabla_\mu, \tag{1.68}$$

where the Wilson parameter r is usually set to 1. Then the quark propagator becomes, after expanding the sin function around $p \approx 0$,

$$G^{-1}_W(p) = i\gamma^\mu p_\mu + m + \frac{ra}{2}\sum_{\nu=1}^{4} p^2_\nu. \tag{1.69}$$

Therefore, as $a \to 0$ the fermion of mass m will have the right form. However, for the doublers we expand the sin function around $p \approx \pi/2$. For a doubler which has one component of momentum close to π/a and the others close to 0, we get

$$G_W^{-1}(\tilde{p}) = i\gamma^\mu \tilde{p}_\mu + m + \frac{2r}{a} + \cdots \tag{1.70}$$

where $\tilde{p}$ is the momentum difference between p and π/a. Thus as $a \to 0$ the doubler's mass tends to infinity decoupling the particle from the theory. This occurs for all the 15 doublers.

The quark fields are rescaled $\Psi \to a^{3/2}\Psi$. This makes the quark action dimensionless and the value of a is not known until after the simulation when a physical quantity is fixed to experiment. The action becomes

$$S_f^W = \sum_x \{\bar{\Psi}(x)[(\gamma^\mu - r)\Psi(x + a\hat{\mu}) - (\gamma^\mu + r)\Psi(x - a\hat{\mu})] + (ma + 4r)\bar{\Psi}(x)\Psi(x)\}. \tag{1.71}$$

The *hopping parameter* κ is defined as

$$\kappa = \frac{1}{2ma + 8r}. \tag{1.72}$$

The quark fields are rescaled by $\sqrt{2\kappa}$ and U fields are included as links between quark fields to allow interactions. The Wilson fermion action then becomes

$$S_f^W = \sum_x \{\kappa[\bar{\Psi}(x)(\gamma^\mu - r)U_\mu(x)\Psi(x + a\hat{\mu})\bar{\Psi}(x + a\hat{\mu})(\gamma^\mu + r)U_\mu^\dagger(x)\Psi(x)] + \bar{\Psi}(x)\Psi(x)\}. \tag{1.73}$$

However, this 'fix' is far from ideal because the inclusion of the Wilson term explicitly breaks the chiral symmetry (Eqn. 1.62) of the naive action. In fact, Nielson and Ninomiya showed in their *no go theorem* [26] that it is impossible to define a local hermitian lattice theory which has no doublers and is chirally symmetric.

Cloverleaf Fields

To Symanzik improve the Wilson action through $\mathcal{O}(a)$ whilst retaining the fix for doublers, Sheikholeslami and Wohlert proposed adding to S_W another term [27]:

$$S_{SW} = S_W - \frac{iaC_{SW}\kappa r}{4}\bar{\Psi}(x)\sigma_{\mu\nu}F_{\mu\nu}^{cvr}\Psi(x), \tag{1.74}$$

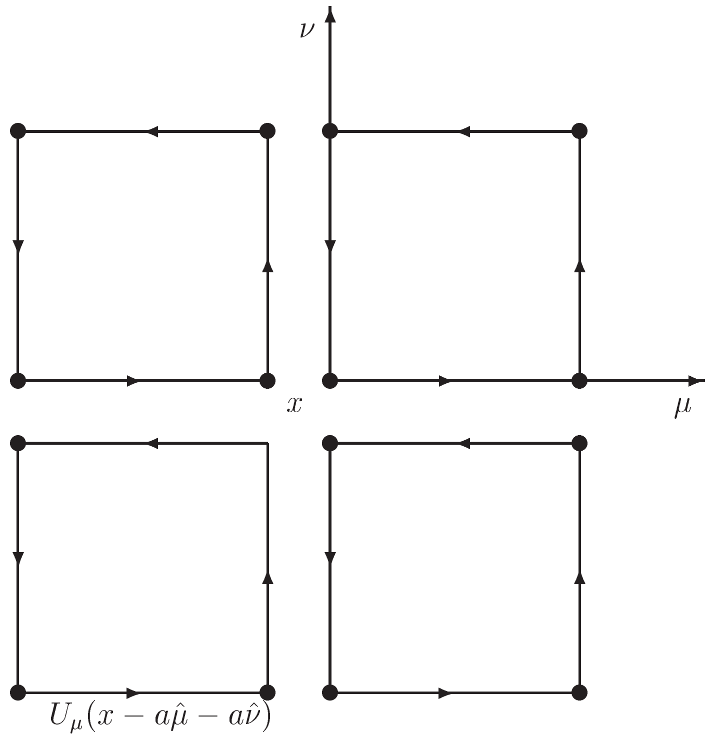

Figure 1.4: A cloverleaf arrangement of U_μ fields on the lattice.

where the coefficient C_{SW} is 1 at tree level but can be calculated beyond tree level perturbatively [28] or non-perturbatively [29]. The cloverleaf operator $F^{cvr}_{\mu\nu}$ is defined as

$$gF^{cvr}_{\mu\nu}(x) = -\frac{1}{4a^2} \sum_{P(x,\nu\mu)} \mathcal{I}[U_{P(x,\mu\nu)}], \tag{1.75}$$

with the sum being over all plaquettes P in the (μ, ν) plane which contains the site x. $I[U_P]$ is defined as

$$I[U_P] \equiv \frac{U_P - U_P^\dagger}{2i} - \frac{1}{3} Im(TrU_P) \tag{1.76}$$

with U_P being the product of U matrices counterclockwise about $\hat{\mu} \times \hat{\nu}$ on P, as in figure 1.4. Eqn. 1.74 is commonly known as the Wilson Clover Action.

1.3.6 Staggered Quarks

An alternative to the Wilson formulation, the *staggered formulation* was proposed first in 1975 by Kogut and Susskind. The doubling problem is treated in the staggered formulation by exploiting the fact that spin-diagonalisation can be used to reduce the degrees of freedom from 16 down to 4 [30, 16].

Staggered fermions $\chi(x)$ relate to the fields $\Psi(x)$ via

$$\Psi(x) = \Gamma_x \chi(x) \tag{1.77}$$

$$\bar{\Psi}(x) = \bar{\chi}(x)\Gamma_x^\dagger \tag{1.78}$$

where

$$\Gamma_x = \gamma_1^{x_1}\gamma_2^{x_2}\gamma_3^{x_3}\gamma_4^{x_4} \tag{1.79}$$

The γ matrices can be replaced by the phases

$$\eta_\mu(x) = (-1)^k; k = \sum_{\nu<\mu} x_\nu \tag{1.80}$$

which do not have a spinor index. Thus the different spin components of χ decouple, and one can drop the spin index on χ leaving only a colour index. The 16-fold degeneracy then reduces to 4-fold. The staggered Kogut-Susskind fermion action becomes

$$S_{KS} = \sum_x \bar{\chi}(x)\{\frac{1}{2}\eta_\mu(x)(U_\mu(x)\chi(x+a\hat{\mu}) - U_\mu^\dagger(x-a\hat{\mu})\chi(x-a\hat{\mu})) + ma\chi(x)\}. \tag{1.81}$$

The resulting degeneracy causes the quark vacuum polarisation loop to over contribute by a factor of 4. Thus, in order to simulate just one quark, the quark determinant in the path integral is replaced by its fourth root. In order to simulate both light quarks (which can be treated degenerately since the difference between their masses is much smaller than any other mass) , the quark determinant in the path integral is replaced by its square root (see section 1.3.7).

This process preserves a continuous $U(1) \times U(1)$ symmetry which is a remnant of the original chiral symmetry Eqn. 1.62 [16].

Improved Staggered Quarks

However, the standard staggered action Eqn. 1.81 allows large flavour changing strong interactions at $\mathcal{O}(a^2)$ which are not present in QCD and thus cause substantial discretisation errors in computed quantities. This is a main reason for the popularity of the alternative Wilson formulation in past calculations.

However, recently an understanding has emerged of these flavour changing interactions and it is now possible to remove them perturbatively, highly improving the staggered formulation.

An alternative way of exposing the quark doubling property of the naive quark action Eqn. 1.68 is to note that it is symmetric under the 'doubling' transformation

$$\begin{aligned} \Psi(x) \to \tilde{\Psi}(x) &\equiv i\gamma_5\gamma_\rho(-1)^{x_\rho/a}\Psi(x) \\ &= i\gamma_5\gamma_\rho e^{ix_\rho\pi/a}\Psi(x), \end{aligned} \tag{1.82}$$

where ρ denotes an arbitrary direction. This clarifies that a mode with low momentum $\Psi(x)$ is equivalent to another mode $\tilde{\Psi}$ with near maximal lattice momentum, $p \approx \pi/a$. This transformation can be carried out successively in 2 or more directions and becomes in general

$$\Psi(x) \to \tilde{\Psi}(x) \prod_\rho (i\gamma_5\gamma_\rho)^{\zeta_\rho} e^{ix.\zeta\pi/a}\Psi(x), \tag{1.83}$$

with ζ a vector with one or more components equal to one and the remaining components zero. Therefore, there are 15 extra modes which are equivalent to the original low momentum mode. These are nothing more than the doublers derived in section 1.3.4 but this new derivation motivates new insights.

A low energy quark which absorbs a momentum $q \approx \zeta\pi/a$ for any of the 15 different ζ will, instead of being forced way off energy-shell, be transformed into a low-energy quark of another taste. This momentum transfer can occur via the emission of a gluon with momentum $q \approx \zeta\pi/a$. This gluon is highly virtual as it has $q^2 = \mathcal{O}((\pi/a)^2)$ and hence must be quickly reabsorbed by another quark which will then also change taste, as in Figure 1.5.

Since this process involves the transfer of high momentum, it can be treated perturbatively, and the 1 gluon exchange process has a larger contribution than the exchange of multiple gluons. These taste-changing interactions do not appear in QCD and are a source of $\mathcal{O}(a^2)$ errors. They can however be calculated perturbatively and removed.

It is shown in [31] that the couplings between the quarks and gluons with momentum π/a can be removed by *fattening* the links to include factors of not just the simple link but

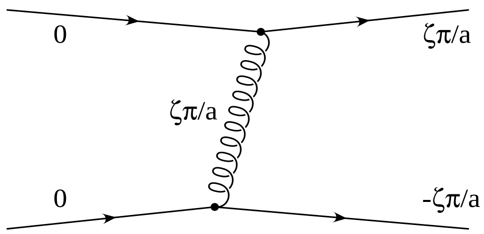

Figure 1.5: A taste changing interaction.

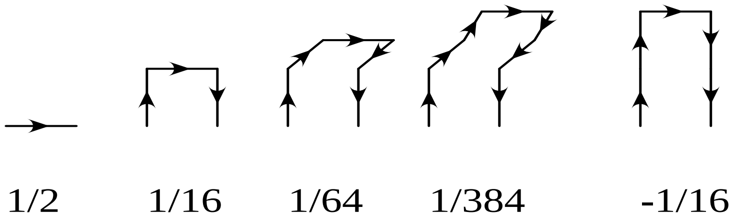

.

Figure 1.6: Illustrations of (from left ot right) a simple link, 3, 5, and 7 link staples and the Naik term complee with weighting coefficients.

three link, five link and seven link staple terms as depicted in figure 1.6. The coefficients of these terms are chosen to remove all combinations of momentum π/a couplings. The final term in figure 1.6 is the so called *Lepage term* which corrects for a low momentum error introduced by the fattening loops [31].

The action is then staggered as in the previous section, giving the *asq action*

$$S = \sum_x \eta_\mu(x)\overline{\chi}(x)(\Delta'_\mu - \frac{1}{6}\Delta^3_\mu)\chi(x) + ma\overline{\chi}(x)\chi(x), \tag{1.84}$$

where Δ' is a fattened link and Δ^3 is the *Naik term* [32] which removes $\mathcal{O}(a^2)$ errors from the derivative. This action can then be tadpole improved by inserting factors of u_0 to give the so called *asqtad action*.

1.3.7 Monte Carlo Simulations Including Quarks

The procedure of section 1.3.3 cannot be followed directly with the inclusion of quarks because the fields Ψ are Grassmann variables and cannot be represented by ordinary numbers

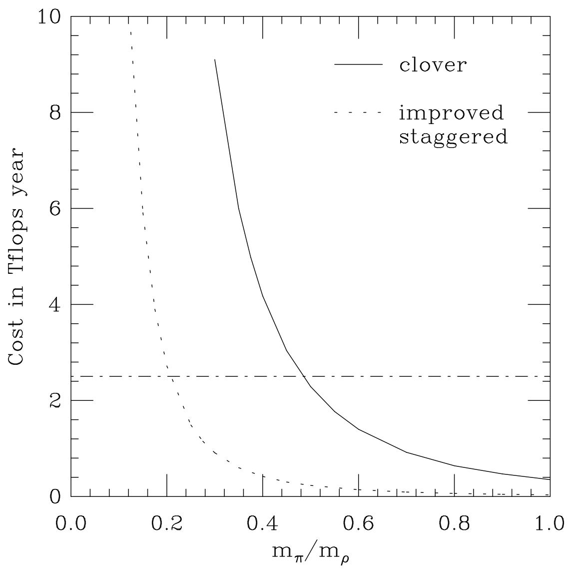

Figure 1.7: The cost in Tflop years, calculated by C.T.H. Davies, of generating an ensemble using Wilson clover quarks (solid line) and improved staggered quarks (dashed line) versus the ratio of pseudoscalar to vector meson mass.

on a computer. These fields can however be integrated analytically:

$$\int dU_\mu d\Psi d\bar{\Psi} e^{-S_g+\bar{\Psi}M(U_\mu)\Psi} = \int dU_\mu \mathrm{det} M(U_\mu) e^{-S_g}. \tag{1.85}$$

Then, the action becomes

$$S = S_G - \ln(\det(M(U_\mu))). \tag{1.86}$$

The Monte-Carlo techniques can then proceed using this action as before. In order to minimise the time taken to create configurations, preferred algorithms differ depending on the form of S. For Wilson clover quarks, the *Hybrid Monte Carlo* [33] is the best choice whilst for improved staggered quarks, the *R Algorithm* [34] is used.

However, the calculation of $\det(M(U_\mu))$ is extremely computationally expensive, and the cost increases as the eigenvalues of M decrease, i.e. as we approach the chiral limit. Simulations are therefore done at dynamical quark masses greater than the physical quark masses, and extrapolations are done to get physically comparable results. The form the extrapolations need to take can be calculated in *chiral perturbation theory* which involves an expansion in the quark mass, but this is only expected to work up to a scale of around $m_s/2$. It is of utmost imporance that the simulations take place at quark masses as low as possible in order to overlap the chiral region so chiral extrapolations to the physical light quark masses can be properly performed.

Figure 1.7 demonstrates the cost increase with decreasing dynamical quark mass but also shows the computational cost advantage of the improved staggered formulation over the Wilson clover alternative by showing that, for example, in 6 months a 5 Tflop (5×10^{12} floating point operations per second) machine will be able to simulate at $m_\pi/m_\rho \sim 0.2$ which is much further toward the physical $m_\pi/m_\rho = 0.181$ and hence much more realistic than the $m_\pi/m_\rho \sim 0.45$ obtainable using the Wilson Clover formulation, where m_π and m_ρ are the masses of the π and ρ mesons with the dynamical light quarks as valence particles. [3]

Staggered quarks have another advantage over their Wilson counterparts. The eigenvalues of the Wilson quark operator are widely spread over the complex plane and include zero modes on any given configuration. This results in numerical difficulties [35]. Staggered quark eigenvalues on the other hand cannot be zero on any finite lattice and are much easier to handle numerically.

Because calculating the highly non-local determinant when updating the Monte-Carlo algorithm is extremely computationally expensive, the *quenched approximation* has had widespread use in the previous years.

1.3.8 Quenching

Lack of computing power has resulted in the use of the quenched approximation in the vast majority of previous simulations, which involves setting $\det M(U_\mu) = 1$ in the action corresponding to ignoring the effects of closed quark loops in the vacuum (called dynamical or sea quarks). This results in a computational saving of a factor of at least 10000. The quenched theory is not physically correct and in undertaking quenched simulations it is important to determine the quenching errors in the results.

[3] This specific cost example was calculated to estimate the potential of the new QCDOC machine destined for Edinburgh Parallel Computing Centre in 2004. Note that this example uses a volume of 3fm so may be too optimistic for the very low quark mass region where a 4fm volume would be more reasonable.

Recently, several calculations have been done in the *partially quenched* approximation, in which the number of dynamical fermions (N_f) included is not the number sufficient to be physically accurate.

In the case of Υ simulations, $N_f = 3$ is sufficient as c, b, t are too heavy to have a noticeable effect and can be ignored [36]. With such Υ simulations, I have performed some of the first fully unquenched calculations (with $N_f = 3$) and the results are presented in this thesis.

1.4 Matching Between Lattice and Continuum

Experimental results are quoted in some continuum renormalisation scheme, most often $\overline{MS}$. To compare lattice results with such experimental data, it is necessary to match between the lattice and continuum at the quark level for currents whose matrix elements are then calculated on the lattice. This can be done either perturbatively or non-perturbatively.

In this thesis, perturbative matching will be done. This involves the perturbative calculation of a specific process in both schemes with the results being fixed to be the same with the introduction of some matching factor Z_{match}.

Chapter 2

Heavy Meson Simulations

2.1 Quark Model Notation For Mesons

Mesons are hadrons containing as valence particles a quark and an antiquark. The valence particles can be thought of as having their spins parallel or anti-parallel to one another, resulting in a *vector* spin 1 or *pseudoscalar* spin 0 meson respectively. Their orbital angular momenta relative to one another can also take different values. Thus there are different *channels* in a meson system. The simple quark model (see, for example [37]) assumes conservation of the spin angular momentum quantum number of the meson $S = 0, 1$ and the orbital angular momentum quantum number $L = S, P, D, F$ corresponding to $0, 1, 2, 3$ respectively, and therefore states can be labelled with these numbers. The channels of the meson system are labelled $^{2S+1}L_J$, with $J = S \oplus L$ the total angular momentum quantum number. Each channel also exists in a specific radially excited state, labelled by the radial excitation quantum number $n = 1, 2, 3 \cdots$.

However, in a full relativistic theory, the only physically conserved quantum numbers are J, parity P and charge conjugation C. It is therefore often useful to label a state using J^{PC} notation. To switch between notations, the relations $P = (-1)^{L+1}$ and $C = (-1)^{L+S}$ can be used. For example, the vector $^3S_1$ has $J^{PC} = 1^{--}$.

2.2 The Υ System

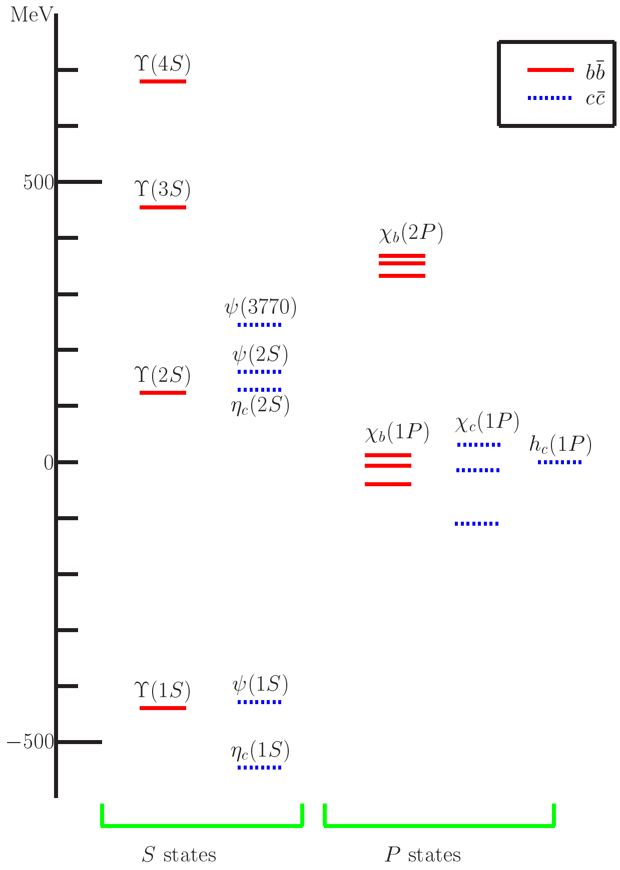

Figure 2.1: The heavyonium spectrum relative to the spin averaged χ_b and χ_c states.

The bottomonium system is the system of mesons which have as their valence particles a b and a $\bar{b}$. The system is commonly called the Upsilon (Υ) system, since the first bottomonium states discovered experimentally were the $n^3S_1 : n = 1 \cdots 3$ $\Upsilon(nS)$ states. They were found at Fermilab in 1977 by colliding protons and nuclei [38]. Since then, the preferred method for their production has been e^+e^- collisions (figure 2.2) which give better resolution. The χ_b states $1^3P_{0,1,2}$ and $2^3P_{1,2,3}$ have since been found in the radiative decays of the $\Upsilon(2S)$ (or Υ') and $\Upsilon(3S)$ (or Υ'') in 1983 [39] and 1982 [40, 41] respectively.

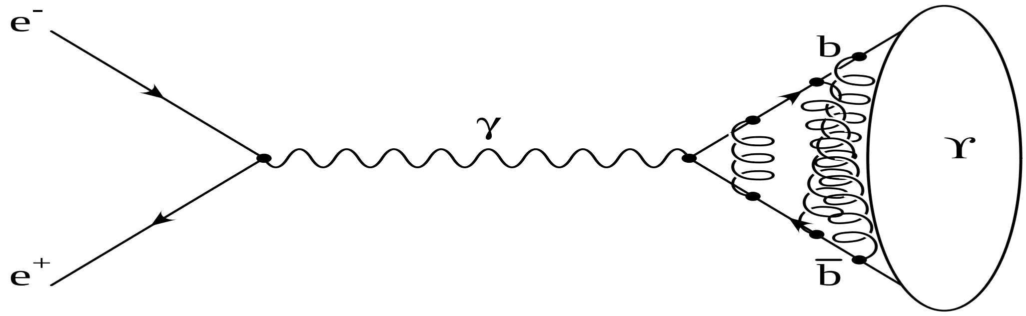

Figure 2.2: Creation of Υ in e^+e^- collision.

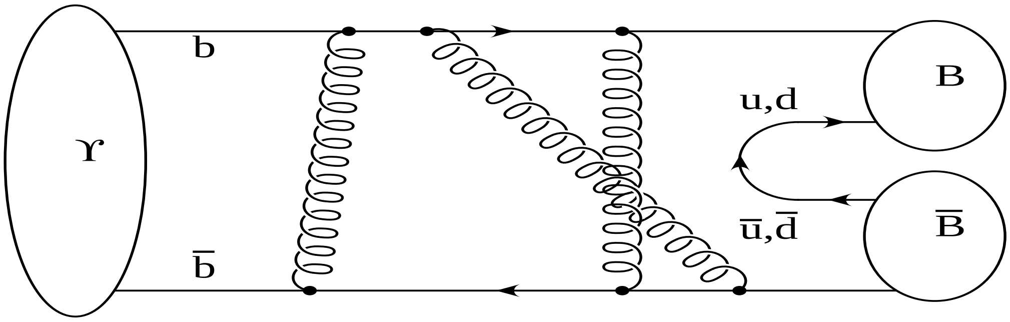

Figure 2.3: Decay of Υ to $B\bar{B}$.

There had been no further observations of narrow $b\bar{b}$ states until the summer of 2002 when CLEO-III found the $^3D_2$ state [42].

The Υ spectrum is shown in figure 2.1. The equivalent spectrum for the charmonium $c\bar{c}$ system is included for comparison. In both cases, the zero of energy has been set at the mass of the spin average of the $^3P_{0,1,2}$ χ channels, defined as

$$M_{\overline{\chi}} = \frac{M_{\chi_0} + 3M_{\chi_1} + 5M_{\chi_2}}{9}. \tag{2.1}$$

The $^1S_0$ η_b and the $^1P_1$ h_b bottomonium states have not yet been observed but are expected to exist because of the presence of the equivalent charmonium channels and because of quark model predictions. The experimental spectrum is very precisely known up to the threshold energy for decay to $B\bar{B}$ via the means of diagram 2.3. The states above this threshold have large widths and will not be considered in this thesis.

2.3 Heavy Meson Modelling

An exploitable property of charmonium and bottomonium spectra is that all the mass splittings are very much less than the masses of the mesons. This implies that the important dynamical scales such as the mesons' kinetic and potential energies are also much lower than their masses and therefore $v^2 << c^2$. It can be estimated [43] that the squared quark velocities are $v^2 \sim 0.1$ and 0.3 for the Υ and Ψ respectively. This fact can be exploited in developing methods to compute the physical properties of these heavy mesons.

Before introducing the method used in this thesis, the theory of NRQCD, I will review some alternative methods which are also used in heavy hadron spectroscopy.

Potential Modelling

The gluons exchanged by the quarks in the meson have an energy of the order of the quark momenta, and it is therefore a factor of $1/v$ larger than the quark kinetic energy. Therefore the interactions between heavy quarks in the meson are almost instantaneous (in the quarks' reference frame) and they can be modelled by Schrödinger's equation. Much work has been done in using lattice QCD to nonperturbatively compute the heavy quark potential which can be used in the Schrödinger equation (see e.g. [36, 44, 45]). This is done by replacing the heavy quarks by infinitely heavy static sources and using the lattice to determine the underlying Hamiltonian. Calculations have been done [45] with the inclusion of relativistic corrections to the static limit up to $\mathcal{O}(v^4)$. The resulting bottomonium spectrum from this is fairly close to but not in agreement with experiment. It would be extremely complicated to include higher order relativistic corrections in such a calculation, and this approach also ignores effects such as retardation.

Heavy Quark Effective Theory

Heavy quark effective theory (HQET) (see for example [46]) is an effective field theory of QCD in which a $1/m_q$ expansion is performed. Correlation functions are computed including only the lowest order term in the expansion, i.e. in the static limit and corrections are included systematically as perturbations to this static limit.

One major drawback with this method has been the problem of large statistical errors due to correlation functions in the static limit being very noisy. However, it has recently been claimed in [47] that this noise can be reduced by changing the lattice discretisation and in particular improving the links in a similar way to that described in section 1.3.6.

Other Lattice Methods at Non-infinite Quark Mass

To handle real b and c quarks, it is possible to use a discretisation of the Dirac equation provided that attention is paid to the fact that ma must be large.

The Fermilab formalism [48] uses the improved Wilson quark action with a non-relativistic interpretation to handle charm quarks. Recent calculations have been done on the same dynamical configurations as used in this thesis (see section 4.4).

Alternatively, a fine discretisation in the time direction of the lattice is sufficient to ensure that at least $ma_t < 1$ without needing a fine discretisation of the spatial directions. This anisotropic approach has has so far been applied in the quenched approximation [49, 50].

The effective theory of nonrelativistic QCD (NRQCD) is used in this thesis to accurately extract observables directly. The quark dynamics are retained in doing so. The following discussion of continuum and lattice NRQCD is a review of standard material.

2.4 Continuum NRQCD

Heavy meson spectroscopy is difficult to perform using full lattice QCD due to the wide range of energy scales involved. The three important scales are the mass of the meson M, its 3-momentum Mv and its kinetic energy Mv^2. Since v is small, these are very different. The lattice must be large compared to $1/Mv^2$ but must have a lattice spacing much smaller than $1/M$. This requires simulations using lattices of a size too large for current computers. NRQCD exploits the fact that all the bound-state physics happens at the scale of the quark momentum so an ultraviolet cutoff Λ can be imposed at a scale of the order of the quark mass $M >> Mv$. The relativistic states have strong effects as intermediate states but they are highly virtual and therefore local. Therefore they do not propagate long distances and can be compensated for by the addition of new local interactions in the Lagrangian.

At leading order in $1/\Lambda$ these relativistic contributions simply have the effect of shifting the bare quark mass and charge, and beyond leading order new non-renormalisable interactions are added such as (setting $\Lambda \sim M$) [51]

$$\frac{c_1 g}{M}\bar{\Psi}\sigma_{\mu\nu}F^{\mu\nu}\Psi + \frac{c_2 g}{M^2}\bar{\Psi}i\partial_\mu F^{\mu\nu}\gamma_\nu\Psi + \frac{c_3 g^2}{M^2}(\bar{\Psi}\gamma^\mu\Psi)^2 + \cdots . \tag{2.2}$$

One can work to a desired accuracy of $O(p/M)^n$ by keeping only up to and including the $O(1/M)^n$ terms. At the desired order, the couplings $M, g, c_1, c_2, c_3 \cdots$ are chosen such that the results agree with full QCD to this order.

The theory can be further simplified by applying a Foldy-Wouthuysen-Tani transformation [52] of the Dirac equation to a nonrelativistic expansion in powers of $1/M$:

$$\bar{\Psi}(\gamma.\mathbf{D} - M)\Psi \rightarrow \psi^\dagger(iD_t - M + \frac{\mathbf{D}^2}{2M})\psi + \psi^\dagger(\frac{g}{2M}\boldsymbol{\sigma}\cdot\mathbf{B} + \frac{g}{8M^2}\mathbf{D}.\mathbf{E} + \frac{\mathbf{D}^4}{8M^3} + \cdots)\psi, \tag{2.3}$$

where $\mathbf{B} = \mathrm{curl}\mathbf{A}$ and $\mathbf{E} = -\nabla\phi - \partial\mathbf{A}/\partial t$ are the chromomagnetic and chromoelectric field strengths respectively, with $(\phi, \mathbf{A})$ defined in Eqn. 1.14.

The upper and lower components of the four component field Ψ have decoupled into a field ψ representing the quark (as shown) and a field χ representing the antiquark which has analogous interactions.

Therefore with an ultraviolet cutoff of order M the NRQCD Lagrangian becomes

$$\begin{aligned}\mathcal{L}_{NRQCD} &= -\frac{1}{2}\mathrm{Tr}F_{\mu\nu}F^{\mu\nu} + \psi^\dagger(iD_t + \frac{\mathbf{D}^2}{2M})\psi + \psi^\dagger(c_1\frac{\mathbf{D}^4}{8M^3} + c_2\frac{g}{2M}\boldsymbol{\sigma}.\mathbf{B})\psi \\ &+ \psi^\dagger(c_3\frac{g}{8M^2}\mathbf{D}.\mathbf{E} + c_4\frac{ig}{8M^2}\boldsymbol{\sigma}.(\mathbf{D}\times\mathbf{E} - \mathbf{E}\times\mathbf{D}))\psi \\ &+ \text{antiquark terms} + \text{quark-antiquark terms} + \cdots . \end{aligned} \tag{2.4}$$

The $\psi^\dagger M\psi$ term has been dropped. This only has the effect of shifting the overall energy scale, not energy differences between states. The couplings can then be determined by matching NRQCD to full QCD, either perturbatively or non-perturbatively.

To work to a certain order in v^2, those terms which contribute at that level must be added. The method of *power counting* [51] can be used to estimate the magnitudes of such terms and determine whether they must be included when working to a certain order.

Operator	Description	Estimate of Magnitude
ψ	quark annihilation field	$(Mv)^{3/2}$
χ	antiquark creation field	$(Mv)^{3/2}$
D_t	covariant time derivative	Mv^2
$\mathbf{D}$	covariant spatial derivative	Mv
$g\phi$	scalar potential (in Coulomb Gauge)	Mv^2
$g\mathbf{A}$	vector potential (in Coulomb Gauge)	Mv^3
$g\mathbf{E}$	chromoelectric field	M^2v^3
$g\mathbf{B}$	chromomagnetic field	M^2v^4

Table 2.1: Estimation of magnitudes, in terms of the quark mass M and typical velocity v in a quarkonium state, of the component fields and operators for the NRQCD heavy quark action.

2.4.1 Power Counting

Rules have been developed to estimate the characteristic magnitudes of the fundamental operators and fields so that it can be determined which interaction terms must be included to the Lagrangian when working to a given precision. We require magnitudes for the quark and antiquark fields ψ and χ, the temporal part D_t and spatial part $\mathbf{D}$ of the covariant derivative, the scalar and vector potentials $g\phi$ and $g\mathbf{A}$, and the chromomagnetic and chromoelectric fields $g\mathbf{B}$ and $g\mathbf{E}$ where g is the coupling of the theory.

The heavy quark number operator

$$\int d^3x \psi^\dagger(x)\psi(x) \tag{2.5}$$

measures the number of quarks in the volume d^3x so has an expectation value close to 1 for Υ or ψ, where, from the uncertainty principle, the quark is localised within a region $\Delta x \sim 1/p$. Therefore,

$$\int d^3x \sim \frac{1}{p^3} \tag{2.6}$$

which gives

$$\psi^\dagger(x)\psi(x) \sim p^3, \tag{2.7}$$

and $\psi \sim p^{3/2}$.

The kinetic energy operator,

$$\int d^3x \psi^\dagger(x) \frac{\mathbf{D}^2}{2M} \psi(x), \tag{2.8}$$

measures the kinetic energy K of the meson giving

$$\mathbf{D} \sim \sqrt{2MK} \sim p. \tag{2.9}$$

The leading order (lowest order in v^2) terms in the Lagrangian are (from the Schrödinger equation)

$$L_0 = \psi^\dagger(x) \left(iD_t + \frac{\mathbf{D}^2}{2M} \right) \psi. \tag{2.10}$$

Substituting this into the Euler-Lagrange Equation Eqn. 1.6 leads to

$$(iD_t + \frac{\mathbf{D}^2}{2m})\psi = 0, \tag{2.11}$$

so the magnitude of the temporal covariant derivative can be estimated as

$$D_t \sim \frac{\mathbf{D}^2}{2M} \sim K. \tag{2.12}$$

The Coulomb gauge Eqn. 1.21 is the most natural for nonrelativistic systems as in this gauge the spatial gluon field is minimised and $\mathbf{D}^2$ is most like the $\mathbf{p}^2$ from the Schrödinger equation. In this gauge, the field equation becomes

$$(i\partial_t - g\phi(x) + \frac{\nabla^2}{2m})\psi \sim 0, \tag{2.13}$$

where the vector potential has been neglected because it is small in this gauge. The $g\phi$ term is the origin of the potential energy in the system which is in a bound state so it must balance the kinetic energy. Hence,

$$g\phi(x) \sim K. \tag{2.14}$$

The 4-vector field $A_\mu = (\phi, \mathbf{A})$ also satisfies the Euler-Lagrange equation Eqn. 1.6. Thus, again neglecting the vector potential,

$$\nabla^2 g\phi(x) = -g^2 \psi^\dagger(x)\psi(x). \tag{2.15}$$

From this we get

$$g\phi(x) \sim \frac{1}{p^2} g^2 p^3 \sim g^2 p. \tag{2.16}$$

This agrees with the above if the strong coupling constant at low energies has a magnitude

$$\alpha_s \sim g^2 \sim v. \tag{2.17}$$

Now including the vector potential in the solution to the field equations we get

$$(\partial_t^2 - \nabla^2) g\mathbf{A} = \frac{g^2}{M} \psi^\dagger \nabla \psi + g\phi \nabla g\phi + \cdots , \tag{2.18}$$

which implies that

$$g\mathbf{A}(x) \sim \frac{1}{p^2} (\frac{g^2}{M} p^4 + pK^2) \sim vK. \tag{2.19}$$

The chromomagnetic and chromoelectric fields' magnitudes then can be estimated as

$$g\mathbf{E} \sim -\nabla g\phi + \cdots \sim pK \tag{2.20}$$

$$g\mathbf{B} \sim \nabla \times g\mathbf{A} + \cdots \sim K^2 \tag{2.21}$$

This is summed up in table 2.1.

2.4.2 NRQCD Interactions

The power counting rules from the previous section can now be used to determine which of the most general possible interactions which posess the symmetries of the original theory must be included in the NRQCD action when working to a given order. The antiquark action can be obtained directly from the quark action simply by taking the complex conjugate and thus can be neglected in the following development.

The primary terms which need to be considered are those lowest order in v^2, which have already been stated in Eqn. 2.10.

The next set of terms which need to be considered are those which are bilinear in the quark field suppressed by v^2 with respect to the leading order terms;

$$\begin{aligned}
\delta\mathcal{L}_{bilinear} &= c_1 \frac{1}{M^3} \psi^\dagger \mathbf{D}^4 \psi \\
&+ c_2 \frac{g}{M^2} \psi^\dagger (\mathbf{D}.\mathbf{E} - \mathbf{E}.\mathbf{D}) \psi \\
&+ c_3 \frac{ig}{M^2} \psi^\dagger \boldsymbol{\sigma}.(\mathbf{D} \times \mathbf{E} - \mathbf{E} \times \mathbf{D}) \psi \\
&+ c_4 \frac{g}{M} \psi^\dagger \boldsymbol{\sigma} \cdot \mathbf{B} \psi. \qquad (2.22)
\end{aligned}$$

These terms give rise to the spin-splittings in the spectrum. The inclusion of these terms means relativistic errors will be at $\mathcal{O}(Mv^6) \sim 5$MeV, i.e. for the Υ where $v^2 \sim 0.1$, about 1% of a typical radial or orbital excitation or 10% of a typical spin splitting. Terms involving the time derivative, D_t, of the quark field have not been included above as they evoke an extremely complicated evolution equation for the quark propagators. Instead, we can redefine the quark fields such that, in accordance with the field equation Eqn. 2.11 for ψ

$$iD_t\psi(x) \sim \frac{-\mathbf{D}^2}{2M}\psi(x), \qquad (2.23)$$

effectively factors of iD_t are replaced by factors of $\mathbf{D}^2/2M$.

To achieve accuracies of 1% for spin splittings, terms which are suppressed by v^4 relative to the leading order terms must be included:

$$\begin{aligned}
\delta\mathcal{L}_{spin} &= f_1 \frac{g}{M^3} \psi^\dagger \{\mathbf{D}^2, \boldsymbol{\sigma} \cdot \mathbf{B}\} \psi \\
&+ f_2 \frac{ig}{M^4} \psi^\dagger \{\mathbf{D}^2, \boldsymbol{\sigma}.(\mathbf{D} \times \mathbf{E} - \mathbf{E} \times \mathbf{D})\} \psi \\
&+ f_3 \frac{ig^2}{M^3} \psi^\dagger \boldsymbol{\sigma}.\mathbf{E} \times \mathbf{E} \psi. \qquad (2.24)
\end{aligned}$$

Using the power counting rules of section 2.4.1, it is estimated that these spin-dependent corrections should result in splittings which are smaller than radial and orbital splittings by a factor of v^2, i.e. 0.1 for bottomonium and 0.3 for charm. From figure 2.1 it can be seen that this is indeed consistent and this is good verification that the power counting rules are working and reliable.

At first thought, the four fermion terms arising from the quark-antiquark pieces of Eqn.

2.4

$$\begin{aligned} \delta\mathcal{L}_{contact} &= d_1 \frac{1}{M^2}\psi^\dagger\chi\chi^\dagger\psi \\ &+ d_2 \frac{1}{M^2}\psi^\dagger\boldsymbol{\sigma}\chi.\chi^\dagger\boldsymbol{\sigma}\psi \end{aligned} \tag{2.25}$$

seem to be down on the leading order terms by only a factor of v and should be included when working to this order. However, these terms must be further suppressed by a factor of α_s^2 since they do not occur in relativistic QCD and must come in as 1-loop corrections. They are therefore ignored and we will only work to leading order in α_s. Similarly, the four-fermion operators coupled to coloured states

$$\begin{aligned} \delta\mathcal{L}_{colour} &= d_3 \frac{1}{M^2}\sum_a \psi^\dagger T^a\chi\chi^\dagger T^a\psi \\ &+ d_4 \frac{1}{M^2}\sum_a \psi^\dagger T^a\boldsymbol{\sigma}\chi.\chi^\dagger T^a\boldsymbol{\sigma}\psi \end{aligned} \tag{2.26}$$

are also not included because such coupling is equivalant to virtual gluon emission which is suppressed by a factor of v^2.

2.4.3 Determination of coefficients

In the previous section it was determined which operators must be included due to relativistic corrections when working to a certain order. Now we must determine values for the coupling constants which multiply these operators. This can be done for each term by way of requiring that a perturbative result in NRQCD agrees with that of the equivalent QCD result, to a certain order in α_s. Here we work to tree level (zeroth order in α_s).

Kinetic Term

A quark has relativistic energy

$$\sqrt{\mathbf{p}^2 + M^2} \sim M + \frac{\mathbf{p}^2}{2M} - \frac{\mathbf{p}^4}{8M^3}. \tag{2.27}$$

Therefore, the kinetic correction to the Schrödinger term must be

$$\delta\mathcal{L}_K = \frac{1}{8M^3}\psi^\dagger\mathbf{D}^4\psi \tag{2.28}$$

which sets $c_1 = 1/8$ in equation 2.22.

Electric Couplings

For the case of the corrections which are linear in $g\mathbf{E}$, the coefficients are determined by matching the order g amplitude T_E for scattering a quark off a static electric field.

In QCD,

$$T_E(\mathbf{p},\mathbf{q}) = \overline{u}(\mathbf{q})\gamma^0 g\phi(\mathbf{q}-\mathbf{p})u(\mathbf{p}). \tag{2.29}$$

We are going to match this with NRQCD so v must be small and we can expand in powers of $\mathbf{q}/M$ and $\mathbf{p}/M$.

The Dirac spinor is

$$u(\mathbf{p}) = \sqrt{(\frac{E_p+M}{2E_p})}\left[\begin{array}{c} \psi \\ \frac{\boldsymbol{\sigma}.\boldsymbol{p}}{E_p+M}\psi \end{array}\right], \tag{2.30}$$

where $E_p \equiv \sqrt{\mathbf{p}^2+M^2}$ and ψ is a 2 component spinor. Therefore, from equation 2.29 we get

$$\begin{aligned} T_E(\mathbf{p},\mathbf{q}) &= \sqrt{\frac{(E_p+M)(E_q+M)}{4E_pE_q}} \\ &\times \psi^\dagger\left[1+\frac{\mathbf{p}.\mathbf{q}+i\boldsymbol{\sigma}.\mathbf{q}\times\mathbf{p}}{(E_q+M)(E_p+m)}\right]g\phi(\mathbf{q}-\mathbf{p})\psi \\ &\equiv S_E(\mathbf{p},\mathbf{q})+V_E(\mathbf{p},\mathbf{q}) \end{aligned} \tag{2.31}$$

where, expanded to second order in $\mathbf{p}/M$ and $\mathbf{q}/M$, the scalar spin independent term S_E is given by

$$S_E(\mathbf{p},\mathbf{q}) = \left(1-\frac{(\mathbf{p}-\mathbf{q})^2}{8M^2}\right)\psi^\dagger g\phi(\mathbf{q}-\mathbf{p})\psi \tag{2.32}$$

and similarly the spin dependent V_E is

$$V_E(\mathbf{p},\mathbf{q}) = \left(\frac{i}{4M^2}-\frac{3i}{32M^4}(\mathbf{p^2}+\mathbf{q^2})\right)\psi^\dagger\boldsymbol{\sigma}.\mathbf{q}\times\mathbf{p}g\phi(\mathbf{q}-\mathbf{p})\psi \tag{2.33}$$

Now the coefficients of the NRQCD action must be set such that computation of this same process results in the same terms.

The iD_t term from equation 2.10 results in a scattering amplitude $\psi^\dagger g\phi(\mathbf{q}-\mathbf{p})\psi$ which exactly accounts for the first term in S_E. The remaining terms in S_E and V_E can similarly be accounted for if the following terms are included in the NRQCD action:

$$\begin{aligned}\delta\mathcal{L}_E &= \frac{g}{8M^2}\psi^\dagger(\mathbf{D}.\mathbf{E}-\mathbf{E}.\mathbf{D})\psi \\ &+ \frac{ig}{8M^2}\psi^\dagger\boldsymbol{\sigma}.(\mathbf{D}\times\mathbf{E}-\mathbf{E}\times\mathbf{D})\psi \\ &+ \frac{3ig}{64M^4}\psi^\dagger\{\mathbf{D^2},\boldsymbol{\sigma}.(\mathbf{D}\times\mathbf{E}-\mathbf{E}\times\mathbf{D})\}\psi. \end{aligned} \tag{2.34}$$

This therefore sets $c_1 = c_2 = 1/8$ in Eqn. 2.22 and $f_2 = 3/64$ in Eqn. 2.24.

Magnetic Couplings

The magnetic couplings can similarly be calculated this time in determining the scattering amplitude T_B of a quark from a static vector potential $\mathbf{A}$;

$$T_B(\mathbf{p},\mathbf{q}) = -\overline{u}(\mathbf{q})\gamma.g\mathbf{A}(\mathbf{q}-\mathbf{p})u(\mathbf{p}), \tag{2.35}$$

which, when expanded in $\mathbf{p}/M$ gives

$$\begin{aligned} T_B(\mathbf{p},\mathbf{q}) &= -\frac{g}{2M}\left(1-\frac{\mathbf{p^2}}{2M^2}\right) \\ &\times \psi^\dagger[(\mathbf{p}+\mathbf{q}).\mathbf{A}+\boldsymbol{\sigma}.\mathbf{A}\times(\mathbf{p}-\mathbf{q})]\psi \\ &\equiv S_B(\mathbf{p},\mathbf{q})+V_B(\mathbf{p},\mathbf{q}). \end{aligned} \tag{2.36}$$

The terms in S_B are accounted for by the NRQCD kinetic $\mathbf{D^2}$ and $\mathbf{D^4}$ terms but the only way to account for the terms in V_B is to include in the action the terms

$$\begin{aligned} \mathcal{L}_B &= \frac{g}{2M}\psi^\dagger\boldsymbol{\sigma}\cdot\mathbf{B}\psi \\ &+ \frac{g}{8M^3}\psi^\dagger\{\mathbf{D^2},\boldsymbol{\sigma}\cdot\mathbf{B}\}\psi. \end{aligned} \tag{2.37}$$

This fixes $c_4 = 1/2$ in 2.22 and $f_1 = 1/8$ in 2.24.

Continuum Euclidean NRQCD action to order v^4

Since our aim is to construct a Lagrangian which may be discretised for lattice simulations, as described in the previous chapter we use the relations Eqn. 1.25 - Eqn. 1.30 to perform a Wick rotation and we will work in Euclidean space for the rest of this thesis. From Eqns. 2.10 and 2.22 the continuum NRQCD Lagrangian, correct through $\mathcal{O}(Mv^4)$, can be written

$$\mathcal{L}_{cont} = \psi^\dagger(D_t + H_0^{cont})\psi + \psi^\dagger \delta H^{cont}\psi \tag{2.38}$$

where

$$H_0^{cont} = -\frac{\mathbf{D^2}}{2M} \tag{2.39}$$

and

$$\begin{aligned} \delta H^{cont} &= \frac{1}{8M^3}\mathbf{D}^4 + \frac{ig}{8M^2}(\mathbf{D}.\mathbf{E} - \mathbf{E}.\mathbf{D}) \\ &- \frac{g}{8M^2}\boldsymbol{\sigma}\cdot(\mathbf{D}\times\mathbf{E} - \mathbf{E}\times\mathbf{D}) - \frac{g}{2M}\boldsymbol{\sigma}\cdot\mathbf{B}. \end{aligned} \tag{2.40}$$

The relativistic errors involved with the emission of higher order relativistic terms will therefore be of $\mathcal{O}(Mv^6) \sim 5$Mev. We will only work to this order in this thesis but future work will need to go beyond this order. To work to $\mathcal{O}(v^6)$ lattice discretisations of the terms in 2.24 must be included.

2.5 Lattice NRQCD

In section 1.3, a lattice formulation was used to regularise full QCD. Now we regularise the nonrelativistic counterpart NRQCD on the lattice in a similar vein. A discretised version of the NRQCD Lagrangian Eqn. 2.40 will be developed from a few basic elements. The following backward and forward derivatives are used to replace covariant derivatives:

$$\Delta_\mu^{(+)}\psi(x) \equiv \frac{1}{a}(U_\mu(x)\psi(x+a\hat{\mu}) - \psi(x)) \tag{2.41}$$

$$\Delta_\mu^{(-)}\psi(x) \equiv \frac{1}{a}(\psi(x) - U_\mu^\dagger(x-a\hat{\mu})\psi(x-a\hat{\mu})) \tag{2.42}$$

$$\Delta^{(\pm)} \equiv \frac{1}{2}(\Delta^{(+)} + \Delta^{(-)}). \tag{2.43}$$

The lattice Laplacian becomes

$$\boldsymbol{\Delta}^{(2)} \equiv \sum_i \Delta_i^{(+)}\Delta_i^{(-)} = \sum_i \Delta_i^{(-)}\Delta_i^{(+)}. \tag{2.44}$$

As described in section 1.3.5, cloverleaf operators $F^{cvr}_{\mu\nu}(x)$ are used for the field $F_{\mu\nu}(x)$. The lattice covariant derivatives of $F^{cvr}_{\mu\nu}(x)$ are given by

$$\Delta^{(+)}_{\rho} F^{cvr}_{\mu\nu}(x) \equiv \frac{1}{a}(U_{\rho}(x)F^{cvr}_{\mu\nu}(x+a\hat{\rho}) - F^{cvr}_{\mu\nu}(x)) \tag{2.45}$$

$$\Delta^{(-)}_{\rho} F^{cvr}_{\mu\nu}(x) \equiv \frac{1}{a}(F^{cvr}_{\mu\nu}(x) - U^{\dagger}_{\rho}(x-a\hat{\rho})F^{cvr}_{\mu\nu}(x-a\hat{\rho})) \tag{2.46}$$

The chromomagnetic field $\mathbf{B}$ and chromoelectric field $\mathbf{E}$ are defined in terms of the cloverleaf field 1.75 as

$$E^i(x) = F^{(cvr)}_{0i}(x) \tag{2.47}$$

$$B^i(x) = \frac{1}{2}\epsilon_{ijk}F^{(cvr)}_{jk}(x). \tag{2.48}$$

These elements can now be solely used to construct the lattice NRQCD Lagrangian and hence the heavy quark propagators.

2.5.1 Leading Order Quark Evolution Equation

Initially ignoring the δH terms, a lattice NRQCD action $S^{(n)}_0$ can be defined as [51]

$$\begin{aligned} S^{(n)}_0 &= a^3 \sum_x \psi^{\dagger}(x)\psi(x) \\ &- a^3 \sum_x \psi^{\dagger}(x+a\hat{t})\left(1-\frac{aH_0}{2n}\right)^n U^{\dagger}_{\mu}(\mathbf{x},t)\left(1-\frac{aH_0}{2n}\right)^n \psi(x), \end{aligned} \tag{2.49}$$

where the 'stability parameter' n is a positive integer which, depending on the bare quark mass, may take a value other than 1 in order to stabilise the quark propagator as will be explained shortly. H_0 is the lattice kinetic energy operator

$$H_0 \equiv -\frac{\boldsymbol{\Delta}^{(2)}}{2M} \tag{2.50}$$

The quark propagator G must satisfy the condition

$$\sum_y K(x,y)G(y,0) = \delta_{\mathbf{x},\mathbf{0}}\delta_{t,0} \tag{2.51}$$

where $K(x,y)$ is the bilinear term appearing in the action. Therefore, here the quark propagator satisfies the evolution equation [51]

$$G(\mathbf{x},t+a) = \left(1-\frac{aH_0}{2n}\right)^n U^{\dagger}_{\mu}(\mathbf{x},t)\left(1-\frac{aH_0}{2n}\right)^n G(\mathbf{x},t) \tag{2.52}$$

with the initial condition

$$G(\mathbf{x}, 0) = \delta_{\mathbf{x},0}. \tag{2.53}$$

As is discussed in [53], if $n = 1$ and $Ma > 3$ modes with high momenta will give a contribution to the quark propagator which will increase with t. This creates a large background from which it becomes difficult to separate the small contributions of the physical low-momentum modes. This instability is resolved by setting $n > 1$ and in general n must be set such that that $Ma > 3/n$ is satisfied.

2.5.2 Discretisation Error Corrections

The introduction of a finite lattice spacing results in systematic errors which appear first at $\mathcal{O}(a^2)$. The $\mathcal{O}(a^2)$ errors can be quantified and removed.

Spatial Derivatives

Looking at the action of the operators Eqns. 2.41 and 2.42 on the continuum gauge fields from the expansion of Eqn. 1.41, and on the Taylor expansions of the quark fields leads to the relations

$$\Delta_i^{(+)} \equiv exp(aD_i) - 1 = aD_i + \frac{a^2}{2}D_i^2 + \cdots \tag{2.54}$$

$$\Delta_i^{(-)} \equiv 1 - exp(-aD_i) = aD_i - \frac{a^2}{2}D_i^2 + \cdots . \tag{2.55}$$

These $\mathcal{O}(a^2)$ errors can therefore be removed by using the improved operators

$$\tilde{\Delta}_i^{(+)} \equiv \Delta_i^{(+)} - \frac{a}{2}(\Delta_i^{(+)})^2 \tag{2.56}$$

$$\tilde{\Delta}_i^{(-)} \equiv \Delta_i^{(+)} + \frac{a}{2}(\Delta_i^{(-)})^2 \tag{2.57}$$

$$\tilde{\Delta}_i^{(\pm)} \equiv \Delta_i^{(\pm)} - \frac{a^2}{6}\Delta_i^{(+)}\Delta_i^{(\pm)}\Delta_i^{(-)} \tag{2.58}$$

giving

$$\tilde{\boldsymbol{\Delta}}^{(2)} = \boldsymbol{\Delta}^{(\mathbf{2})} - \frac{a^2}{12}[\Delta_i^{(+)}\Delta_i^{(-)}]^2 \tag{2.59}$$

which are accurate to $\mathcal{O}(a^4)$.

Temporal Derivatives

The method of the previous section cannot be used to improve the temporal derivatives. Unlike the relativistic Dirac theory, quark propagation in NRQCD is governed by a Schrödinger like equation in which the temporal derivative is different from the spatial derivative. It is this very property which makes working with NRQCD so appealing as the calculation of the quark Green's functions can be done using a simplistic evolution equation instead of having to solve a boundary value Dirac problem. Naive improvement of the temporal derivatives would introduce higher order time derivatives destroying this simplicity.

Instead, however, the quark Green function, Eqn. 2.52 can be improved. If the gauge field is neglected for the time being, this equation may be written in the form

$$\begin{aligned} G(\mathbf{x}, t+a) &= \left(1 - \frac{aH_0}{2n}\right)^{2n} G(\mathbf{x}, t) \\ &= e^{-aH_{eff}} G(\mathbf{x}, t), \end{aligned} \tag{2.60}$$

with H_{eff} being an effective Hamiltonian defined as

$$\begin{aligned} H_{eff} &\equiv -\frac{2n}{a} ln \left(1 - \frac{aH_0}{2n}\right) \\ &= H_0 + \frac{a}{4n} H_0^2 + \cdots . \end{aligned} \tag{2.61}$$

This $\mathcal{O}(a)$ error can therefore be removed by replacing H_0 with the improved

$$\tilde{H}_0 = H_0 - \frac{a}{4n} H_0^2. \tag{2.62}$$

Using $\tilde{H}_0$ in the full equation 2.52 is equivalent to improving the temporal derivatives naively.

Chromoelectric and Chromomagnetic Fields

The cloverleaf field $F_{\mu\nu}^{cvr}$ differs from the continuum field strength tensor $F_{\mu\nu}^{cvr}$ at $\mathcal{O}(a^2)$. It is shown in [51] that if the replacement

$$\begin{aligned} F_{\mu\nu}^{cvr}(x) \to \tilde{F}_{\mu\nu}^{cvr}(x) &= \frac{5}{3} g F_{\mu\nu}^{cvr}(x) - \frac{1}{6}[U_\mu(x) g F_{\mu\nu}^{cvr}(x + a\hat{\mu}) U_\mu^\dagger(x) \\ &+ U_\mu^\dagger(x - a\hat{\mu}) g F_{\mu\nu}^{cvr}(x - a\hat{\mu}) U_\mu(x - a\hat{\mu},) - (\mu \Leftrightarrow \nu)] \end{aligned} \tag{2.63}$$

is undertaken, then these $\mathcal{O}(a^2)$ errors are removed and $\tilde{F}_{\mu\nu}^{cvr}(x)$ is correct to $\mathcal{O}(a^4)$.

2.6 Quark Evolution Equation to $\mathcal{O}(Mv^4)$

A quark evolution equation correct through $\mathcal{O}(Mv^4)$ can be obtained by including lattice discretisations of the δH terms in Eq. 2.38. As is discussed in [54], at this order the spatial and temporal lattice spacing corrections should be included as should the corrected clover terms which contribute to the hyperfine spliting (i.e. those in a term involving σ). The $\mathcal{O}(Mv^4)$ quark evolution equation is then

$$G(\mathbf{x}, t+a) = \left(1 - \frac{aH_0}{2n}\right)^n \left(1 - \frac{a\delta H}{2}\right) U_\mu^\dagger(\mathbf{x}, t) \left(1 - \frac{a\delta H}{2}\right) \left(1 - \frac{aH_0}{2n}\right)^n G(\mathbf{x}, t), \quad (2.64)$$

with the initial condition

$$G(\mathbf{x}, 0) = \delta_{\mathbf{x},0} \quad (2.65)$$

where

$$\begin{aligned} H_0 &= -\frac{\Delta^{(2)}}{2M}, \\ \delta H &= -\frac{(\boldsymbol{\Delta}^{(2)})^2}{8M^3} + \frac{ig}{8M^2}(\boldsymbol{\Delta}^{(\pm)} \cdot \mathbf{E} - \mathbf{E} \cdot \boldsymbol{\Delta}^{(\pm)}) \\ &- \frac{g}{8M^2}\sigma \cdot (\boldsymbol{\Delta}^{(\pm)} \times \tilde{\mathbf{E}} - \tilde{\mathbf{E}} \times \boldsymbol{\Delta}^{(\pm)}) \\ &- \frac{g}{2M}\sigma \cdot \tilde{\mathbf{B}} + \frac{a^2\Delta^{(4)}}{24M} - \frac{a(\Delta^{(2)})^2}{16nM^2}. \end{aligned} \quad (2.66)$$

This evolution equation, when tadpole improved (see next section) will be the one used for the work in this thesis.

2.7 Radiative Corrections and Tadpole Improvement

Tadpole improvement (introduced in section 1.3.2) is applied to the theory. The U_μ fields transform as in Eqn. 1.52, with the consequence of the chromoelectric and chromomagnetic fields transforming as

$$\mathbf{E} \to \frac{\mathbf{E}}{u_0^4}, \quad (2.67)$$

$$\mathbf{B} \to \frac{\mathbf{B}}{u_0^4}. \quad (2.68)$$

Care must be taken, however, in tadpole improving the improved cloverleaf operator $\tilde{F}^{cvr}_{\mu\nu}(x)$ from Eqn. 2.63. The latter terms in this equation incorporate two extra gauge field terms. Naively, this suggests that this will result in terms which have six gauge fields (since each part of the cloverleaf term has four links), and one should divide by u_0^6. This is exactly what our code does.

However, in actual fact, the unitarity of U_μ causes cancellations in U with $U^\dagger$ fields resulting in terms which are over tadpole improved by a factor of $1/u_0^2$. This must be corrected and can be done so with the addition to Eqn. 2.63 of the term [54]

$$+\frac{1}{3}\left(\frac{1}{u_0^2}-1\right)F^{cvr}_{\mu\nu}(x). \tag{2.69}$$

2.8 Lattice Simulation of the Υ Meson

The propagators for the NRQCD quark and antiquark (which, as explained in section 2.4 has analogous interactions) which were derived in section 2.6 can be combined to give a meson propagator.

Since $\psi^\dagger$ creates a quark and $\chi^\dagger$ creates an antiquark, the interpolating operator

$$\mathcal{O}^\dagger(t) = \sum_{\mathbf{x_1},\mathbf{x_2}} \psi^\dagger(\mathbf{x_1},t)\Gamma(\mathbf{x_1}-\mathbf{x_2})\chi^\dagger(\mathbf{x_2},t) \tag{2.70}$$

creates a meson, where the *meson operator* Γ is constructed as

$$\Gamma(\mathbf{x_1}-\mathbf{x_2}) = \Omega\phi(|\mathbf{x_1}-\mathbf{x_2}|). \tag{2.71}$$

Ω selects a meson with the desired ${}^{2S+1}L_J$ quantum numbers (see table 2.2) and ϕ is a smearing function, as will be described in the next section.

The meson propagator from time 0 to time t is then given by the 2-point function

$$\langle 0|\mathcal{O}(t)\mathcal{O}^\dagger(0)|0\rangle. \tag{2.72}$$

The quark and antiquark propagators are respectively given by

$$\begin{aligned} Q_{i,j;\alpha,\beta}(\mathbf{y},t;\mathbf{x}) &= \langle 0|\psi_{i,\alpha}(\mathbf{y},t)\psi^\dagger_{j,\beta}(\mathbf{x},0)|0\rangle && (2.73)\\ Q^A_{i,j;\alpha,\beta}(\mathbf{y},t;\mathbf{x}) &= \langle 0|\chi_{i,\alpha}(\mathbf{y},t)\chi^\dagger_{j,\beta}(\mathbf{x},0)|0\rangle && (2.74)\end{aligned}$$

so using the fact that $Q^A = Q^*$ and eliminating the summation over initial antiquark position using translational invariance, the meson propagator Eqn. 2.72 is then

$$G_{meson}(t) = \sum_{\mathbf{y_1},\mathbf{y_2}} \mathrm{Tr}\left[G_t^\dagger(\mathbf{y_2}) {\Gamma^{(sk)}}^\dagger(\mathbf{y_1}-\mathbf{y_2})\tilde{G}_t(\mathbf{y_1})\right] \tag{2.75}$$

where

$$\tilde{G}_t(\mathbf{y}) \equiv \sum_x G_t(\mathbf{y}-\mathbf{x})\Gamma^{(sc)}(\mathbf{x}) \tag{2.76}$$

with the trace over spin and colour, and where $G_t(\mathbf{x}) = G(\mathbf{x}, t)$. $\Gamma^{(sc)}$ is the smearing at the source (when the meson is created) whilst $\Gamma^{(sk)}$ is the smearing at the sink (when the meson is destroyed). In Eqn. 2.64 if we replace $\delta_{\mathbf{x},0}$ with $\Gamma^{(sc)}(\mathbf{x})$,this yields $\tilde{G}_t(\mathbf{x})$ directly, and $\tilde{G}$ is therefore referred to as the quark propagator.

2.8.1 Meson Operators and Smearing

The purpose of the meson operator Eqn. 2.71 is to construct a meson with the desired quantum numbers [55, 56]. The Ω operator is chosen to have the same $^{2S+1}L_J$ quantum numbers as the desired meson. Since this does not differentiate between mesons with differing radial quantum number n, its use will create a mixture of different n states. The purpose of the *smearing* operator ϕ is to maximise the contribution of a specific radially excited state in the meson propagation.

To do this ϕ is chosen to have a large overlap with the appropriate radial excitation. The ideal form for ϕ is the wavefunction of the n_{th} state but the exact form of this is not known for bottomonium and much work has been done in order to determine what functions can be used to best represent such bottomonium wavefunctions. It is important that the major properties of the states are represented by the smearing such as the fact that physical S wave states are symmetric and have non-zero wavefunction at the origin and P wave states have vanishing wavefunction at the origin. In this thesis we follow the procedure of [54] and use the radial part $R_{n,L}(r)$ of the hydrogenic style wavefunctions (see for example [57])

$$\psi_{n,L,S} = R_{n,L}(r)Y_{L,S}(\theta, \phi), \tag{2.77}$$

where $Y_{L,S}(\theta, \phi)$ is a spherical harmonic part and (r, θ, ϕ) are spherical coordinates.

Our smearing functions then become for the S wave states

$$\phi_g^{(S)}(r, r_0^S) = exp(-\frac{r}{r_0^S}) \tag{2.78}$$

$$\phi_e^{(S)}(r, r_0^S) = (2r_0^S - r)exp(-\frac{r}{2r_0^S}) \tag{2.79}$$

$$\phi_d^{(S)}(r, r_0^S) = (27(r_0^S)^2 - 18r_0^S r + 2r^2)exp(-\frac{r}{3r_0^S}) \tag{2.80}$$

where $g, e,$ and d represent $n = 1, 2, 3$ respectively and r_0 is the Bohr radius. The P and D wave smearings are constructed from the S wave smearings:

$$(\phi_{g,e}^{(P)}(r, r_0^P))_x = |x|\phi_{g,e}^{(S)}(r, r_0^P) \tag{2.81}$$

$$(\phi_{g,e}^{(P)}(r, r_0^P))_y = |y|\phi_{g,e}^{(S)}(r, r_0^P) \tag{2.82}$$

$$(\phi_{g,e}^{(P)}(r, r_0^P))_z = |z|\phi_{g,e}^{(S)}(r, r_0^P) \tag{2.83}$$

$$(\phi_{g,e}^{(D)}(r, r_0^D))_x = |y||z|\phi_{g,e}^{(S)}(r, r_0^D) \tag{2.84}$$

$$(\phi_{g,e}^{(D)}(r, r_0^D))_y = |x||z|\phi_{g,e}^{(S)}(r, r_0^D) \tag{2.85}$$

$$(\phi_{g,e}^{(D)}(r, r_0^D))_z = |x||y|\phi_{g,e}^{(S)}(r, r_0^D) \tag{2.86}$$

where $()_{x,y,z}$ denotes the wavefunction in that specific spatial dimension.

In this thesis, the values

$$r_0^S = 1.0 \tag{2.87}$$

$$r_0^P = 0.5 \tag{2.88}$$

were chosen following work in [54] and

$$r_0^D = 0.5 \tag{2.89}$$

was chosen succesfully as a guess.

Coulomb Gauge Fixing

If we were to calculate the quark propagators without first fixing the gauge then the use of the smearing functions would cause the meson operator to be non gauge-invariant and it will

Meson $^{2S+1}L_J(J^{PC})$	Lattice Rep.	$\Gamma = \Omega\phi$ Ω	ϕ
$^1S_0(0^{-+})$	A_1^{-+}	$\hat{I}$	$\phi^{(S)}_{n_{sc}}(r);\ n_{sc} = loc, g, e, d$
$^3S_1(1^{--})$	$T^{--}_{1(i)}$	σ_i	
$^1P_1(1^{+-})$	$T^{+-}_{1(i)}$	Δ_i	$\phi^{(P)}_{n_{sc}}(r);\ n_{sc} = loc, g, e$
$^3P_0(0^{++})$	A_1^{++}	$\sum_j \Delta_j\sigma_j$	
$^3P_1(1^{++})$	$T^{++}_{1(k)}$	$\Delta_i\sigma_j - \Delta_j\sigma_i$	
$^3P_2(2^{++})$	$E^{++}_{(k)}$	$\Delta_i\sigma_i - \Delta_j\sigma_j$	
	$T^{++}_{2(ij)}$	$\Delta_i\sigma_j + \Delta_j\sigma_i\ (i \neq j)$	
$^1D_2(2^{-+})$	$E^{-+}_{(k)}$	$D_{ii} - D_{jj}$	$\phi^{(D)}_{n_{sc}}(r);\ n_{sc} = loc, g, e$
	$T^{-+}_{2(ij)}$	$D_{ij}\ (i \neq j)$	
$^3D_1(1^{--})$	$T^{--}_{1(i)}$	$\sum_j D_{ij}\sigma_j$	
$^3D_2(2^{--})$	$E^{--}_{(j)}$	$D_{ij}\sigma_k - D_{jk}\sigma_i$	
	$T^{--}_{2(ij)}$	$(D_{ii} - D_{jj})\sigma_k + D_{jk}\sigma_j - D_{ki}\sigma_i$	
$^3D_3(3^{--})$	A_2^{--}	$(D_{ij}\sigma_k + D_{jk}\sigma_i + D_{ki}\sigma_j)/3$	
	$T^{--}_{1(i)}$	$D_{ii}\sigma_i - 2/5\sum_j D_{ij}\sigma_j$	
	$T^{--}_{2(ij)}$	$(D_{ii} - D_{jj})\sigma_k + 2(D_{ki}\sigma_i - D_{kj}\sigma_j)$	

Table 2.2: Meson operators and smearing functions used in the construction of the lattice representations of mesons.

vanish in the ensemble average [36]. We here chose to fix to the Coulomb gauge 1.21 for the reasons given in section 2.4.1.

On the lattice, the Coulomb condition is given by the gauge transformation matrix $G_{Coul}(x)$ which maximises the function [17]

$$F[G_{Coul}] = \sum_x \sum_t \mathrm{Tr} G_{Coul}(x) \left(U_i(x) G_{Coul}(x+\hat{i}) + U^\dagger(x-\hat{i}) G^\dagger_{Coul}(x-\hat{i}) \right), \tag{2.90}$$

separately on each time slice.

2.9 Correlator Fitting

2.9.1 Functional Form

Let $\mathcal{O}^\dagger_H(t)$ be an operator which creates an Υ meson at time t in the Heisenberg picture. Then an Υ propagating between times $t = 0$ and $t = t$ can be represented in the Heisenberg picture, where the states carry no time dependence, by the correlation

$${}_H\langle 0|\mathcal{O}_H(t)\mathcal{O}^\dagger_H(0)|0\rangle_H. \tag{2.91}$$

We can transform Eqn. 2.91 to the Schrödinger representation [57] where the states are time dependent. States in the two pictures can be related by

$$|n,t\rangle_S = \tau(t)|n\rangle_H \tag{2.92}$$

where the unitary operator τ in Euclidean space is

$$\tau(t) \equiv e^{-Ht}. \tag{2.93}$$

The operators in the two pictures are related by

$$\mathcal{O}_H(t) = \tau^\dagger(t)\mathcal{O}_S\tau(t). \tag{2.94}$$

Expression 2.91 thus transforms like

$$\begin{aligned} & {}_H\langle 0|\tau^\dagger(t)\mathcal{O}_S\tau(t)\mathcal{O}^\dagger_S|0\rangle_H \\ \equiv \quad & {}_S\langle 0, t=t|\mathcal{O}_S\tau(t)\mathcal{O}^\dagger_S|0, t=0\rangle_S. \end{aligned} \tag{2.95}$$

A complete set of energy eigenstates

$$\sum_{states} |n\rangle\langle n| = 1 \tag{2.96}$$

can be inserted into 2.95 giving

$$\begin{aligned}
& \sum_{states} {}_S\langle 0, t=t|\mathcal{O}_S\tau(t)|n\rangle\langle n|\mathcal{O}_S^\dagger|0, t=0\rangle_H \\
= & \sum_{states} {}_S\langle 0, t=t|\mathcal{O}_S e^{-E_n t}|n\rangle\langle n|\mathcal{O}_S^\dagger|0, t=0\rangle_H \\
= & \sum_{states} |\langle 0|\mathcal{O}_S|n\rangle|^2 e^{-E_n t}
\end{aligned} \tag{2.97}$$

where E_n is the energy of the state $|n\rangle$.

Therefore the general theoretical functional form of the correlator is

$$G_{th}(t; A_n, E_n) = \sum_{n=1}^{\infty} A_n e^{-E_n t} \tag{2.98}$$

where A_n is the matrix element $|\langle 0|\mathcal{O}_S|n\rangle|^2$ and the energies E_n are in order of increasing size. Therefore the higher the energy state, the more quickly its contribution decays. At large enough t, only the contribution from the ground state remains.

The *effective mass function* $m_{eff}(t)$ is defined as

$$m_{eff}(t) = -\ln\left(\frac{G(t+1)}{G(t)}\right), \tag{2.99}$$

and as $t \to \infty$, $m_{eff} \to E_0$ so a plot of m_{eff} against t should plateau at the ground state energy for large enough t, allowing E_0 to be determined.

2.9.2 Traditional Multi Correlation Fitting

The effective mass method is good for extraction of the ground state energy. However, an improved technique [55, 58] involving simultaneously fitting to correlations with different source and sink smearings whilst constraining the energies to be the same allows extraction of excited state energies and amplitudes.

Two separate types of improved fit can be done; row fits and matrix fit. The matrix fit involves simultaneously fitting to the $k \times k$ 'matrix' of correlators $G(n_{sc}, n_{sk}, t)$ with smearing numbers $n_{sc}, n_{sk} = loc, 1, .., k-1$. The functional form for such a fit is

$$G_{th}(n_{sc}, n_{sk}, t) = \sum_{n=1}^{N_{exp}} a(n_{sc}, n) a^*(n_{sk}, n) e^{-E_n t}, \tag{2.100}$$

where N_{exp} is the number of exponentials used in the fit.

In the case of a row fit we only fit to correlators with local smearing at the sink, i.e. the $k \times 1$ 'row' $G(n_{sc}, loc, t)$ with smearing numbers $n_{sc} = loc, 1, .., k-1$. The functional form in this case is

$$G_{th}(n_{sc}, loc, t) = \sum_{n=1}^{N_{exp}} b(n_{sc}, n) e^{-E_n t}. \tag{2.101}$$

The correlators $G^\alpha(t)$, where α represents a certain combination of source and sink smearings, are averaged over each configuration and each origin on each run to give

$$\overline{G^\alpha(t)} = \frac{1}{N_{conf} \times N_{orig}} \sum_{i=1}^{N_{conf}} \sum_{j=1}^{N_{orig}} G^\alpha(t). \tag{2.102}$$

where the general notation of Eqn. 2.98 has been used.

The fit then proceeds by varying A_n and E_n to minimise $\chi^2(A_n, E_n)$ where

$$\chi^2(A_n, E_n) \equiv \sum_{tt', \alpha\beta} \Delta G^\alpha(t) (\sigma^2)^{-1}_{t,t'} \Delta G^\beta(t') \tag{2.103}$$

and

$$\Delta G^\alpha(t) \equiv \overline{G^\alpha(t)} - G^\alpha_{th}(t; A_n, E_n). \tag{2.104}$$

The *covariance matrix* $\sigma^2_{t,t'}$ given by

$$\sigma^2_{tt',\alpha\beta} \equiv \overline{G^\alpha(t) G^\beta(t')} - \overline{G^\beta(t')} \overline{G^\alpha(t)} \tag{2.105}$$

is needed because the Monte Carlo algorithm results in correlations between data from successive time points or different choices of smearings.

Following the procedure in [60] the variance the j^{th} parameter $\sigma^2(a_j)$ can be determined as

$$\sigma^2(a_j) = \alpha^{-1}_{jj} \tag{2.106}$$

where the matrix $[\alpha]$ is given by

$$\alpha_{kl} = \sum_{tt', \alpha\beta}^{N} \frac{1}{\sigma^2} \left[\frac{\partial G}{\partial a_k} \frac{\partial G}{\partial a_l} \right]. \tag{2.107}$$

A measure of the quality of the fit can be determined [60] by calculating the *Incomplete Gamma Function*

$$Q(a,x) \equiv \frac{1}{\Gamma(a)} \int_x^\infty e^{-t} t^{a-1} dt \ (a > 0) \tag{2.108}$$

where $a = N_{df}/2$, N_{df} being the number of degrees of freedom, and $x = \chi^2/2$. The gamma function Γ is defined as

$$\Gamma(z) = \int_0^\infty t^{z-1} e^{-t} dt. \tag{2.109}$$

The quality of fit Q essentially determines the probability that a value as poor as χ^2_{min} could occur by chance for the correct model. Hence, the nearer Q is to 1, the better the fit. Generally, $Q > 0.1$ is regarded as being a good fit but smaller values can be deemed acceptable (but perhaps treated with caution) since poor fits are typically characterised by extremely small values of Q.

Another method of determining errors which is preferable when there are large correlations between the data (for example when determining the ratios of spin splittings) is *bootstrapping* [61].

Bootstrapping involves creating from the $N_{corr} = N_{conf} \times N_{orig}$ correlators N_{boot} sets of correlators where each set has the same number (N_{corr}) of members as the original set which each have been randomly chosen (with replacement) from the original set. The observable is determined on each set and the resulting values are sorted in order of increasing size. The error is then taken as half of the width of the central 68% of this spread.

Obviously, in practice we can not fit to an infinite number of parameters. Since the contributions from high energy states are suppressed exponentially at large t, it is possible to fit to a finite number of exponentials if the data is truncated such that the G values at low t are excluded, i.e. we only fit the data to $t \geq t_{min}$ where t_{min} is a chosen carefully to maximally suppress the high energy contributions whilst minimising the amount of redundant data.

Traditionally, this method has been used to simultaneously fit the Monte Carlo data from several differently smeared meson propagators to 2 or 3 exponentials to extract the amplitude and energy parameters. There have, however, been problems involved with doing this, including the fact that the fit errors grow as the choice of t_{min} increases resulting in large errors if t_{min} is chosen at all conservatively. However, more recently an improved approach involving constrained curve fitting has been implemented which allows the fitting of non-truncated data to an arbitrary large number of exponentials [62]. The latter method has been extensively used in this thesis.

2.9.3 Constrained Multi Exponential Fitting

The reason that the traditional fitting methods can not be used to fit to the whole range of data ($t_{min} = 0$) with a large number of exponentials is that the errors on the leading parameters become unreasonably large. This is due to the fact that the poorly constrained parameters related to the high energy terms wander off from their true values in the multi dimensional-parameter space, and this affects the error estimates for the better constrained low energy parameters.

The idea behind constrained curve fitting is the augmentation of χ^2 with a Bayesian term

$$\chi^2 \to \chi^2_{aug} \equiv \chi^2 + \chi^2_{prior} \tag{2.110}$$

where

$$\chi^2_{prior} \equiv \sum_n \frac{(A_n - \tilde{A}_n)^2}{\tilde{\sigma}^2_{A_n}} + \sum_n \frac{(E_n - \tilde{E}_n)^2}{\tilde{\sigma}^2_{E_n}}. \tag{2.111}$$

The χ^2_{prior} terms discourage the fitting algorithm from venturing outside the region $[\tilde{A}_n - \tilde{\sigma}_{A_n}, \tilde{A}_n + \tilde{\sigma}_{A_n}]$ for each amplitude, and the region $[\tilde{E}_n - \tilde{\sigma}_{E_n}, \tilde{E}_n + \tilde{\sigma}_{E_n}]$ for each energy of the fit. The *priors* $(\tilde{A}_n, \tilde{E}_n, \tilde{\sigma}_{A_n}\tilde{\sigma}_{E_n})$ are inputs to the fit which must be chosen with physical motivation.

The fit can then proceed as before, but now minimising χ^2_{aug}, to fit the entire range of data to an arbitrarily large number of exponentials.

Chapter 3

Upsilon Spectroscopy Lattice Results

3.1 Introduction

The configurations used in this thesis are a selection of those generated by the MILC collaboration [63].

The lattice spacings were tuned in generation of these ensembles using a dimensionful parameter associated with the static quark potential to be either $a = 0.13$fm ('coarse') or $a = 0.08$fm ('fine')[1].

Available are ensembles which have 2+1 flavours of dynamical quarks, with one quark mass being held at m_s, which is approximately (but not equal to) the value of the strange quark mass, and two degenerate flavors varying from m_s to $m_s/5$. Also available are quenched ensembles and a two flavor ensemble with degenerate dynamical quark masses of $m_s/2.5$.

The asqtad improved staggered action (which is $\mathcal{O}(a^2)$ improved) was used for the quarks and an $\mathcal{O}(\alpha a^2)$ Symanzik improved action was used for the gauge fields.

Table 3.1 shows which and how many configurations were used for results in this thesis, and the parameters used in the Υ correlator runs. I concentrated on the coarse ensembles and one dynamical fine ensemble was used to check for scaling violations. u_{0L} is the value of the landau link used for tadpole improvement, estimated from the u_{0P} values used by

[1] These lattice spacing values can not be taken as accurate, however, and the true values will be determined using Υ spectroscopy in this chapter.

Lattice	n_f	β	am_l, am_s	u_{0L}	aM_b^0	n	n_{conf}	n_{orig}
$20^3 \times 64$ coarse	0	8.0	-	0.856	2.3	4	210	8
					2.8	4	210	16
	2	7.2	0.02,-	0.845	2.8	4	210	16
	2+1	6.76	0.01,0.05	0.836	2.8	4	210	16
	2+1	6.79	0.02,0.05	0.837	2.8	4	210	16
	2+1	6.81	0.03,0.05	0.8378	2.8	4	210	16
	3	6.85	0.05,0.05	0.8391	2.8	4	210	8
	2+1	6.76	0.01,0.05	0.836	2.8	8	210	16
$28^3 \times 96$ fine	2+1	7.09	0.0062, 0.031	0.8461	1.95	4	159	16,12*
					2.1	4	92	16

Table 3.1: Parameters and details of MILC configurations used for Υ correlator calculations. *For 92 of the 159 configurations, data from 4 of the 16 origins was rejected due to corruption on the last timeslice of the configuration.

MILC. aM_b^0 is the bare b quark mass. As will be discussed in section 3.4, $aM_b^0 = 2.8$ and $aM_b^0 = 1.95$ are the best tuned values for the coarse and fine lattices respectively, and I concentrated on these runs in the analysis. n is the NRQCD stability parameter which was varied in one run to ensure that the results are n independent. n_{conf} and n_{orig} are the number of configurations and the number of meson origins used for each run respectively. Multiple origins were used to increase the statistics. In the case of $n_{orig} = 8$, 4 origins were maximally separated on each of the first and middle ($t = T/2$) timeslices and for $n_{orig} = 16$ there were also origins located on the $t = T/4$ and $t = 3T/4$ timeslices.

3.2 Fitting Results

3.2.1 Effective Mass plots

Figure 3.6 shows effective mass plots for the matrix of correlators in which each element has the smearing combination (n_{src}, n_{snk}) with (n_{src}) and (n_{snk}) each being *loc*, *g*, or *e*. As explained in the previous chapter, the effective mass should tend to the ground state energy of the channel at large t since the higher the energy of the state, the quicker the exponential fall-off of that state. The time taken to plateau at the ground state mass depends on the smearings used.

It can be seen that the (g, l) effective mass quickly reaches a plateau, indicating that the g smearing has a good overlap with the wavefunction of the ground state. The (e, l) effective mass takes longer to reach a plateau indicating a substantial contribution from the first excited Υ state as required.

The plateau value from any of the effective mass plots can be extracted to give a value for the ground state mass. However, instead multi-correlation multi exponential simultaneous fits are used to more effectively give this value in addition to values for excited state energies and amplitudes.

3.2.2 Standard and Bayesian Multi Correlation Fitting

In Figure 3.1, the results for E_0 and E_1 from a standard 2 exponential 2 smearing (g, e) simultaneous matrix fit are plotted against t_{min} where t_{max} is 31. This fit is for the $^3S_1$ channel using the $n_f = 2 + 1$ $m_l = 0.01$ coarse data. These values are tabulated in table B.21 along with the Q values of the fit. The errors from this and all other fits are statistical only.

Techniques for performing these fits and instructions on how to choose a best t_{min} are discussed in [54]. In this case we should drop the first 2 fits, $t_{min} = 2, 3$ as the Q values are below 0.1. We should then drop the next 2 fits, $t_{min} = 4, 5$ and take the subsequent $t_{min} = 6$ as the best fit.

Equivalant multi exponential Bayesian fits were done using the same 4 correlators. Figure 3.2 shows the results for the ground and first excited energy parameters. There is no varying of t_{min} or t_{max} since the whole range of t values are fitted to in the Bayesian case. Instead the results are plotted against the number of exponentials used in the fit, n_{exp}. We have fitted to $\ln E_0$ as opposed to E_0 in order to prevent the fit from venturing into unphysical negative energy space. Similarly, the higher energy parameters E_n have been replaced by the parameters $\ln(E_n - E_{n-1})$ to ensure correct ordering of energy states. The latter substitution also simplifies the procedure of allocating parameter guesses to the fitting program since the radial energy splittings in the Υ spectrum are fairly evenly spaced. The χ^2_{prior} (Eqn. 2.111) terms were taken for this fit (with similar values used for all other Bayesian fits in this thesis) as

$$\tilde{\hat{E}}_n = -1.1 \tag{3.1}$$

$$\sigma^2_{\tilde{\hat{E}}_n} = 0.7 \tag{3.2}$$

$$\tilde{A}_n = 0.1 \tag{3.3}$$

$$\sigma^2_{\tilde{A}_n} = 0.7 \tag{3.4}$$

where $\hat{E}_n$, as described above, is defined by

$$\hat{E}_n = \begin{cases} \ln(E_n)\ (n = 0) \\ \ln(E_{n+1} - E_n)\ (n > 0) \end{cases} \tag{3.5}$$

These specific values for the priors were chosen using rough estimates of the expected parameters and the above widths were chosen to be large enough that the fit was not overly constrained to these guesses.

The values E_0, E_1 and Q for this fit are tabulated in B.22.

The Q values for the $n_{exp} = 2, 3$ fits are low indicating that not enough energy parameters are available to account for the high energy contributions to the low t behavior of the correlators.

For $n_{exp} = 5, 6, 7, 8$ the fit has been unable to correctly resolve the higher energy parameters. Thus $n_{exp} = 4$ has been chosen as the best fit in this case. The results agree with those from the standard fit.

Figure 3.3 and table B.32 show results from the equivalent 3×3 matrix (*loc*, g and e smearing) fit. For similar reasons as above, the $n_{exp} = 7$ fit is chosen as the best. The results for this fit agree with the standard fit and the 2×2 Bayesian fit. With this fit, however, it is also possible to extract a 2nd excited energy parameter.

Table 3.2 shows which 2×2 Bayesian fits were performed for each dataset and which n_{exp} was chosen for the best fit in each case. In general the Q values obtained for these were good. Table 3.3 shows the equivalent information for the 3×3 Bayesian fits. Unfortunately, the Q values for these fits were in general not as high as ideally one would like. All fit results are tabulated in Appendix B.

S wave results

2×2 (g, e) Bayesian matrix fits on $^3S_1$ and $^1S_0$ correlators were performed for all runs and bare quark masses. This allowed determination of the ground and first excited energies. The best fit results are shown in table 3.4.

Equivalent 3×3 (l, g, e) fits were performed for all best tuned M_b^0. These fits allowed the determination of the ground and first 2 excited energies, and the ground and 1st excited wavefunction at the origin (see section 3.6). The best fit results are shown in tables 3.5 and 3.6 for the $^3S_1$ and $^1S_0$ channels respectively.

P wave results

2×2 (g, e) Bayesian matrix fits on $^1P_1$ correlators were performed for all runs and bare quark masses, allowing the determination of the ground and 1st excited state energies. The best fit results are shown in table 3.7.

2×2 Bayesian matrix fits on $^3P_0$, $^3P_1$ and $^3P_{2E}$ correlators were performed on the $n_f = 2 + 1$ $m_{light} = 0.01$ data. Note that these fits used only half the statistics of table 3.1 since data for 8 of the origins were lost before this analysis.

Equivalent fits were performed on the $n_f = 2 + 1$ $m_{light} = 0.02$ data (with full statistics), but results are only given for the $^3P_0$ and $^3P_{2E}$ channels since a good fit was unobtainable for the $^3P_1$ channel. The best fit results are shown in table 3.8.

D wave results

2×2 (l, g) Bayesian matrix fits on $^1D_2$, $^3D_{2E}$ and $^3D_{3A}$ correlators were performed on the $n_f = 2 + 1$ $m_{light} = 0.01$ data. The best fit results are shown in table 3.9.

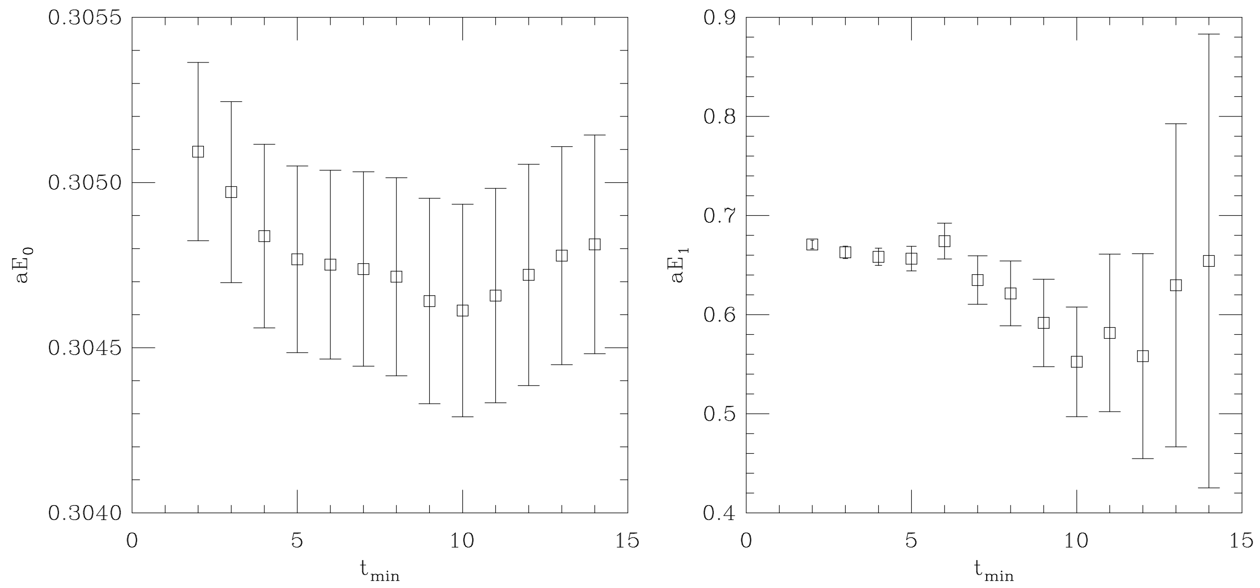

Figure 3.1: Results for the lowest 2 energy parameters from a standard 2×2 matrix fit to the $n_f = 2+1$ $m_{light} = 0.01$ coarse MILC data at $aM_b^0 = 2.8$.

Autocorrelation check

In the generation of the ensembles, a large enough number of Monte-Carlo time steps should have been chosen between accepted configurations such that only configurations independent of each other remain as members of the ensemble. If this is not the case then it is said that *autocorrelations* exist between the configurations.

It is possible to test for autocorrelations by binning correlator data over succesive configurations. If the correlators on an ensemble with n_{conf} configurations are $\{C_n\}$ $(n = 1..n_{conf})$, then a binned ensemble $\{C'_n\}$ $(n = 1..n_{conf}/2)$ can be created where $C'_n = (C_{2n-1} + C_{2n})/2$.

Autocorrelations would show up in a fit to the binned data by the shift of central values or resizing of errors.

2×2 Bayesian matrix fits were performed on such binned correlators for both the coarse ($n_f = 2+1$ $m_{light} = 0.01$) and fine configurations for the $^3S_1$ channel. The fitting results are shown in tables B.28 and B.74 respectively. The complete agreement with these to the unbinned configuration fits (tables B.22 and B.71) suggest that no autocorrelations exist.

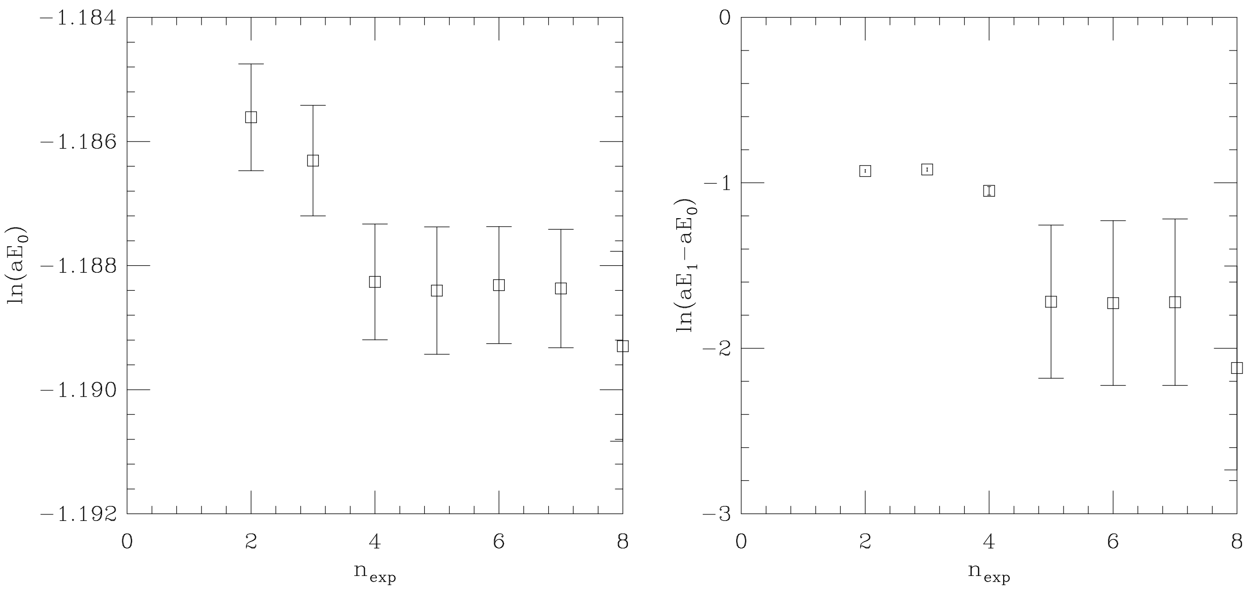

Figure 3.2: Results for the lowest 2 energy parameters from a Bayesian 2×2 matrix fit to the $n_f = 2+1$ $m_{light} = 0.01$ coarse MILC data at $aM_b^0 = 2.8$.

3.3 Fixing the Lattice Spacing

The lattice formulation is such that all calculated quantities are dimensionless. This has been done by the rescaling of fields in the Lagrangian by powers of the lattice spacing a, which has mass dimension -1. Thus a dimensionless energy splitting calculated on the lattice ΔE_{latt} relates to the physical energy splitting ΔE_{phys} by

$$\Delta E_{latt} = a\Delta E_{phys}. \tag{3.6}$$

Similarly,

$$A_{latt} = a^3 A_{phys}. \tag{3.7}$$

where A is an amplitude. Thus, in order to obtain physical results we must determine a^{-1}, multiply our lattice energy splitting by a factor a^{-1} and multiply our lattice amplitudes by a factor $(a^{-1})^3$.

The inverse lattice spacing is determined such that a physical quantity calculated on the lattice is matched to experiment. In the case of a correct lattice theory, the lattice spacing determined from any chosen physical quantity should agree with that from any other chosen

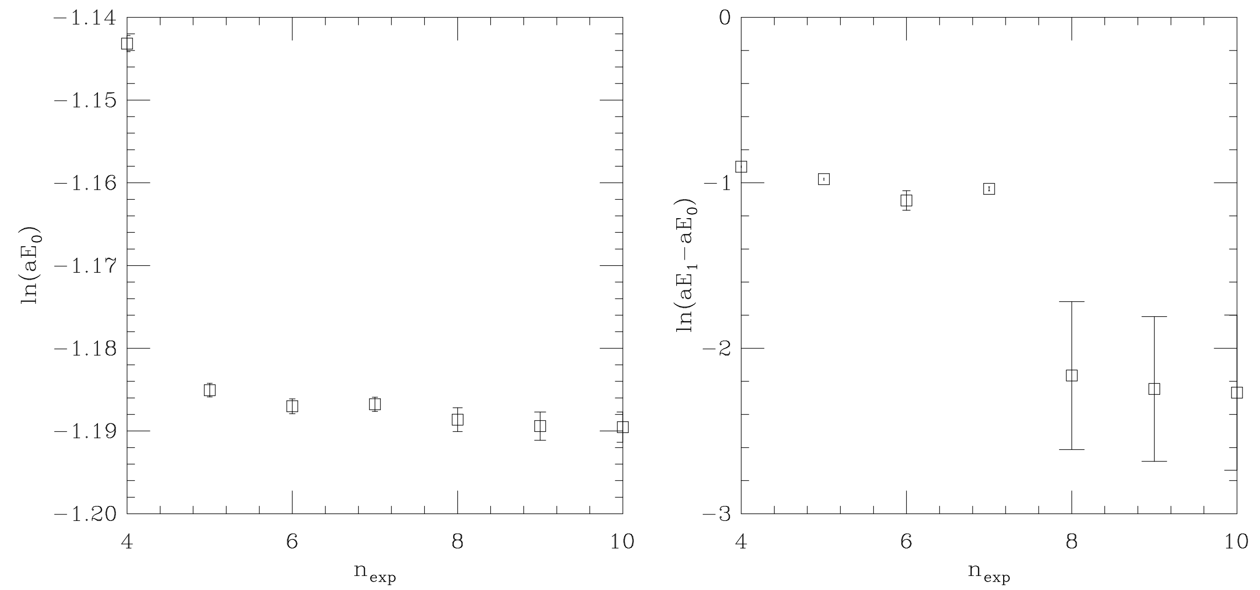

Figure 3.3: Results for the lowest 2 energy parameters from a Bayesian 3×3 matrix fit to the $n_f = 2+1$ $m_{light} = 0.01$ coarse MILC data at $aM_b^0 = 2.8$.

physical quantity. However, a major problem with lattice simulations in the past has been that quenching effects have caused this not to be the case, resulting in ambiguous results.

Here we choose the 2 separate physical quantities and determine the lattice spacing from both. Comparing these determinations is a way of probing the dynamical content of the configurations, as will be discussed in more detail in the next chapter.

The first chosen physical quantity is the $(h_b - \Upsilon)$ $({}^1P_1 - {}^3S_1)$ energy splitting. The h_b has not been found experimentally but it is expected to have the same mass as the spin average $\overline{\chi}_b$ of the ${}^3P$ states [2]

$$\overline{\chi}_b = \frac{\chi_0 + 3\chi_1 + 5\chi_2}{9}. \tag{3.8}$$

Therefore a^{-1} is determined through

$$a^{-1}(PS) = \frac{(E^{h_b} - E^{\Upsilon})_{latt}}{(E^{\bar{\chi}_b} - E^{\Upsilon})_{phys}}. \tag{3.9}$$

The second chosen physical quantity is the $(\Upsilon' - \Upsilon)$ $(2^3S_1 - 1^3S_1)$ energy splitting, and

[2]The reason for this expected equality is discussed in [36] and it has been tested in [54].

run	aM_b^0	n_{exp}								
		$^3S_1$	$^1S_0$	$^1P_1$	$^3P_0$	$^3P_1$	$^3P_{2E}$	$^1D_2$	$^3D_{2E}$	$^3D_{3A}$
Quenched	2.3	4	4	4	-	-	-	-	-	-
	2.8	4	4	4	-	-	-	-	-	-
$n_f = 2$	2.8	4	4	4	-	-	-	-	-	-
$m_l = 0.01$	2.8	4	4	4	4	4	4	4	4	4
$m_l = 0.02$	2.8	4	4	4	4	-	4	-	-	-
$m_l = 0.03$	2.8	4	4	4	-	-	-	-	-	-
$m_l = 0.05$	2.8	4	4	4	-	-	-	-	-	-
Fine	1.95	4	4	4	-	-	-	-	-	-
	2.1	4	4	4	-	-	-	-	-	-
$m_l = 0.01$,$n = 8$	2.8	4	4	4	-	-	-	-	-	-

Table 3.2: Details of 2×2 multi-exponential Bayesian matrix fits carried out and the number of exponentials which resulted in the best fit.

a^{-1} is determined through

$$a^{-1}(SS) = \frac{(E^{\Upsilon'} - E^{\Upsilon})_{latt}}{(E^{\Upsilon'} - E^{\Upsilon})_{phys}}. \tag{3.10}$$

The results for each run are summarized in table 3.10.

3.4 Fixing the Bare Quark Mass

When calculating using NRQCD, one must (as in QCD) fix the bare quark masses (which are free parameters of the theory). In Υ spectroscopy, there is only one such mass; the bare mass of the bottom quark M_b^0. This must be fixed such that calculated physical quantities match experiment.

This can be done by way of requiring that the meson mass M must equal the experimental Υ mass of 9.46GeV. The relativistic energy-momentum dispersion relation of the meson is given by

$$E^2(\mathbf{p}) = \mathbf{p}^2 + M^2, \tag{3.11}$$

run	aM_b^0	n_{exp}	
		$^3S_1$	$^1S_0$
Quenched	2.3	-	-
	2.8	6	7
$n_f = 2$	2.8	6	6
$m_l = 0.01$	2.8	7	7
$m_l = 0.02$	2.8	7	7
$m_l = 0.03$	2.8	6	7
$m_l = 0.05$	2.8	6	6
Fine	1.95	7	7
	2.1	-	-
$m_l = 0.01, n = 8$	2.8	7	6

Table 3.3: Details of 3×3 multi-exponential Bayesian matrix fits carried out and the number of exponentials which resulted in the best fit.

where $E(\mathbf{p})$ is the energy of the meson at momentum $\mathbf{p}$.

In the case of NRQCD it is always true that $\mathbf{p} << M$, so a binomial expansion can be used on Eqn. 3.11 giving

$$E(\mathbf{p}) = M_0 + \frac{\mathbf{p}^2}{2M_1} + \frac{\mathbf{p}^4}{8M_3} + \cdots . \tag{3.12}$$

In general, M_0 does not equal any of the masses appearing in higher order terms in the expansion since we have removed the energy scale M from the lattice simulation. Also, $M_1 \neq M_2$ when the series is truncated at a certain order due to the omission of higher order terms.

It has been common practice in the past to truncate the series Eqn. 3.12 including only the zeroth and first order in $\mathbf{p}^2$ terms and define the *kinetic mass* M_{kin} of the meson to be M_1. Then M_{kin} is given by

$$M_{kin} = \frac{\mathbf{p}^2}{2\left(E(\mathbf{p}) - E(\mathbf{0})\right)}, \tag{3.13}$$

and M_b^0 can then be set such that M_{kin} equals the experimental Υ mass.

run	aM_b^0	$^3S_1$ aE_0	aE_1	$^1S_0$ aE_0	aE_1
Quenched	2.3	0.26424(34)	0.6277(83)	0.23846(27)	0.6146(83)
	2.8	0.26606(25)	0.6198(65)	0.24457(20)	0.6104(67)
$n_f = 2$	2.8	0.29545(28)	0.633(11)	0.26873(22)	0.618(12)
$m_l = 0.01$	2.8	0.30475(28)	0.6552(90)	0.27354(21)	0.6452(90)
$m_l = 0.02$	2.8	0.30113(27)	0.6490(80)	0.27054(21)	0.6395(77)
$m_l = 0.03$	2.8	0.29826(28)	0.631(14)	0.26866(21)	0.623(13)
$m_l = 0.05$	2.8	0.29533(38)	0.641(23)	0.26640(29)	0.640(19)
Fine	1.95	0.23251(31)	0.4814(41)	0.20641(24)	0.4670(41)
	2.1	0.23656(38)	0.4803(52)	0.21132(29)	0.4678(51)
$m_l = 0.01$,$n = 8$	2.8	0.29390(29)	0.6454(89)	0.26225(21)	0.6352(88)

Table 3.4: Final results for S wave lattice energies from 2×2 matrix Bayesian fits.

Here, however, the improved method of [54] is instead used in which all higher order relativistic terms are retained by not peforming the expansion in $\mathbf{p}$ allowing M_{kin} to be defined by

$$E(\mathbf{p}) - E(\mathbf{0}) = \left(\mathbf{p}^2 + M_{kin}^2\right)^{1/2} - M_{kin}. \tag{3.14}$$

The kinetic mass is then given by

$$M_{kin} = \frac{\mathbf{p}^2 - (\Delta E(\mathbf{p}))^2}{2\Delta E(\mathbf{p})}, \tag{3.15}$$

where $\Delta E(\mathbf{p})$ is defined as

$$\Delta E(\mathbf{p}) = E(\mathbf{p}) - E(\mathbf{0}). \tag{3.16}$$

To allow the determination of M_{kin}, $^3S_1$ correlators at all momenta in the range

$$(p_x, p_y, p_z) = (-2..2, -2..2, -2..2) \tag{3.17}$$

in units of $2\pi/La$ were created, for which values of $\mathbf{p}^2$ can take

$$\mathbf{p}^2 = p_x^2 + p_y^2 + p_z^2 = 0, 1, 2, 3, 4, 5, 6, 8, 9, 12. \tag{3.18}$$

run	aM_b^0	$^3S_1$		
		aE_0	aE_1	aE_2
Quenched	2.8	0.26660(23)	0.6223(27)	0.889(11)
$n_f = 2$	2.8	0.29577(26)	0.6465(60)	0.875(23)
$m_l = 0.01$	2.8	0.30521(26)	0.6598(43)	0.890(16)
$m_l = 0.02$	2.8	0.30116(25)	0.6506(42)	0.873(20)
$m_l = 0.03$	2.8	0.29877(25)	0.6528(57)	0.9309(78)
$m_l = 0.05$	2.8	0.29611(33)	0.6512(56)	0.925(19)
Fine	1.95	0.23278(29)	0.4801(46)	0.699(13)
$m_l = 0.01, n = 8$	2.8	0.29434(26)	0.6473(49)	0.880(16)

Table 3.5: Final results for $^3S_1$ lattice energies from 3×3 matrix Bayesian fits.

The correlators at nonzero momenta $\mathbf{p}$ were divided by those at zero momenta using a jacknife method [61], for both $(n_{src}, n_{snk}) = (g, loc)$ and $(n_{src}, n_{snk}) = (e, loc)$ smearings. Then a traditional simultaneous vector fit was carried out on these *ratio* correlators yielding the ground state energy as $\Delta E(\mathbf{p})$. In figure 3.4, $\Delta E(\mathbf{p})$ is plotted against $\mathbf{p}^2$ for the $n_f = 2+1$ $m_l = 0.01$ coarse MILC data at $aM_b^0 = 1.8$. $\Delta E(\mathbf{p})$ can then be plugged in to Eqn. 3.15 in order to determine the kinetic mass for each $\mathbf{p}$.

Figure 3.5 plots M_{kin} vs $\mathbf{p}^2$ for all the available values of $\mathbf{p}^2$, for the $n_f = 2+1$ $m_l = 0.01$ coarse MILC data at $aM_b^0 = 2.8$. The lack of dependence allowed the determination of M_{kin} to proceed using only the ratio of $\mathbf{p}^2 = 1$ and $\mathbf{p}^2 = 0$ correlators for the remaining ensembles.

Results of the fits to various ratio correlators for each of above data sets are shown in appendix B. For each of these a value of t_{min}/t_{max} was chosen as the best fit and M_{kin} was calculated.

The kinetic mass results for each run are summarized in table 3.11, where $a^{-1}(PS)$ has been used to fix the lattice spacing.

For the quenched case, runs were done for $aM_b^0 = 2.3$ and $aM_b^0 = 2.8$. It can be seen that the former value yields a kinetic mass which is below the physical value of 9.46GeV while the latter case yields a kinetic mass which is in agreement. Since the coarse ensembles

run	aM_b^0	$^1S_0$		
		aE_0	aE_1	aE_2
Quenched	2.8	0.24471(19)	0.5925(51)	0.871(15)
$n_f = 2$	2.8	0.26903(20)	0.6318(57)	0.883(20)
$m_l = 0.01$	2.8	0.27377(20)	0.6473(41)	0.873(19)
$m_l = 0.02$	2.8	0.27055(20)	0.6326(40)	0.830(33)
$m_l = 0.03$	2.8	0.26885(20)	0.6216(62)	0.826(29)
$m_l = 0.05$	2.8	0.26677(26)	0.6329(67)	0.909(21)
Fine	1.95	0.20647(22)	0.4645(44)	0.667(15)
$m_l = 0.01, n = 8$	2.8	0.26254(19)	0.6486(32)	0.9381(62)

Table 3.6: Final results for $^1S_0$ lattice energies from 3×3 matrix Bayesian fits.

were designed to have similar lattice spacings, $aM_b^0 = 2.8$ was chosen for all runs on these lattices.

In the case of the fine ensemble, runs were done for $aM_b^0 = 1.95, 2.1$. The value of 1.95 yields a kinetic mass in agreement with experiment and thus was used in obtaining lattice results.

3.5 Bootstrapping Results for Spin Dependent Splittings

The terms in the lattice NRQCD hamiltonian 2.66 which give rise to the spin splittings are those which incorporate the Pauli spin matrix σ. The first such term

$$\frac{g}{8M^2}\sigma \cdot (\mathbf{\Delta}^{(\pm)} \times \tilde{\mathbf{E}} - \tilde{\mathbf{E}} \times \mathbf{\Delta}^{(\pm)}) \tag{3.19}$$

can be shown using potential model arguments to give rise to the P-state fine structure while similarly the second term

$$\frac{g}{2M}\sigma \cdot \tilde{\mathbf{B}} \tag{3.20}$$

gives rise to the hyperfine splitting [36].

run	aM_b^0	$^1P_1$	
		aE_0	aE_1
Quenched	2.3	0.5083(41)	0.784(15)
	2.8	0.5100(28)	0.779(11)
$n_f = 2$	2.8	0.5525(52)	0.783(23)
$m_l = 0.01$	2.8	0.5831(40)	0.815(14)
$m_l = 0.02$	2.8	0.5695(39)	0.791(15)
$m_l = 0.03$	2.8	0.5601(57)	0.782(34)
$m_l = 0.05$	2.8	0.5584(61)	0.814(27)
Fine	1.95	0.4268(27)	0.6214(46)
	2.1	0.4275(38)	0.5995(73)
$m_l = 0.01$,$n = 8$	2.8	0.5726(39)	0.807(13)

Table 3.7: Final results for $^1P_1$ lattice energies from 2×2 matrix Bayesian fits.

run	aM_b^0	$^3P_0$		$^3P_1$		$^3P_{2E}$	
		aE_0	aE_1	aE_0	aE_1	aE_0	aE_1
$m_l = 0.01$	2.8	0.5679(56)	0.791(26)	0.5851(58)	0.813(22)	0.6004(62)	0.801(32)
$m_l = 0.02$	2.8	0.5526(34)	0.787(15)	-	-	0.5794(42)	0.806(15)

Table 3.8: Final results for ^3P lattice energies from 2×2 matrix Bayesian fits.

The power counting rules of section 2.4.1 can be used to show that these terms are down by a factor of v^2 on the leading order terms which introduces an relativistic error of $\mathcal{O}(10\%)$ to the spin dependent splittings in the case of the Υ.

Also present are errors of $\mathcal{O}(\alpha_S v^4)$. However, the ratio of the spin splitting in the first excited state to that in the ground state removes this uncertainty (which is there due to the lack of matching to a higher order in v) from the coefficients of the above terms.

Inspection of tables 3.4, 3.8 and 3.9 shows that the splittings between states with same L but different S quantum numbers cannot be naively resolved due to the size of the errors. However, correlators with a certain L quantum number are highly correlated with each other. Bootstrapping can be used, as explained in section 2.9.2, to greatly reduce these

run	aM_b^0	$^1D_2$		$^3D_{2E}$		$^3D_{3A}$	
		aE_0	aE_1	aE_0	aE_1	aE_0	aE_1
$m_l = 0.01$	2.8	0.7543(75)	1.129(13)	0.7518(79)	1.123(13)	0.7576(84)	1.156(15)

Table 3.9: Final results for D wave lattice energies from 2×2 matrix Bayesian fits.

run	aM_b^0	$a^{-1}(PS)$(GeV)	$a^{-1}(SS)$(GeV)
Quenched	2.3	1.805(30)	1.585(22)
	2.8	1.808(21)	1.583(12)
$n_f = 2$	2.8	1.714(35)	1.605(27)
$m_l = 0.01$	2.8	1.584(27)	1.588(19)
$m_l = 0.02$	2.8	1.640(24)	1.611(19)
$m_l = 0.03$	2.8	1.684(37)	1.590(25)
$m_l = 0.05$	2.8	1.678(39)	1.586(25)
Fine	1.95	2.267(31)	2.276(42)
	2.1	2.272(36)	2.311(50)
$m_l = 0.01$, $n = 8$	2.8	1.579(22)	1.595(22)

Table 3.10: Final results for the inverse lattice spacing determined from both the $1^1P_1 - 1^3S_1$ and $2^3S_1 - 1^3S_1$ splittings.

errors provided that the same bootstrap ensembles of configurations are used for each L wave fit.

For each 2×2 matrix fit performed in section 3.2.2 for the relevant channels, an equivalent bootstrap fit was performed (with the exception of the poorly tuned M_b^0 data) at the chosen best n_{exp}.

Tables 3.12, 3.13, and 3.14 show the results for the S, P and D wave spin dependent splittings respectively. Shown are results for the ratios of excited to ground state splittings and the absolute values for such splittings.

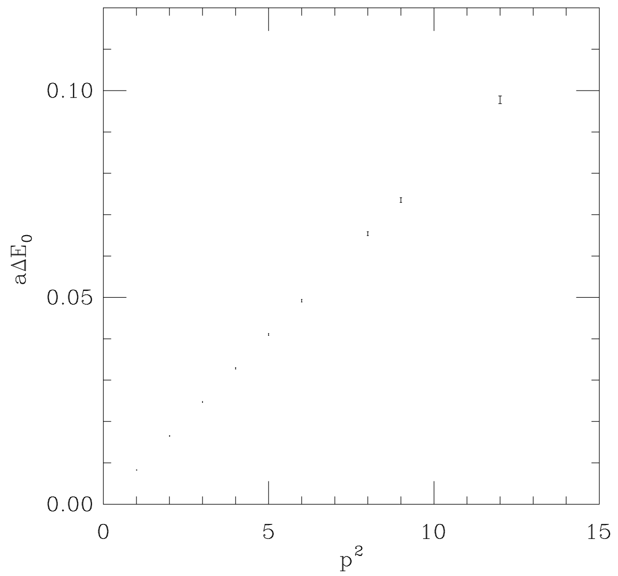

Figure 3.4: The energy difference of nonzero and zero momentum Υ correlators in lattice units plotted against the squared lattice momenta for the $n_f = 2+1$ $m_l = 0.01$ coarse MILC data at $aM_b^0 = 2.8$.

3.6 Wavefunction at the Origin Results

An important physical quantity which can be calculated on the lattice is the Υ *leptonic width*, Γ_{ee}, the decay width for the process of the b and $\bar{b}$ quarks annihilating to create a virtual photon which in turn creates a pair of leptons. This is precisely the time reversed process of how an Υ is created in e^+e^- colliders as shown in Figure 2.2.

At lowest order in v, $\Gamma_{ee}(nS)$, the leptonic width of $\Upsilon(nS)$, is given by [64]

$$\Gamma_{ee}(nS) = 16\pi\alpha_{em}^2 e_b^2 \frac{|\psi_n(0)|^2}{M_{\Upsilon(nS)}^2} Z_{match}^2 \tag{3.21}$$

$\alpha_{em} = 1/137$ is the electromagnetic coupling constant, $e_b = -1/3$ is the electric charge of the b quark, and Z_{match} is a matching factor between the lattice and continuum renormalisation schemes. At tree level $Z_{match} = 1$ and a preliminary calculation for a perturbative determination of Z_{match} to 1-loop (and matching factors for the currents which contribute to Γ_{ee} ar higher orders in v) is discussed in chapter 6.

The *wavefunction at the origin* $\psi_n(0)$, the overlap of the local current with the state n,

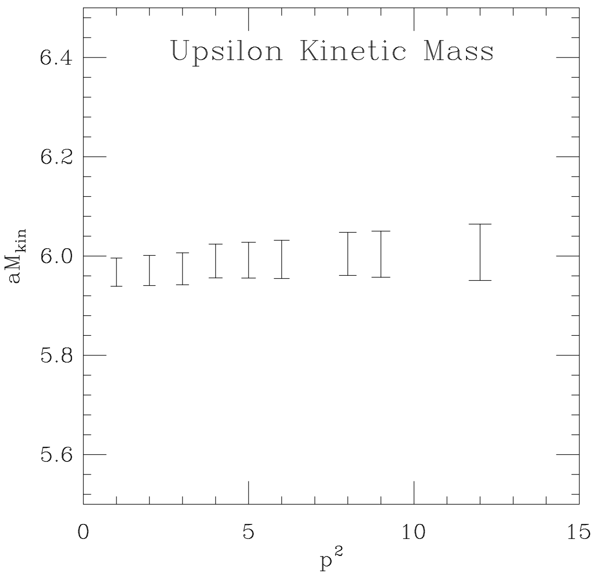

Figure 3.5: The value of the kinetic mass in lattice units plotted against the squared lattice momenta for the $n_f = 2+1$ $m_{light} = 0.01$ coarse MILC data at $aM_b^0 = 2.8$.

is given by

$$\psi_n(0) = \langle n|loc\rangle = \langle n| \sum_{\mathbf{x}} \psi^\dagger(\mathbf{x})\Omega\chi^\dagger(\mathbf{x})|0\rangle, \tag{3.22}$$

which is a matrix element which we can extract from our lattice simulation, where the meson operator $\Omega = \hat{I}, \sigma_i$ for ${}^1S_0$ and ${}^3S_1$ channels respectively as described in section 2.8.1.

If $\mathcal{S}_H(t)$ is an Heisenberg representation operator which creates an S wave meson at time t, then the correlator

$$_H\langle 0|\mathcal{S}_H(t)\mathcal{S}_H^\dagger(0)|0\rangle_H, \tag{3.23}$$

which represents the propagation of an S wave meson from time 0 to t, becomes in the Schrödinger representation (c.f. section 2.9.1)

$$\sum_{states} \langle loc|n\rangle\langle n|loc\rangle e^{-E_n t}. \tag{3.24}$$

Therefore, with local smearings $(n_{src}, n_{snk}) = (loc, loc)$, it can be seen from Eq. 2.100 that

$$\psi_n^{latt}(0) = a^{3/2}\psi_n^{phys}(0) = \langle n|loc\rangle = a(loc, n) \tag{3.25}$$

run	aM_b	t_{min}/t_{max}	M_{kin}(GeV)
Quenched	2.8	14/31	9.34(16)
	2.3	10/31	8.80(15)
$n_f = 2$	2.8	12/31	10.07(20)
$m_l = 0.01$	2.8	14/31	9.45(14)
$m_l = 0.02$	2.8	12/31	9.74(15)
$m_l = 0.03$	2.8	11/31	9.98(22)
$m_l = 0.05$	2.8	11/31	9.91(24)
Fine	1.95	11/31	9.67(16)
	2.1	11/31	10.16(17)
$m_l = 0.01$, $n = 8$	2.8	12/31	9.35(14)

Table 3.11: Kinetic Mass for $\mathbf{p}^2 = 1$ in units of $2\pi/La$ using $P - S$ splitting to fix a.

and the wavefunction at the origin of the n_{th} state is given by the n_{th} (loc, loc) amplitude of our matrix fit.

The results for $\psi_n(0)$ for the $^3S_1$ and $^1S_0$ channels are given in appendix B. The best fit values are given in table 3.15. Note that no results are given for 2×2 fits as no local smearing correlators were used in these.

These results will be analysed further in the next chapter.

Run	Ma_b^0	$^3S_1$-$^1S_0$		
		rat	gnd	ex
Quenched	2.8	0.433(65)	0.021487(90)	0.0093(14)
$n_f = 2$	2.8	0.58(14)	0.02673(12)	0.0156(36)
$m_l = 0.01$	2.8	0.320(76)	0.03121(14)	0.0099(24)
$m_l = 0.02$	2.8	0.310(82)	0.03059(13)	0.0095(25)
$m_l = 0.03$	2.8	0.26(13)	0.02960(13)	0.0078(38)
$m_l = 0.05$	2.8	0.09(30)	0.02894(18)	0.0029(88)
Fine	1.95	0.55(11)	0.02610(16)	0.0144(29)
$m_l = 0.01$, $n = 8$	2.8	0.323(76)	0.03165(14)	0.0102(24)

Table 3.12: Final results for S wave fine structure in lattice units from 2×2 matrix bootstrapped Bayesian fits.

Run	$^3P_1 -^3 P_0$			$^3P_{2E} -^3 P_0$		
	rat	gnd	ex	rat	gnd	ex
$m_l = 0.01$	1.06(45)	0.0164(18)	0.0174(78)	0.29(59)	0.0325(57)	0.009(17)
$m_l = 0.02$				0.71(21)	0.0268(22)	0.0189(60)

Table 3.13: Final results for P wave fine structure in lattice units from 2×2 matrix bootstrapped Bayesian fits.

Run	$^1D_2 -^3 D_{2E}$			$^3D_{3A} -^3 D_{2E}$		
	rat	gnd	ex	rat	gnd	ex
$m_l = 0.01$	2.1(64)	0.0025(56)	0.0053(59)	5.7(62)	0.0057(54)	0.033(11)

Table 3.14: Final results for D wave fine structure in lattice units from 2×2 matrix bootstrapped Bayesian fits.

run	aM_b^0	$^3S_1$		$^1S_0$	
		$a^{3/2}\psi_0(0)$	$a^{3/2}\psi_1(0)$	$a^{3/2}\psi_0(0)$	$a^{3/2}\psi_1(0)$
Quenched	2.8	0.26266(43)	0.2487(20)	0.28502(47)	0.2416(58)
$n_f = 2$	2.8	0.28610(56)	0.255(33)	0.31446(54)	0.2631(33)
$m_l = 0.01$	2.8	0.30203(55)	0.2436(50)	0.33414(56)	0.2556(51)
$m_l = 0.02$	2.8	0.29825(58)	0.2396(48)	0.32980(57)	0.2456(42)
$m_l = 0.03$	2.8	0.29554(57)	0.2543(36)	0.32655(55)	0.2459(59)
$m_l = 0.05$	2.8	0.29232(68)	0.2528(34)	0.32256(68)	0.2599(43)
Fine	1.95	0.17593(47)	0.1373(36)	0.21152(46)	0.1505(42)
$m_l = 0.01$,$n = 8$	2.8	0.30466(57)	0.2461(55)	0.33919(46)	0.234(38)

Table 3.15: Final results for the wavefunction at the origin from 3×3 matrix Bayesian fits.

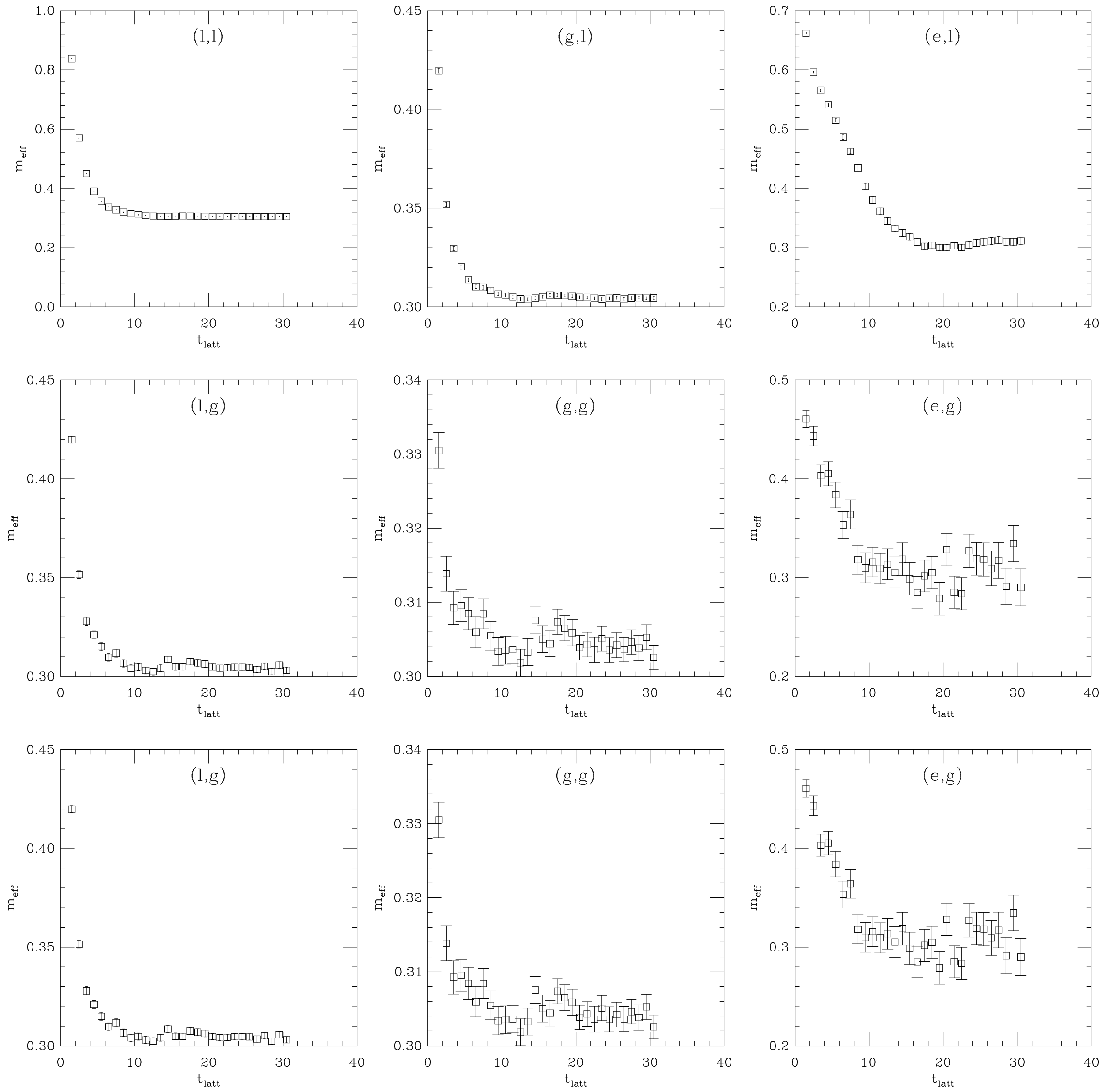

Figure 3.6: Effective mass plots with the use of smearing (n_{src}, n_{snk}) for the $n_f = 2 + 1$ $m_{light} = 0.01$ coarse MILC data at $aM_b^0 = 2.8$.

Chapter 4

Physical Results

4.1 Introduction

In this chapter the results of the previous section are analysed in order to compare with experiment and to provide information about the dynamical content of the configurations, in what is an updated version of the results presented at the LAT02 meeting in Boston [65].

The results for the lattice spacing determined from the radial and orbital splittings are compared with each other and with those determined from the static quark potential to reveal information about the dynamical content of the configurations and to obtain a value for r_0.

The spin independent and dependent results are compared with each other and experiment, as are results for the leptonic width.

Section 4.4 includes results from our collaborators at Ohio State University, Fermi National Accelerator Laboratory, Simon Fraser University and Cornell University (HPQCD).

4.2 Inverse Lattice Spacing Comparison and Determination of r_0

As explained in the previous chapter, the lattice spacing is fixed by the choice of β but it is not determined until after the simulation when a physical quantity is matched to experi-

run	$r_0 = 0.5fm$		$r_0 = 0.466fm$	
	$\frac{a_{\Upsilon}^{-1}(PS)}{a_{r_0}^{-1}}$	$\frac{a_{\Upsilon}^{-1}(SS)}{a_{r_0}^{-1}}$	$\frac{a_{\Upsilon}^{-1}(PS)}{a_{r_0}^{-1}}$	$\frac{a_{\Upsilon}^{-1}(SS)}{a_{r_0}^{-1}}$
Quenched	1.245(14)	1.087(14)	1.160(13)	1.013(13)
$n_f = 2$	1.145(20)	1.078(20)	1.067(19)	1.004(19)
$m_l = 0.01$	1.070(14)	1.077(14)	0.997(13)	1.003(13)
$m_l = 0.02$	1.087(13)	1.068(13)	1.013(12)	0.995(12)
$m_l = 0.03$	1.117(25)	1.055(17)	1.041(23)	0.983(15)
$m_l = 0.05$	1.110(26)	1.050(20)	1.034(25)	0.979(19)
Fine	1.081(15)	1.086(20)	1.007(14)	1.012(19)

Table 4.1: Ratios of inverse lattice spacings determined by Υ splittings to those determined using r_0.

ment. Once the lattice spacing has been set in this way it can be used to give dimensionful predictions for other observables.

Obviously, there should be only one real value for the lattice spacing and therefore it should not matter which energy splitting is used in fixing it. However, it has been a long known problem that in fact this is often not the case in lattice simulations due to the use of unrealistic dynamical fermion content. This gives ambiguities in calculating physical observables as it is impossible to say what the 'right' lattice spacing is.

Determinations of the lattice spacing from different splittings can be used as a guide to how good the dynamical quark content of the configurations being used are [1]. In this thesis the orbital ($^1P_1 -^3 S_1$) (PS) and radial ($2^3S_1 - 1^3S_1$) (SS) energy splittings were chosen to independently fix the lattice spacing, and the results were given in table 3.10.

The lattice spacing can be fixed another way using the static quark potential [66]. The force $F(r)$ between static quarks can be calculated precisely on the lattice. Therefore, if a hadronic length scale $R(c)$ is defined via the relation

$$R(c)^2F(R(c)) = c \tag{4.1}$$

[1]This is because, in a quenched theory where the coupling runs incorrectly, physical quantities probing different scales will have lattice artefacts dependent on the scale.

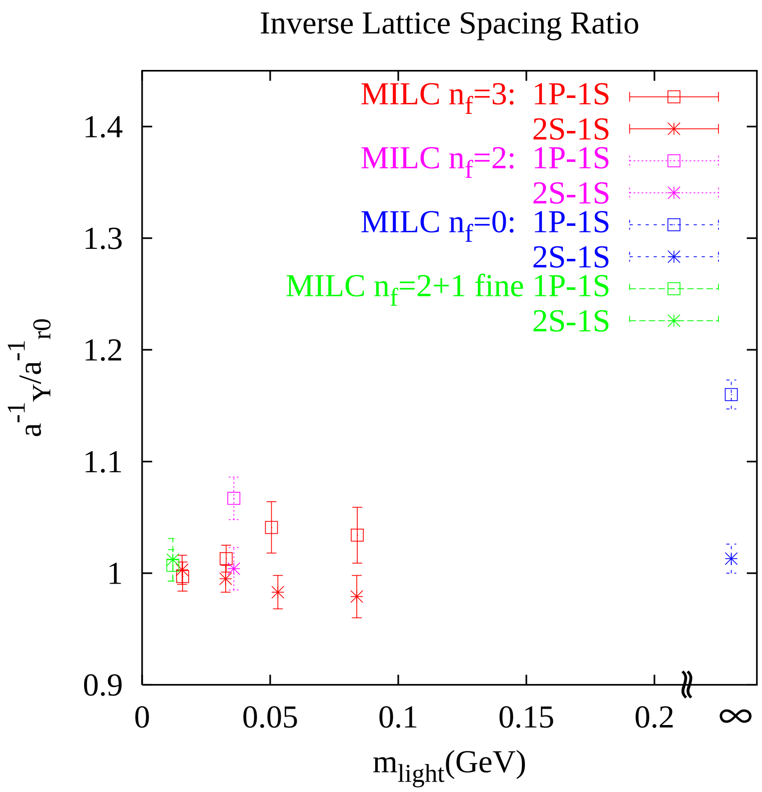

Figure 4.1: The ratio of the inverse lattice spacing obtained from the Υ spectrum to that obtained from the static quark potential using $r_0 = 0.466$fm, plotted against the bare light dynamical quark mass. Open squares represent scales determined from the 1P-1S splittings and bursts represent scales determined from the 2S-1S splittings.

where c is a dimensionless parameter, then the scale can be set if a physical value of $R(c)$ at a certain c is known. c is chosen to be 1.65 and $R(1.65)$ is known as r_0. The value of r_0 is not known accurately but from potential models (eg the Cornell [67] and Richardson [68] models) it is thought that $r_0 \sim 0.5$fm.

The scale was set in this way by MILC and the values $a^{-1}r_0$ are given in [63]. $a_{r_0}^{-1}$ was determined by setting r_0 equal to 0.5fm and the Υ inverse lattice spacings were divided by the r_0 inverse lattice spacings. The results for these ratios are shown in table 4.1.

It can be seen that these ratios are greater than one in the case of the most chiral (and hence most realistic) coarse and fine ensembles, suggesting that $r_0 < 0.5$fm. r_0 was varied until the ratio $a_\Upsilon^{-1}(PS)/a_{r_0}^{-1}$ for the most chiral coarse ensemble became in agreement with one in order to determine a value for r_0. An error on r_0 was also determined in this way and the result is

$$r_0 = 0.466(9)\text{fm}. \tag{4.2}$$

This was also done for the $m_l = 0.02$ $N_f = 2+1$ and fine ensembles with the results agreeing with the above value.

Thus r_0 was set to 0.466fm and the ratios were again calculated, with the results given also in 3.10 and illustrated in Figure 4.1. The ordinate gives values of the inverse lattice spacing a^{-1} obtained from both the Υ PS and SS splittings. The abscissa gives the mass of the light dynamical quarks used in the simulation in physical units. Thus as m_{light} decreases toward the physical chiral limit, the simulation is more realistic. It is clearly seen that there is an ambiguity in a^{-1} from the different splittings in the quenched case. This ambiguity is seen to disappear with unquenching and decreasing m_{light}. For the most chiral 2+1 flavour coarse and fine results, which agree indicating that these results are scale independent, the scales have completely converged suggesting that these configurations have realistic dynamical quark content.

4.3 Spin Independent Spectrum Comparison

Using the SS inverse lattice spacings from table 3.10, and the lattice energies from tables 3.5 and 3.7, determinations were made of the spin independent $3^3S_1 - 1^3S_1$, $1^1P_1 - 1^3S_1$, $2^1P_1 - 1^3S_1$ energy splittings in GeV. Figure 4.2 plots the results for the coarse ensembles along with the experimental values (where, as explained in the previous chapter, the $\bar{\chi}_b$ has been used to replace the unobserved h_b).

The ordinate gives values of the splitting and the abscissa gives the physical mass of the light dynamical quarks used in the simulation. Good agreement with experiment is seen as the chiral limit is approached and the flatness of the approach indicates that chiral extrapolations would have little effect on shifting the results from the most chiral ensemble.

Figure 4.6 shows the spin independent Υ spectrum. The dotted lines are the experimental values, including the recently observed ${}^3D_2$ channel. The $1S$ and $1P$ values have been fixed by the fixing of the kinetic mass and the use of the PS inverse lattice spacings from table 3.10 respectively. The ${}^1P_1$ and ${}^3S_1$ lattice energies from tables 3.5 and 3.7 along with the

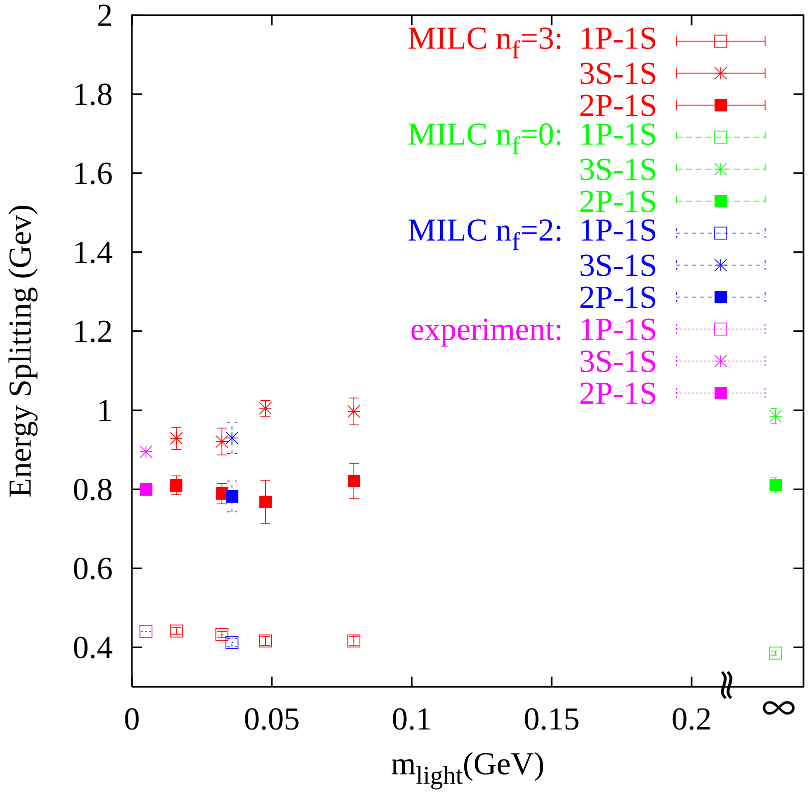

Figure 4.2: Spin independent energy splittings from the coarse MILC lattice results and experiment. Open squares, bursts and closed squares represent $1^1P_1 - 1^3S_1$, $3^3S_1 - 1^3S_1$, and $2^1P_1 - 1^3S_1$ splittings respectively.

$^3D_2$ ground state energy from table 3.9 have been used for the most chiral dynamical and quenched coarse ensembles and the fine ensemble. The quenched results clearly do not agree with experiment whereas the coarse dynamical results do. This shows that the quenching problem has been resolved for these splittings at least. It can be seen that in the case of the fine lattice, discrepencies exist with the higher energy splittings. This may be a problem with low statistics. More configurations should be used on this fine ensemble to increase the statistics and runs should be done on other fine ensembles to investigate this issue further.

4.4 Other Improved Staggered Results

The spin independent energy splitting results from the previous section have been presented along with other results from the High Precision QCD (HPQCD) collaboration in [69]. These

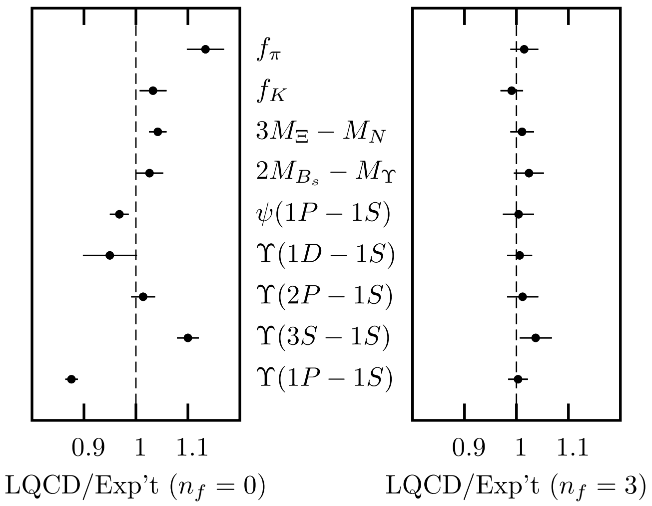

Figure 4.3: The ratio of lattice results for energy splittings and decay constants to experiment. The results are for quenched simulations (left) and simulations incorporating 2+1 flavours of dynamical quarks (right). The top three results are from coarse and fine lattice simulations while the rest are from the coarse lattice simulations.

combined results encompass a wide variety of nonperturbative calculations which give encouraging agreement with experiment.

The chosen quantities are restricted to those which are accurately measured experimentally, are stable and are single-hadron states. The latter 2 restraints are imposed because unstable particles and multi-hadron states (e.g. non-leptonic decay products) constantly fluctuate into on-shell and nearly on-shell decay products which can propagate to the boundaries of the lattice introducing finite volume errors.

Along with the Υ, the J/ψ ($c\bar{c}$), B_s ($s\bar{b}$), K ($u\bar{s}$), π ($u\bar{d}$), N (uud), and Ξ (uss) particles were chosen as suitable. m_Υ was used to set the b quark mass as explained in the previous chapter. The u, d, s and c quark masses also needed to be set to determine physical properties of hadrons which have these as valence particles. m_u was set to equal m_d in generating the configurations and this equality must also hold for the analysis.

The physical quantities m_π^2, $m_K^2 - m_\pi^2$ and m_{D_s} were used to fix the masses of u/d, s and c respectively. The $\Upsilon(2S) - \Upsilon(1S)$ splitting was used to fix the lattice spacing.

Figure 4.3 shows the results for quantities calculated in addition to those used for tuning the bare parameters. Plotted is the ratio of the lattice result to the experimentally measured value for a variety of quantities; the π and K meson decay constants, the $\Xi - N$ baryon mass splitting and various meson mass splittings involving the B_s, J/ψ and Υ (including those presented in the previous section). The quenched results are shown on the left whilst the $n_f = 2 + 1$ dynamical results are shown on the right. The quenched results deviate from experiment by 10-15% (which can increase to 20-30% with a different choice of tuning parameters) while the dynamical results agree with experiment to within systematical and statistical errors of 3% or less.

The light quark (top four) quantities in the plot required extrapolations in the dynamical and valence quark masses, and this was the source of the dominant uncertainty in their values. Chiral perturbation theory (for an introduction to this subject see [70]) was used to correct the u, d quark masses while linear interpolation was used to correct the s quark mass.

The remaining quantities depend much less on the light quark masses and provide more stringent tests of lattice QCD. In particular, the Υ splittings provide especially good tests since they are largely independent of the valence quark masses [71].

These results demonstrate that lattice NRQCD is an accurate and effective tool for calculating heavy quark dynamics using no free parameters in addition to those from QCD, and the improved staggered formulation is a useful tool enabling the simulation of quarks light enough to reach the region where chiral perturbation theory is applicable.

4.5 The Spin Dependent Spectrum

The bootstrap fit results from section 3.5 can be used to obtain results for spin dependent energy splittings.

Hyperfine Splitting

The hyperfine splitting between the Υ and η_b depends on spin dependent terms in the action, and if calculated directly at the order to which we are working with ($\mathcal{O}(v^4)$) it is only accurate to around 10%. Also present are $\mathcal{O}(\alpha_S v^4)$ errors. To get these errors down to the level of spin independent quantities such as the 2S-1S or 1P-1S splittings, around 1%, the action

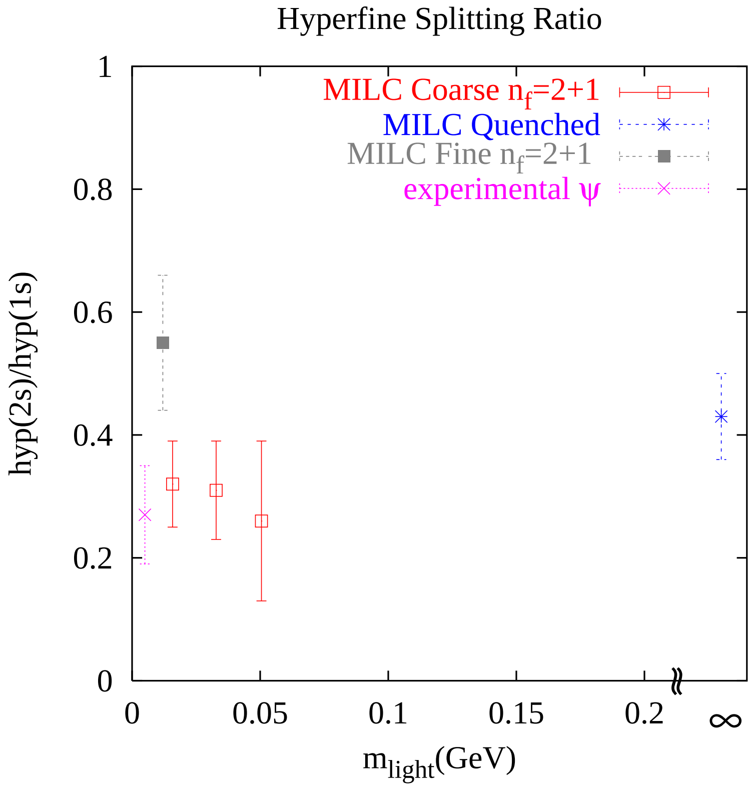

Figure 4.4: The ratio of hyperfine splitting for the 1st excited state of the Υ to that of the ground state. The open squares and closed square represent the results for the $n_f = 2+1$ dynamical coarse ensembles and fine ensemble respectively. The burst represents the quenched result and the cross represents the current experimental result for the ψ system.

must be improved to $(\mathcal{O}(v^6))$ with one loop matching and this should be done in the future. However, if we take ratios the $\mathcal{O}(\alpha_s)$ corrections to the $\sigma \cdot \mathbf{B}$ term cancel which removes a lot of the uncertainty.

Plotted in Figure 4.4 are results from table 3.12 showing the ratio of hyperfine splitting of the 1st excited to that of the ground Υ state. The results for the $n_f = 2$ and $n_f = 3, m_l = 0.05$ ensembles had large errors and are not plotted.

The hyperfine splitting, in leading order in a potential model, is proportional to $|\psi(0)|^2$. Thus similarly to the leptonic width (see next section), a lot of the heavy quark mass dependence cancels in the ratio.

Therefore, since η_b and η_b' are experimentally as yet unseen we compare with the experimental result for the ψ system using recent results for the η_c' from the BELLE collaboration

[72]. Note that since there will still be some mass dependence left in the ratio, the results do not have to completely agree with the experimental point for ψ. The plot does however show a tendency to experiment with unquenching. The fine lattice result for this ratio lies above the coarse lattice result. This may be a sign of discretisation errors in this quantity but, as previously discussed, more work should be done with the fine ensembles.

Figure 4.7 shows lattice predictions for the physical ground and excited state hyperfine splittings. The dotted lines are the experimental values. The results for the most chiral dynamical and quenched coarse ensembles are from table 3.12 and the PS inverse lattice spacings from table 3.10 have been used. A clear shift with unquenching is seen for the ground splitting. Note, as discussed, that these non ratio results have larger systematic errors that the ratio results.

P and D Wave Splittings

Figure 4.8 shows lattice predictions for the physical ground and excited state P wave splittings and ground state D wave splittings. The dotted lines are the experimental values. Shown are results from the most chiral dynamical coarse ensembles from tables 3.13 and 3.14 for P and D waves respectively. The quenched results are from a UKQCD ensemble at $\beta = 6.0$ [73]. Again the PS inverse lattice spacings from table 3.10 have been used. It is clear that the dynamical results are in much better agreement with experiment than the quenched results. Again, these non ratio results have larger systematic errors that the ratio results.

4.6 Upsilon Leptonic Width Ratios

The $\Upsilon(nS)$ leptonic width (width of decay to leptons), Γ_{ee}, is found by squaring the matrix element of the current which destroys an Υ,

$$\Gamma_{ee}(nS) \propto \langle \Upsilon_n \,|\, J_{cont} \,|\, 0 \rangle^2 \,. \tag{4.3}$$

When working on the lattice, the continuum current J_{cont} must be constructed from

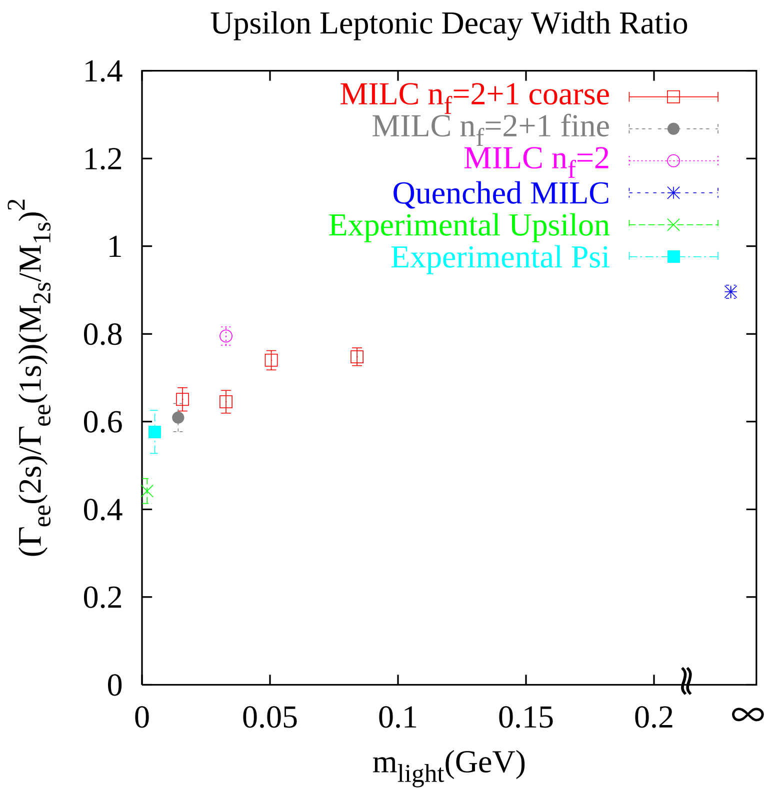

Figure 4.5: The ratio of leptonic width for the 1st excited state of the Υ to that of the ground state. The open squares and open circle represent results for dynamical coarse 3 and 2 flavour configurations respectively while the burst represents the quenched result. The closed circle represents the fine lattice result. The cross and closed square represent the current experimental results for Υ and ψ respectively.

lattice operators,

$$J_{cont} = \sum_i Z^i_{match} J^i_{latt}, \tag{4.4}$$

where J^i_{latt} is a current of order v^{2i}, with v the quark velocity.

Z^i_{match} is a renormalisation constant for matching between the lattice and continuum schemes.

As was explained in section 3.6, if only J_1 is considered, these matrix elements can be extracted from the wavefunction at the origin $\psi_n(0)$ which equals the n_{th} amplitudes of our 3×3 fits where local (delta function) smearings have been used in creation and destruction.

Then, it can be seen from Eqn. 3.21 that

$$\frac{\Gamma_{ee}(2S)}{\Gamma_{ee}(1S)} = \frac{|\psi_2(0)|^2}{|\psi_1(0)|^2}\frac{M^2_{\Upsilon(1S)}}{M^2_{\Upsilon(2S)}} \tag{4.5}$$

and the Z_{match} factor for this current, which must be calculated in perturbation theory, cancels in the ratio.

Figure 4.5 uses the wavefunction at the origin results from table 3.15 to show the ratio of leptonic width of the 1st radially excited Υ to that of the ground state Υ. The ratio is clearly falling with dynamical mass and unquenching but the most chiral coarse result is still some way from experiment. The fine lattice result for this ratio may indicate that discretisation errors are present for this quantity which shift the ratio further from the experimental value. However, again this needs further investigation. The experimental result for the ψ system ($c\bar{c}$) has been included to show that a lot of the heavy quark mass dependence cancels in this ratio (c and b quarks are both considered to be heavy as their masses are greater than the typical scale of QCD).

A lattice determination of the next order current corrections has shown that, unless they have a very large matching factor, they only shift these values by a few percent [74] and not enough to agree with experiment.

However, it is thought that it may well be the case that the matching factors for these current corrections are big, and details of a preliminary calculation to perturbatively calculate the lowest and higher order Z_{match} factors (as has been done for the decay constant of the B meson f_B [75]) is given in chapter 6. Once completed, this calculation will provide the matching coefficients needed to determine leptonic widths without taking ratios.

Absolute Values

The preliminary matching calculation in chapter 6 uses only a lowest order NRQCD action, but it is expected that the matching coefficient for the leading order NRQCD current will not change greatly as the action is improved. Therefore it is possible to use the results of this to determine approximate absolute values of the leptonic widths correct to leading order in v^2. Instead, however, this is done using the results from [76] where a tadpole improved

	$\Gamma_{ee}(1S)$(keV)	$\Gamma_{ee}(2S)$(keV)
Lattice	1.056(54)	0.612(40)
Experiment	1.32(5)	0.520(32)

Table 4.2: Absolute values for the Υ and Υ' leptonic widths. Lattice results are from the most chiral coarse unquenched MILC ensemble and experimental results are from [86].

(and therefore more similar) action has been used. The relevant factor is

$$Z_{match}(aM_b^0 = 2.8) = 0.9359 \tag{4.6}$$

and, using Eqn. 3.21, the results for the absolute values for the ground and 1st excited leptonic widths using the $\psi(0)$ from the most chiral coarse unquenched ensemble are given in table 4.2 along with the experimental values. It can be seen that the ground lattice result is lower than experiment while the excited lattice result is above experiment.

4.7 NRQCD Stability Parameter

The NRQCD stability parameter n, introduced in section 2.5.1, prevents the heavy quark evolution equation becoming unstable, and must be set such that $aM_b^0 > 3/n$. The value $2n = 4$ was chosen for the majority of runs but one run on the $n_f = 2 + 1$ $m_{light} = 0.01$ coarse ensemble was done with $2n = 8$ to check that the results are independent of n.

It can be seen that the $2n = 8$ results from the previous chapter for the lattice spacing, effective mass and S wave fine structure completely agree with the equivalent results from $2n = 4$ run. It is concluded that the results are indeed n independent.

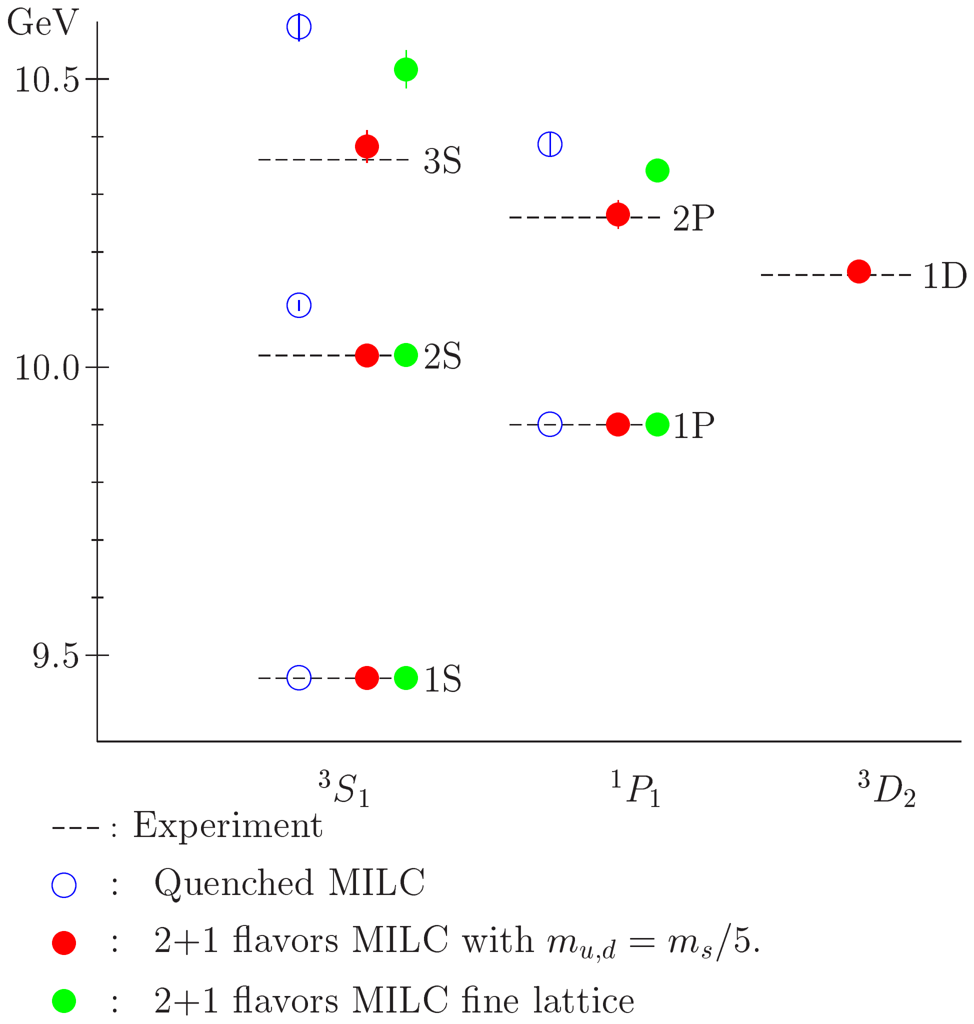

Figure 4.6: The Υ spin independent spectrum. Blue open circles, red closed circles and green closed circles are quenched, coarse $n_f = 2 + 1$ $m_{light} = 0.01$, and fine lattice results respectively. Dashed lines are experimental values.

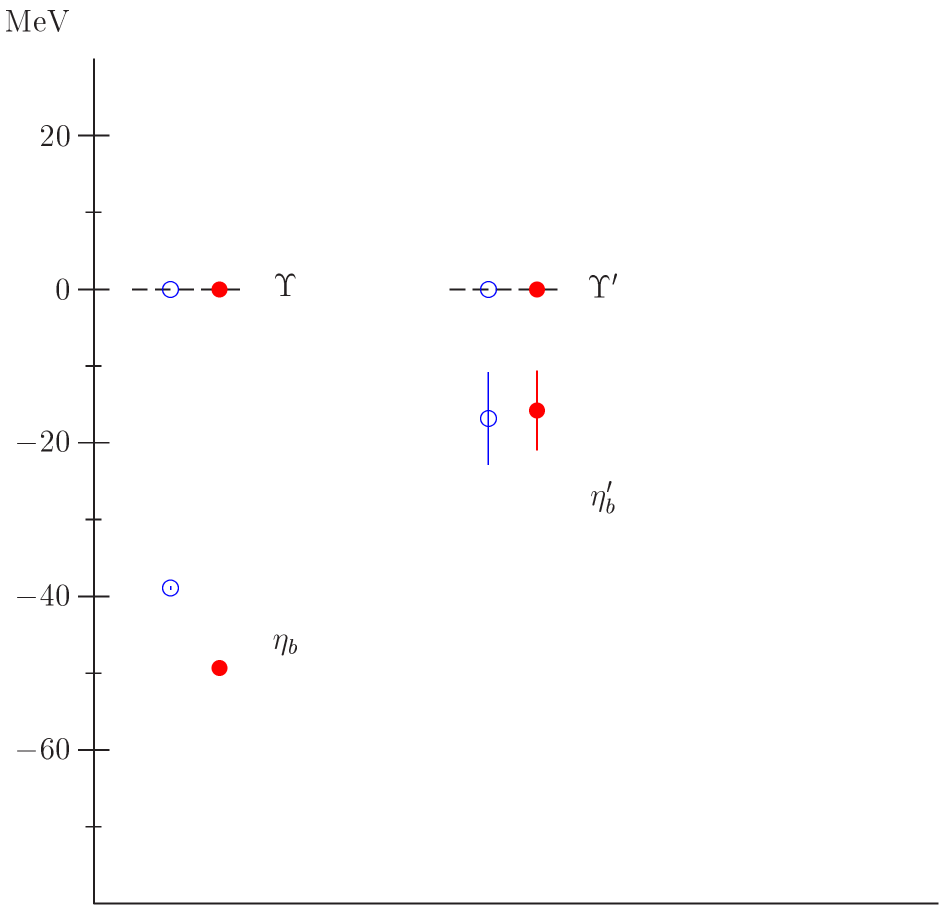

– – – : Experiment

○ : Quenched

● : 2+1 flavours MILC with $m_{u,d} = m_s/5$.

Figure 4.7: The Υ hyperfine splitting. Blue open circles and red closed circles are quenched and coarse $n_f = 2{+}1$ $m_{light} = 0.01$ lattice results respectively. Dashed lines are experimental values.

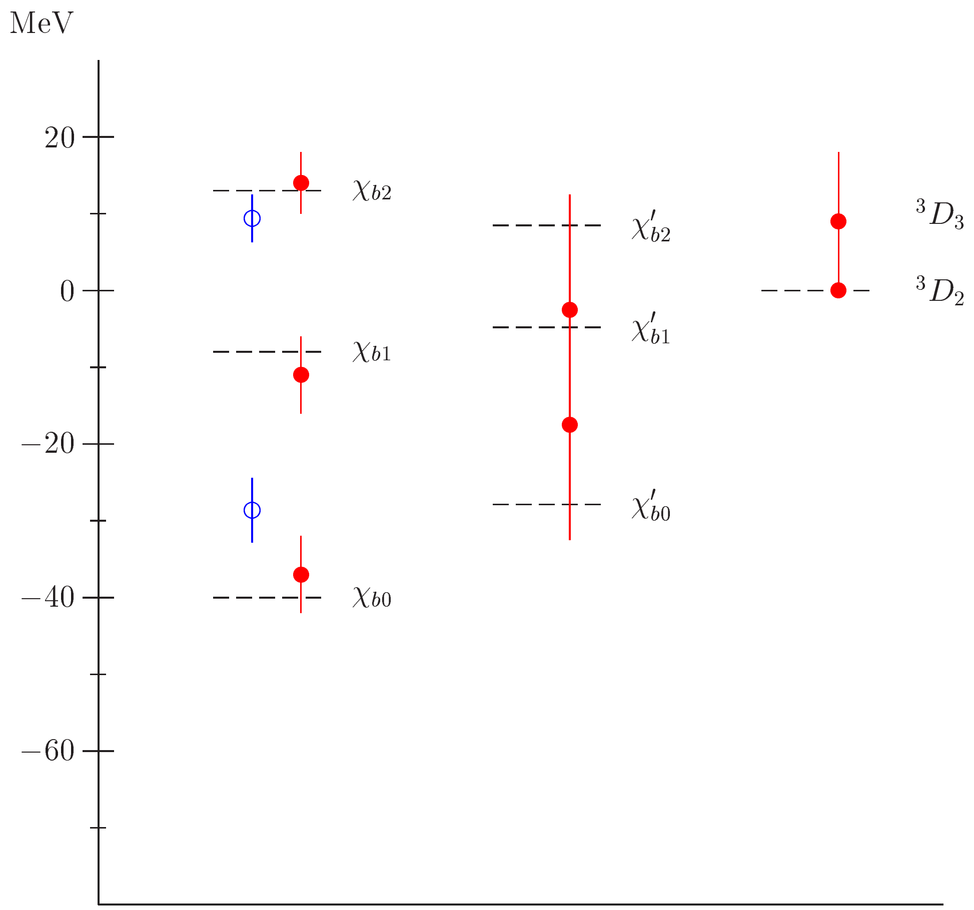

– – – : Experiment

○ : Quenched

● : 2+1 flavours MILC with $m_{u,d} = m_s/5$.

Figure 4.8: The Υ P and D wave spin dependent spectrum. Blue open circles and red closed circles are quenched and coarse $n_f = 2+1$ $m_{light} = 0.01$ lattice results respectively. Dashed lines are experimental values.

Chapter 5

The Strong Coupling Constant

5.1 Introduction

The results from Υ spectroscopy can be used to obtain some of the worlds most accurate and reliable determinations of the strong coupling constant α_s [77].

Obtaining determinations of α_s is important in the search for physics beyond the standard model. At high momenta α_s has the form

$$\alpha_s = \frac{c}{\ln(q/\Lambda)}, \tag{5.1}$$

where Λ is a mass scale which must be determined by comparison to experiment, and c is a constant. This logarithmic decay is equivalent to the term *asymptotic freedom*. Thus α_s very scale dependent and at high energies new physics such as supersymmetry could have an effect on α_S. Disagreements between α_S values determined at different scales and evolved to a common scale would expose such new physics. It is argued by some that the current world average value for α_S allows unification of all the gauge couplings at some high scale only if the superpartners are included in the evolution of the gauge couplings [78].

The first step in a lattice determination of α_s involves tuning the lattice simulation to accurately reproduce an experimental result. The Υ radial and orbital splittings are ideal quantities to tune due to the accuracy of the simulations and the experimental results.

Once the system is tuned, the second step involves calculating short distance quantities on the lattice. Being short distance, these quantities can also be calculated as a perturbative

run	$3 \times plaq$	$\alpha_V(3.33a)$	PS set α_V(8.2GeV)	SS set α_V(8.2GeV)
MILC Quenched	1.863941	0.1868997618	0.1674(17)	0.1603(4)
MILC $n_f = 2$	1.763853	0.2069089509	0.1829(17)	0.1792(19)
MILC $m_l = 0.01$	1.700912	0.2181015112	0.1888(10)	0.1890(7)
MILC $m_l = 0.02$	1.709187	0.2160638041	0.1893(8)	0.1883(7)
MILC $m_l = 0.05$	1.724505	0.2123169106	0.1877(13)	0.1847(7)
MILC Fine	1.784411	0.1979785248	0.1930(8)	0.1923(7)

Table 5.1: Values of the non-perturbatively determined plaquette, and the coupling α_V at the Lepage and MacKenzie scale $3.33a$ and evolved to 8.2GeV using both the Υ $1^1P_1 - 1^3S_1$ and $2^3S_1 - 1^3S_1$ splittings to fix a.

series in α_S and a comparison of the non-perturbative and perturbative results will yield a value for α_s.

The following results are an updated version of those given in [79].

5.2 Determination of α_s

Instead of using a bare coupling constant, a renormalised coupling constant should be used for better behaved perturbation series (see section 2.7 and [21]).

Here the physically well motivated coupling $\alpha_V(q)$ is used. $\alpha_V(q)$ is defined such that the static quark potential $V(q)$ has the exact form

$$V(q) = -\frac{16\pi}{3q^2}\alpha_V(q). \tag{5.2}$$

The perturbative expansions to third order in α_s of $R \times T$ Wilson loops $W(R,T)$ particular to the MILC action have recently been calculated by Trottier and Mason [80] resulting in the relation

$$-\ln W(R,T) = w_0\alpha_V(q^*) \times [1 + r_1\alpha_V(q^*) + r_2\alpha_V^2] + \mathcal{O}(\alpha_V^4) \tag{5.3}$$

where q^* is the Lepage and Mackenzie scale [21] - the most appropriate scale for expansions in the coupling constant. The perturbative coefficients r_i have been split into gluonic and

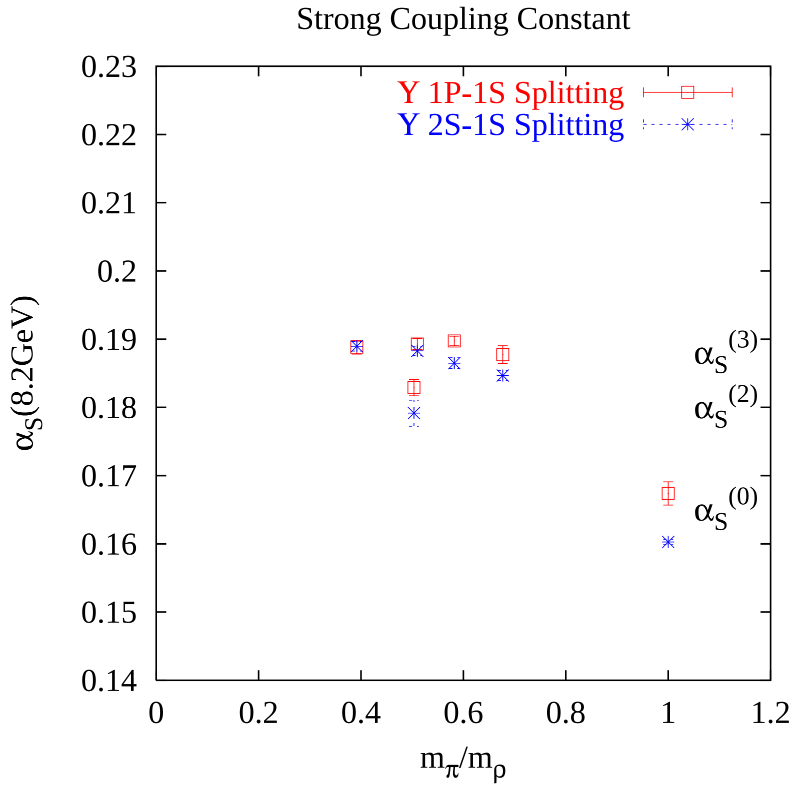

Figure 5.1: The coupling α_s at the scale 8.2GeV for various numbers of dynamical quarks. Open circles represent results using scales determined using the 1P-1S Υ splittings and fancy diamonds represent results scales determined using the 2S-1S Υ splittings.

fermionic components as follows:

$$r_i = r_{i,g} + r_{i,f}^{(1)} N_f + r_{i,f}^{(2)} N_f^2. \tag{5.4}$$

Table 5.2 lists, for the plaquette, the values of the non-zero components of the coefficients and the Lepage and MacKenzie scale in lattice units aq^*.

The non-perturbatively calculated values [81] for the plaquette (multiplied by 3) are given in table 5.1. Solving Eqn. 5.3 then allows determinations of α_V provided a^{-1} and hence q^* has been determined.

aq^*	w_0	$r_{1,g}$	$r_{1,f}$	$r_{2,g}$	$r_{2,f}^{(1)}$	$r_{2,f}^{(2)}$
3.33	3.068395(1)	-0.7753(2)	-0.096934(12)	-0.722(39)	0.7737(51)	0.010217(4)

Table 5.2: The Lepage and Mackenzie scale and the coefficients appearing in the 2 loop perturbative expansion of α_V for the plaquette.

5.3 Quenched Scaling of α_s

If our lattice theory is to be reliable, α_s determined at different scales and evolved to the same scale should agree. Such scaling is tested for the quenched theory in this section.

No quenched fine MILC ensembles were used for the analysis in this thesis. Therefore, scales obtained from r_0 were used to determine the scaling behaviour of α_s in the quenched approximation. r_0 is a very precisely determined scale (even although it is not well known physically) so enables good comparison of α_s determinations at different a values.

Figure 5.2 shows determinations of α_S evolved to the scale $15/r_0$ plotted against $(a/r_0)^2$ where a is the scale at which α_s was determined. Shown are determinations using first, second and third order perturbation theory for the use of both Wilson plaquette glue and MILC improved glue. It can be seen that at each order the MILC results are very flat indicating excellent scaling. Additionally, as the perturbative order is increased, the MILC and Wilson results converge and are in agreement at third order. This indicates that we do not need to worry about scaling effects in the dynamical case. However, this possibly is not the case as will be seen in section 5.5

5.4 Results from Υ Spectroscopy

The a^{-1} values from the Υ spectroscopy (table 3.10) were used to determine q^*. To be compared with one another, these determinations must be evolved to an arbitrary common physical scale, chosen here for historical reasons to be 8.2GeV. The results using a^{-1} from both the PS and SS Υ splittings were evolved to this scale and are shown also in table 5.1.

The results are plotted for $\alpha_V^{(n_f)}$ in Figure 5.1. The ordinate gives the strong coupling constant in the V scheme at 8.2GeV and the abscissa gives against the ratio of the pseu-

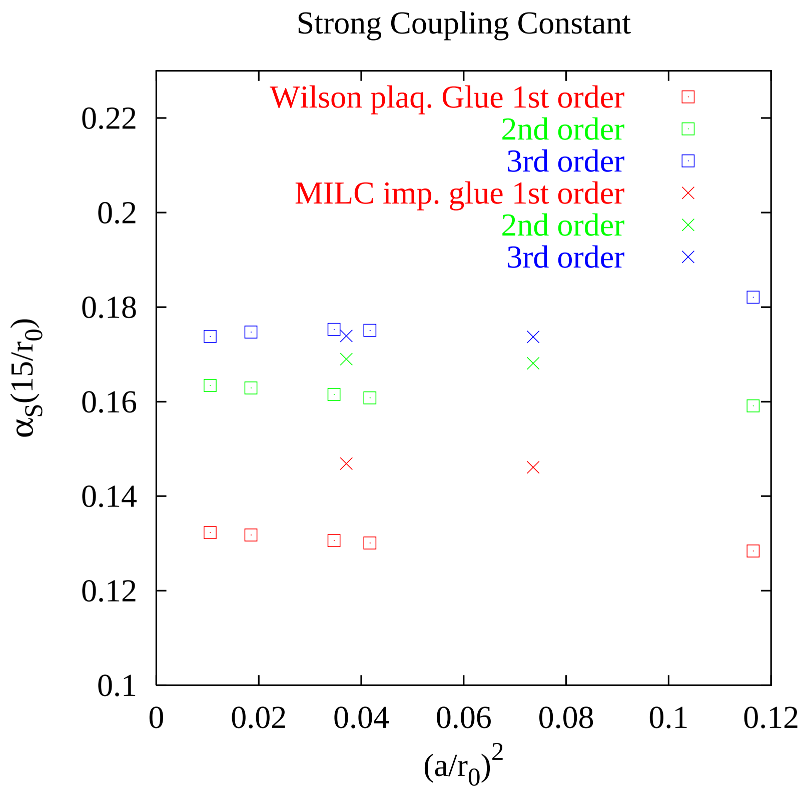

Figure 5.2: Determinations of the strong coupling constant using scales from the static quark potential. Crosses and open squares represent MILC improved glue and Wilson plaquette glue results respectively. For each, red, green and blue colours represent the use of first, second, and third order perturbation theory respectively.

doscalar to vector light-light meson mass where the valence quark mass is equal to the u/d sea quark mass. The point to be taken from these results is the presence of a clear difference in α_s with the number of dynamical flavours used in the simulation.

5.5 Dynamical Scaling of α_s

Figure 5.3 shows determinations of α_S on both the coarse and fine MILC lattices evolved to a common scale of 8.2GeV. The Υ PS splitting was used to determine the scale. The shift seen could be a sign of discretisation errors. However, it is more likely that the cause is perturbative problems; large coefficients of α_s^4 when $n_f \neq 0$ may cause the next order of the expansion to have a larger than expected effect. Much work is currently being done on

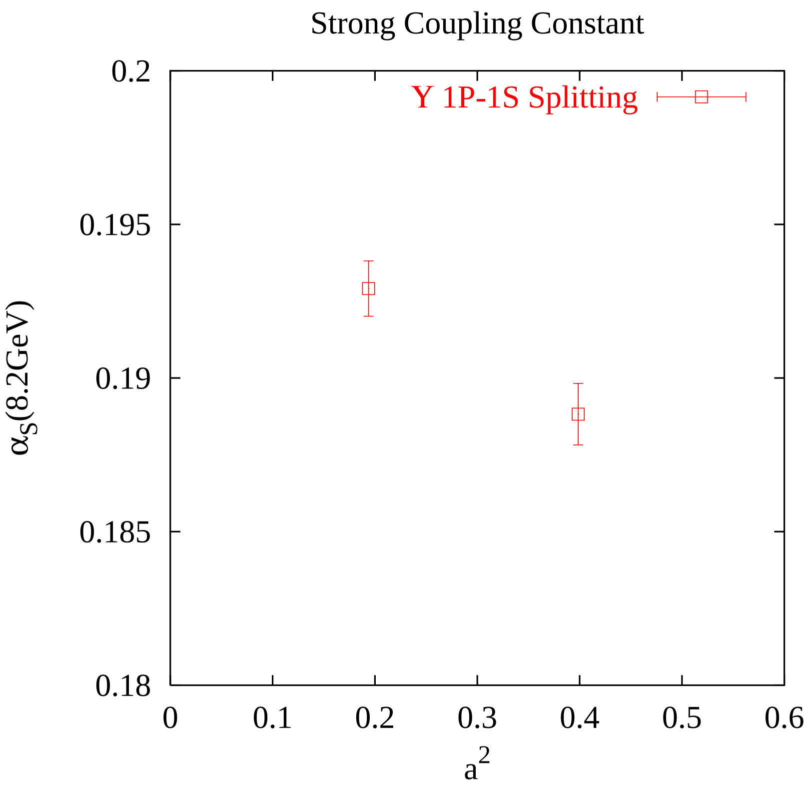

Figure 5.3: Results for the strong coupling constant determined at different scales and evolved to 8.2GeV. The Υ $1^1P_1 - 1^3S_1$ splitting was used to fix the scale

.

this expansion [1].

5.6 Comparison with World Average

The lattice results from the most chiral ensemble and fine ensemble were converted into the more commonly quoted $\overline{MS}$ renormalisation scheme using the relation

$$\alpha^{(N_f)}_{\overline{MS}}(e^{5/6}q) = \alpha^{(N_f)}_{V}(q) \times \left[1 + 2\alpha_V/\pi + (0.1411N_f - 0.7344)\alpha_V^2\right]. \tag{5.5}$$

They were then evolved to the mass of the Z particle and extrapolated to 5 dynamical flavours to give $\alpha^{(5)}_{\overline{MS}}(M_Z)$. These results along with the current world average value are given

[1]There is also currently work being done to sort out some disagreement in this perturbative calculation with earlier literature

	$\alpha^{(5)}_{\overline{MS}}(M_Z)$
Coarse Lattice	0.1125(5)(7)
Fine Lattice	0.1143(3)(5)
World Average	0.117(2)

Table 5.3: Lattice determinations of the strong coupling constant converted to the $\overline{MS}$ scheme, evolved to the scale M_Z, and extrapolated to 5 dynamical flavours. Also given is the current world average value from [86].

in table 5.3. The errors in the first brackets are from the lattice spacings while the second errors are from the perturbation theory. It can be seen that the coarse lattice result is not in agreement with the world average if the quoted errors are accurate. Scaling violations could account for this but, as already explained, it is thought that there are perhaps problems with the perturbative expansion and the perturbative errors could be larger than those quoted. In principle, a result with errors as small as those given should be possible which would then be one of the world's most precise determinations.

Chapter 6

Perturbative Matching of NRQCD Currents to Continuum

6.1 Introduction

In order to compare matrix elements calculated in lattice NRQCD with experimental results quoted in some continuum renormalisation scheme, a calculation to match the schemes must be performed. In particular, we want to obtain experimentally comparable results for the leptonic width of the Υ.

Figure 6.1 shows a Feynman diagram for the leptonic decay of the Υ, where the gluons are present to show an example of the loop corrections which contribute to the process. The $b\bar{b}$ annihilation vertex must be perturbatively calculated in QCD and in NRQCD including all n-loop corrections when working to n^{th} order. This then allows the appropriate n-loop matching coefficients for the heavy-heavy vector annihilation currents to be obtained. This chapter describes how the 1-loop matching coefficients can be obtained and gives results in doing so for a simpler NRQCD action than that used for the simulations.

The work in this chapter has been done in collaboration with Ron Horgan and Georg Von Hippel from the University of Cambridge and Alistair Hart from the University of Edinburgh. The mathematical details of the QCD integrals and QCD-NRQCD subtraction procedure were largely worked out by Ron and Georg. These details will be discussed in this chapter

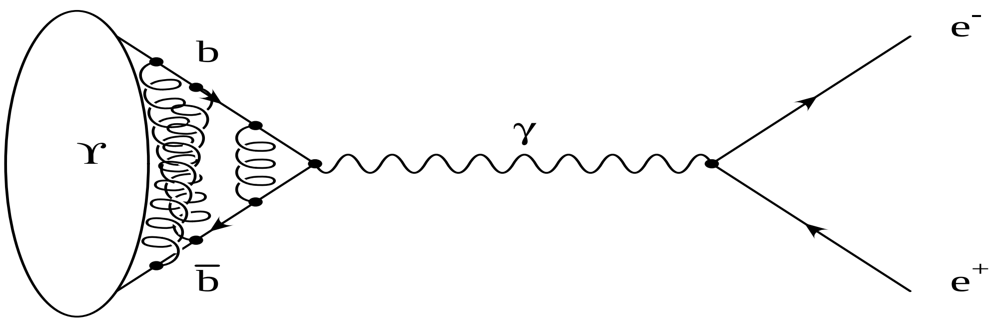

Figure 6.1: The leptonic decay of an Υ.

but are described in full in [85]. Alistair concentrated on automation of the Feynman rules (which has not been used in this preliminary calculation but will be needed for the full calculation), and I was responsible for the numerical and computational implementation of the calculation on the Sunfire machine at the High Performance Computing Facility at Cambridge.

6.2 Matching Procedure

A QCD matrix element can be decomposed into NRQCD current operators as follows:

$$\langle 0|J^{QCD}|\overline{q}q\rangle = \sum_i a_i \langle 0|J_i^{NRQCD}|\overline{q}q\rangle. \tag{6.1}$$

The matching procedure involves determining the co-efficients a_i. This is done by requiring the perturbative calculations for the relevant process at the quark level agree in continuum QCD and lattice NRQCD to a given order in α_s. Here we work to 1-loop order ($\mathcal{O}(\alpha_s)$).

Tree Level Calculation

In order to match to 1-loop, we first must consider the matching result at tree level (zeroth order in α_s).

At tree-level, the co-efficients are given by a non-relativistic expansion of the continuum tree level matrix element $\bar{v}(-\mathbf{p})\gamma_\mu u(\mathbf{p})$. We use the standard Dirac representation

$$\gamma^0 = \begin{pmatrix} 1 & 0 \\ 0 & -1 \end{pmatrix} \qquad \gamma^i = \begin{pmatrix} 0 & \sigma^i \\ -\sigma^i & 0 \end{pmatrix} \tag{6.2}$$

where σ^i are Pauli spin matrices [37], and

$$u(\mathbf{p}) = \begin{pmatrix} \psi \\ \frac{\sigma\cdot\mathbf{p}}{E+m}\psi \end{pmatrix} \sqrt{\frac{E+m}{2m}} \qquad v(\mathbf{p}) = \begin{pmatrix} \frac{\sigma\cdot\mathbf{p}}{E+m}\chi \\ \chi \end{pmatrix} \sqrt{\frac{E+m}{2m}} \tag{6.3}$$

where ψ and χ are the standard Pauli spinors for quarks and antiquarks respectively as introduced in section 2.4. When expressed in terms of the Pauli spinors, the relevant ($^3S_1$ part) Dirac tensor components of the tree level matrix element become

$$\overline{v}(-\mathbf{p})\gamma^0 u(\mathbf{p}) = 0 \tag{6.4}$$

and

$$\overline{v}(-\mathbf{p})\gamma^i u(\mathbf{p}) = f_1(v^2)\chi^\dagger\sigma^i\psi, \tag{6.5}$$

where f_1 is an expansion in v^2 where $v = |\mathbf{p}|/m$ [1].

Tree-level matching simply involves performing the expansion to determine $f_1(v^2)$ which will yield values for $a_i^{(0)}$.

As will be seen shortly, it is useful to note that, again in terms of the relevant Dirac tensor components ,

$$\overline{v}(-\mathbf{p})\frac{i\sigma^{i0}E}{m}u(\mathbf{p}) = f_2(v^2)\chi^\dagger\sigma^i\psi \tag{6.6}$$

with similarly f_2 involving an expansion in v^2, and where $\sigma^{\mu\nu}$ is given by

$$\sigma^{\mu\nu} = \frac{i}{2}[\gamma^\mu, \gamma^\nu]. \tag{6.7}$$

[1] Note that v relates to the particle velocity β by $v = \beta/\sqrt{1-\beta^2}$.

Calculation at 1-loop Order

The QCD 1-loop matrix element can be written in terms of the $\mathcal{O}(\alpha_s)$ contributions to the vertex structure functions $F_1^{(1)}$ and $F_2^{(1)}$ as [52]

$$\begin{aligned} & \langle 0|J^{QCD}|\overline{q}q\rangle_{1-loop}^{up\ to\ \&\ inc.} & (6.8)\\ = & \ (1+\alpha_s F_1^{(1)}(4E^2))\overline{v}(-\mathbf{p})\gamma_\mu u(\mathbf{p}) & (6.9)\\ & +i\alpha_s F_2^{(1)}(4E^2)\overline{v}(-\mathbf{p})\frac{i\sigma_{\mu\nu}p^\nu}{m}u(\mathbf{p}) & (6.10)\\ = & \ f_1(v^2)\chi^\dagger\sigma^i\psi & (6.11)\\ & +\alpha_s\left[F_1^{(1)}(4E^2)f_1(v^2)+F_2^{(1)}(4E^2)f_2(v^2)\right]\chi^\dagger\sigma^i\psi & (6.12)\end{aligned}$$

where we have used the results of the tree level matching.

$F_1^{(1)}$ is UV-finite (i.e. it only involves loop integrals which are finite as the cutoff on the internal momenta tends to infinity) but contains IR divergences (integrals which are infinite as the cut-off on internal momenta tends to zero). NRQCD is a low energy effective theory of QCD so it has the same low-energy behaviour, and thus contains the same IR divergences. Therefore, if the theories are properly matched to one-loop then the subtraction of the one-loop matrix elements of the correct sum of the NRQCD operators from the one-loop matrix element of the QCD operator should vanish, or in other words we can determine a_i to one loop by imposing

$$\begin{aligned} & \langle 0|J^{QCD}|\overline{q}q\rangle_{1-loop}^{up\ to\ \&\ inc.} - \sum_i a_i\langle 0|J_i^{NRQCD}|\overline{q}q\rangle_{1-loop}^{up\ to\ \&\ inc.} & \\ = & \ f_1(v^2)+\alpha_s\left[F_1^{(1)}(4E^2)f_1(v^2)+F_2^{(1)}(4E^2)f_2(v^2)\right] & \\ - & \ \sum_i(a_i^{(0)}+\alpha_s a_i^{(1)})\left(\langle 0|J_i^{NRQCD}|\overline{q}q\rangle^{(0)}+\alpha_s\langle 0|J_i^{NRQCD}|\overline{q}q\rangle^{(1)}\right) & (6.13)\\ = & \ 0. & (6.14)\end{aligned}$$

The tree level matching results in the cancellation of $a_i^{(0)}\langle 0|J_i^{NRQCD}|\overline{q}q\rangle^{(0)}$ with the Taylor co-efficients of $f_1(v^2)$ leaving

$$
\begin{aligned}
& \left[F_1^{(1)}(4E^2)f_1(v^2) + F_2^{(1)}(4E^2)f_2(v^2)\right] \\
- & \sum_i a_i^{(0)}\langle 0|J_i^{NRQCD}|\overline{q}q\rangle^{(1)} \\
- & \sum_i a_i^{(1)}\langle 0|J_i^{NRQCD}|\overline{q}q\rangle^{(0)} = 0
\end{aligned}
\tag{6.15}
$$

The $a_i^{(1)}$ values can be obtained from this resulting expression which is both UV and IR finite.

The first two terms on the left hand side of the above equation each have contributions from terms which are an odd power of v. These arise due to the *Coulomb singularity*; integrals with $1/v$ (i.e. singular at $v = 0$) behaviour. These are a facet of the quark poles arising in the 1-loop corrections to the annihilation vertex of figure 6.1. The terms with odd powers of v arise from multiplying these Coulomb integrals with powers of v^2.

However, since $\langle 0|J_i^{NRQCD}|\overline{q}q\rangle^{(0)}$ contains no odd powers of v, all odd powers of v which arise from the Coulomb singularity in QCD and NRQCD must cancel in the subtraction of the second from the first term.

It is important to ensure that the subtleties involved with performing the calculation (i.e. choice of integration contours) are dealt with carefully to ensure that this cancellation does indeed take place, and we are left with a result incorporating only even powers of v.

The integrations are evaluated numerically using VEGAS [82]. In doing so the co-efficients c_i can be determined where

$$
\begin{aligned}
& \left[F_1^{(1)}(4E^2)f_1(v^2) + F_2^{(1)}(4E^2)f_2(v^2)\right] \\
- & \sum_i a_i^{(0)}\langle 0|J_i^{NRQCD}|\overline{q}q\rangle^{(1)} = \sum_i c_i v^{2i}.
\end{aligned}
\tag{6.16}
$$

Since $\langle 0|J_i^{NRQCD}|\overline{q}q\rangle^{(0)} = j_i v^{2i}$ we are left with

$$
a_i^{(1)} = \frac{c_i}{j_i},
\tag{6.17}
$$

and the matching process is completed.

The 1-loop QCD form factors $F_1^{(1)}$ and $F_2^{(1)}$ can be determined by calculating the 1-loop corrections to the vertex diagram, which are shown in figure 6.2 [85].

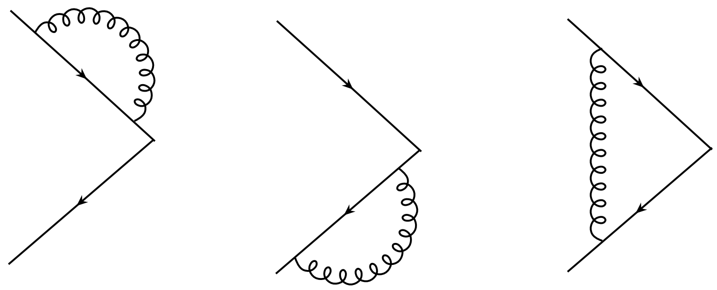

Figure 6.2: The diagrams contributing to the 1-loop correction to the QCD annihilation vertex function.

Figure 6.3 shows the one-loop diagrams contributing to the quark-antiquark annihilation amplitude in NRQCD which appear at lowest order in v.

Additional NRQCD one loop corrections appearing at $\mathcal{O}(v^2)$, earlobe contributions Δ_{ear} and tadpole contributions Δ_{tad}, are shown in figure 6.4.

These NRQCD diagrams must be calculated using the same action as was used in the simulations, i.e. $\mathcal{O}(v^4)$ tadpole improved, for a full matching calculation and this will be done in time, but here we present results for a simpler preliminary calculation which we have performed to ensure that our methods are working and reliable.

6.3 Results for Lowest order NRQCD

We use the $\mathcal{O}(v^2)$ NRQCD action [53, 83]

$$S = a^3 \sum_{\mathbf{x},t} \psi^\dagger_{\mathbf{x}t} \left(\Delta_4 - \sum_i \frac{\Delta_i \Delta_{-i}}{2ma} \right) \psi_{\mathbf{x}t}. \tag{6.18}$$

This is not a good action to use for obtaining physical results since it lacks tadpole improvement but it is suitable for tests of the numerical methods since its Feynman rules are simple enough to be written out by hand and are listed in [53].

This preliminary calculation has not included the Δ_{ear} and Δ_{tad} terms. The subtraction of Eqn. 6.16 was coded by hand (i.e. with no automation of Feynman rules) using these Feynman rules and integrated using a parallelised version of VEGAS for several values of v. The results are given in table 6.1.

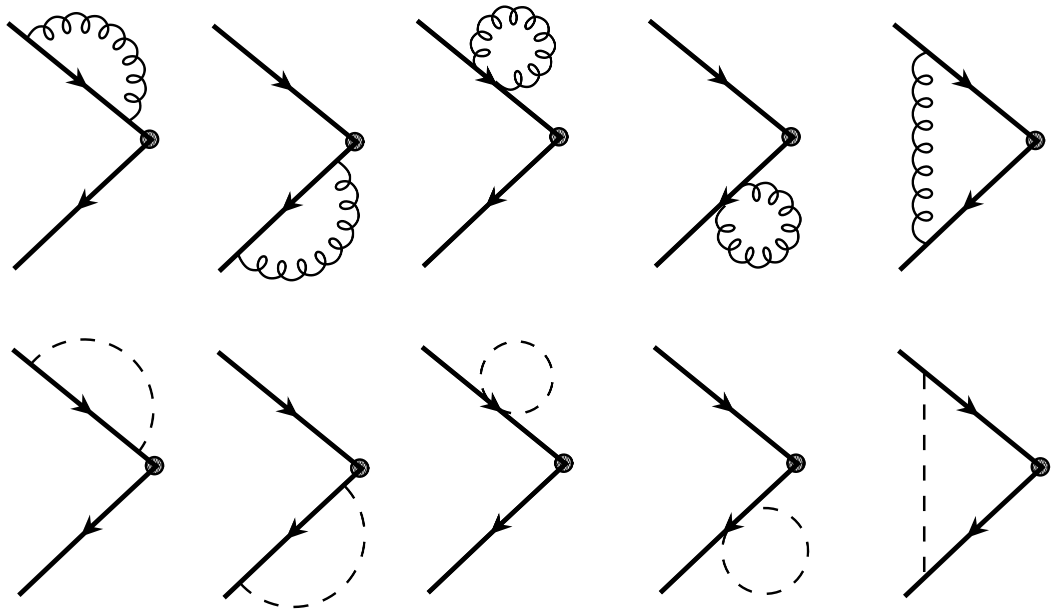

Figure 6.3: The diagrams contributing to the 1-loop correction to the NRQCD annihilation vertex function at lowest order in v^2. Solid and dashed lines depict spatial and temporal gluons respectively.

Figure 6.5 plots the results for the QCD-NRQCD subtraction against v^2. This plot clearly shows that all the $\mathcal{O}(v)$ terms have cancelled between QCD and NRQCD as required, indicating that the subtraction procedure is working well.

6.4 Conclusions

The results of the previous section demonstrate that these numerical techniques are working and all that is required for the full calculation is for higher order lattice NRQCD to be coded. The Feynman rules for this are extremely complex and in order to minimise errors, and enable easy repetition of the calculation with a different action, the Feynman rules should be created automatically.

The PYTHON language is suitable for such automation [84] and much work has been done in developing such code. The full calculation should use PYTHON to automatically

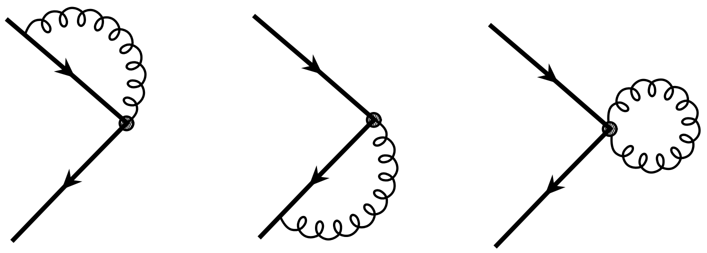

Figure 6.4: The diagrams contributing to the 1-loop correction to the NRQCD annihilation vertex function appearing at $\mathcal{O}(v^2)$; Δ_{ear} (leftmost two diagrams) and Δ_{tad} (rightmost diagram).

v	Subtraction Result
0.05	-0.09244(46)
0.1	-0.09488(18)
0.15	-0.09886(16)
0.2	-0.10541(12)
0.25	-0.11519(10)

Table 6.1: The numerical result for the subtraction of the NRQCD part from the QCD part of the 1-loop vertex diagram integration.

generate the Feynman rules directly from the action. The results of this can be read into the numerical integration VEGAS code which incorporates a hardwired QCD integrand.

Then the equivalent QCD-NRQCD subtraction results will not include any odd powers of v. The results can be fitted to $\sum_i c_i v^{2i}$ to determine c_i (c.f Eqn. 6.16) and the matching coefficients a_i can be determined through Eqn. 6.17. Then the lattice NRQCD simulation results for the annihilation matrix elements, and hence the leptonic width, can be quoted in continuum QCD and compared with experiment as required.

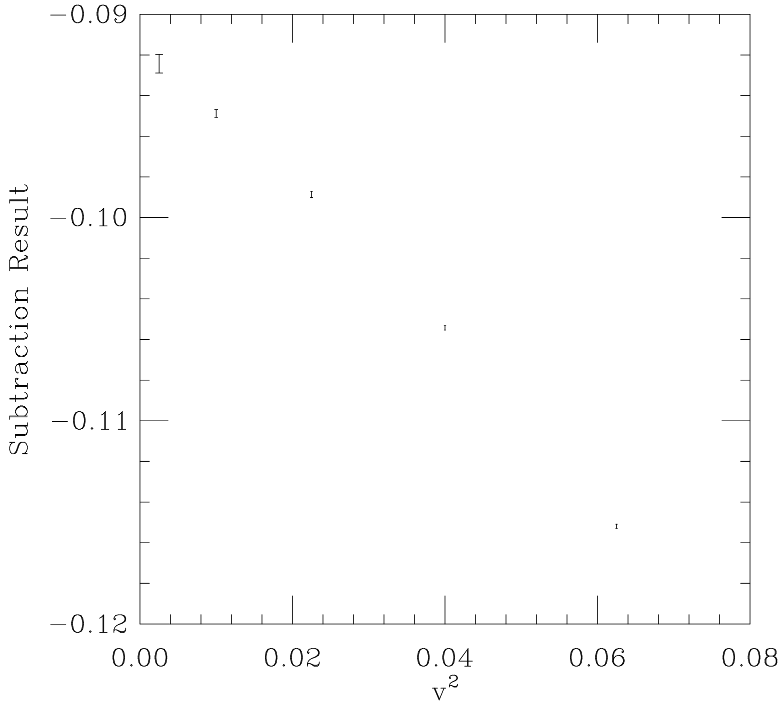

Figure 6.5: The numerical result for the subtraction of the NRQCD part from the QCD part of the 1-loop vertex diagram integration plotted against v^2.

Chapter 7

Conclusions

Calculation of the Υ spectrum gives an excellent test for studying the dynamical content of the configurations being used. NRQCD can be used to give precise results which indicate how the light dynamical quarks feed in to the heavy meson properties. In this thesis I have used configurations generated by MILC which use the improved staggered formulation and incorporate 2+1 flavours of dynamical quarks with the u, d quark masses as low as around $m_s/5$; much lighter than in any previous calculation. I mostly used the relatively coarse lattices with $a \sim 0.13$fm but I used one fine ensemble, with $a \sim 0.08$fm, in order to check for scaling errors.

I have performed simulations of the creation, propagation and destruction of Υ mesons on these configurations using an $\mathcal{O}(v^4, a^2)$ NRQCD heavy quark action. The resulting meson correlators were fitted to using a new Bayesian fitting technique which, contrary to previous fitting methods, allows the whole range of data to be included in the fit yielding better determinations of the ground and first two excited energy levels and amplitudes.

For each ensemble, lattice spacings were determined by comparing the lattice results for both the $(h_b - \Upsilon)$ and $(\Upsilon' - \Upsilon)$ splittings with experiment. Quenching effects which cause these different determinations to disagree were seen to be absent for the most chiral unquenched ensemble, indicating that this ensemble has realistic dynamical quark content. Lattice spacings were also determined using the static quark potential and were seen to agree with the most chiral Υ results provided that r_0 is set to 0.466fm. The fine lattice spacing results were in agreement with the coarse results.

The Υ kinetic mass was determined for each run in order to tune the bare heavy quark mass. This was done by way of determining the difference between ground state energies of small non zero momentum Υ correlators with zero energy correlators.

Results for the radial and orbital splittings were given. Independence of dynamical light quark mass for these splittings indicated that chiral extrapolations were not necessary. The quenched results were seen to disagree with experiment while the results for the most chiral unquenched coarse ensemble were in complete agreement with experiment, suggesting that quenching problems have been resolved in calculating such splittings. Discrepancies exist with the higher energy level splittings in the case of the fine lattice results. Further work with higher statistics will attempt to resolve this issue.

I presented other improved staggered results from my collaborators. These results, when combined with the Υ spin independent results, show that our methods can be effectively used to gain realistic results at least for simple 'gold plated' meson quantities. These methods can now be used with confidence to enable the extraction of the highly important CKM parameters.

The fine structure splittings depend on relativistic correction terms in the action and thus the results for these splittings are only accurate to 10% for the Υ. However, taking ratios of these splittings removes a large portion of the uncertainty. Bootstrap fits were done to take advantage of correlation between the states with different spin quantum numbers and enabling resolution of these energy splittings. The experimental results for the ground and first excited Υ hyperfine splittings are not known since the η_b and η_b' are unobserved, but the ratio of the first excited to ground hyperfine splittings is expected to be largely mass independent and indeed the simulation results for this ratio tends to the experimental result for the ψ with unquenching. The equivalent fine lattice result is in disagreement with the coarse result, and this could indicate scaling violations but requires further investigation. I have also given results for the absolute values (only accurate to 10%) of the hyperfine splittings and the P and D wave fine structure.

The lattice spacing values obtained from the Υ spectroscopy were used to determine values of the strong coupling constant α_s. This was done by comparing a third order perturbative expansion for the plaquette to a non-perturbatively determined value. Clear dependence on the number of dynamical flavours in the simulation can be seen. Results for tests of scaling of α_s using scales determined from r_0 in the quenched case are very promising as no scaling violations are observed, and the results with improved and unimproved actions agree. Dynamical scaling tests using Υ scales, however, showed a disagreement between the determinations at different scales. This could be due to a problem with the perturbative expansion for $n_f \neq 0$ and work is currently being undertaken to investigate this issue.

The amplitudes obtained from the fitting were used to give results for the wavefunction at the origin. These were used to give results, correct to leading order in v^2, for the ratio of the 1st excited to ground leptonic width of the Υ. In such a ratio the multiplicative matching factors between the lattice NRQCD and the continuum renormalisation schemes cancel allowing comparison with experiment. A tendency to experiment is observed but the value for the most chiral ensemble is still some way from experiment. Scaling violations are a likely cause and this requires further investigation.

Details of the procedure to match the lattice NRQCD currents to the continuum were given along with results from a preliminary calculation which uses a more simplistic action than that used for the simulation. These results show that the numerical methods of the perturbative calculation seem to be working and reliable.

In addition to the completion of the full matching calculation, additional work in this area should involve using a $\mathcal{O}(v^6)$ NRQCD lattice action to obtain fine structure results correct to 1%, and the performance of more runs using fine ensembles to attempt to understand and resolve the issues about scaling errors.

Appendix A

Experimental Particle Data

Meson	Rest Mass (GeV)
1^3S_1 $[\Upsilon(1S), \Upsilon]$	9.460
2^3S_1 $[\Upsilon(2S), \Upsilon']$	10.023
3^3S_1 $[\Upsilon(3S), \Upsilon'']$	10.355
1^1S_0 $[\eta_b(1S), \eta_b]$	Unobserved
2^1S_0 $[\eta_b(2S), \eta_b']$	Unobserved
1^1P_1 $[h_b(1S), h_b]$	Unobserved
1^3P_0 $[\chi_b0(1S)]$	9.860
2^3P_0 $[\chi_b0(2S)]$	10.232
1^3P_1 $[\chi_b1(1S)]$	9.892
2^3P_1 $[\chi_b1(2S)]$	10.255
1^3P_2 $[\chi_b2(1S)]$	9.913
2^3P_2 $[\chi_b2(2S)]$	10.269
1^3D_2	10.162

Table A.1: Experimental rest masses for bottomonia states lying under the threshold for decay to $B\bar{B}$. Data taken from the particle data group [86] except for the recently observed $^3D_2$ state, for which the data is from [42]. Masses for all other (observed) particles discussed in this thesis can be found in [86].

Appendix B

Correlator Fit Results

B.1 MILC Quenched $M_b^0 = 2.3$

2×2 **Matrix Fits**

n_{exp}	aE_0	aE_1	Q
2	0.2649(0.00032)	0.649(0.0029)	nan
3	0.26472(0.00033)	0.6515(0.004)	1.5e-07
4	0.26424(0.00034)	0.6277(0.0083)	0.27
5	0.26407(0.00037)	0.358(0.062)	0.12
6	0.26418(0.00037)	0.357(0.062)	0.17
7	0.2598(0.0064)	0.279(0.012)	0.024
8	0.259(0.0083)	0.277(0.01)	0.02

Table B.1: Matrix Bayesian fit to the $^3S_1$ channel.

n_{exp}	aE_0	aE_1	Q
2	0.23873(0.00025)	0.6359(0.0031)	nan
3	0.23871(0.00026)	0.6399(0.004)	1.2e-08
4	0.23846(0.00027)	0.6146(0.0083)	0.18
5	0.23843(0.00027)	0.399(0.089)	0.15
6	0.23842(0.00028)	0.346(0.07)	0.11
7	0.236(0.0029)	0.26(0.016)	0.024
8	0.2346(0.0052)	0.253(0.011)	0.012

Table B.2: Matrix Bayesian fit to the ${}^1S_0$ channel.

n_{exp}	aE_0	aE_1	Q
2	0.5259(0.0024)	0.8283(0.0051)	4.9e-08
3	0.5164(0.0031)	0.8312(0.0083)	0.0021
4	0.5083(0.0041)	0.784(0.015)	0.074
5	0.5087(0.0042)	0.782(0.017)	0.079
6	0.507(0.011)	0.658(0.081)	0.062
7	0.506(0.014)	0.629(0.079)	0.049
8	0.487(0.051)	0.559(0.054)	0.013

Table B.3: Matrix Bayesian fit to the ${}^1P_1$ channel.

2×1 **Ratio Fits**

t_{min}/t_{max}	ΔaE_0	Q
5/31	.0108909(.000027)	0.000
6/31	.0102286(.000030)	0.000
7/31	.0101624(.000037)	0.000
8/31	.0101517(.000039)	0.004
9/31	.0101213(.000042)	0.219
10/31	.0100993(.000046)	0.335
12/31	.0101256(.000042)	0.000
13/31	.0101048(.000045)	0.000
14/31	.0101029(.000069)	0.332
16/31	.0101137(.000067)	0.290
17/31	.0101169(.000063)	0.292
18/31	.0101117(.000060)	0.182
19/31	.0100931(.000073)	0.215
20/31	.0102409(.000171)	0.347
24/31	.0102257(.000093)	0.469
25/31	.0102310(.000101)	0.320

Table B.4: Standard vector fit to the ${}^3S_1$ kinetic mass with $(a\mathbf{p})^2 = 1$.

B.2 MILC Quenched $M_b^0 = 2.8$

2×2 Matrix Fits

n_{exp}	aE_0	aE_1	Q
4	0.26606(0.00025)	0.6198(0.0065)	0.85
5	0.26581(0.00032)	0.456(0.087)	0.87
6	0.26581(0.00032)	0.453(0.086)	0.88
7	0.2658(0.00032)	0.459(0.086)	0.9
8	0.26585(0.00037)	0.391(0.073)	0.85

Table B.5: Matrix Bayesian fit to the $^3S_1$ channel.

n_{exp}	aE_0	aE_1	Q
4	0.24457(0.0002)	0.6104(0.0067)	0.89
5	0.2444(0.00025)	0.438(0.089)	0.9
6	0.24439(0.00025)	0.438(0.089)	0.92
7	0.24439(0.00025)	0.44(0.089)	0.93
8	0.24438(0.00025)	0.442(0.089)	0.94

Table B.6: Matrix Bayesian fit to the $^1S_0$ channel.

n_{exp}	aE_0	aE_1	Q
4	0.51(0.0028)	0.779(0.011)	0.2
5	0.5083(0.0072)	0.654(0.079)	0.17
6	0.5086(0.0057)	0.681(0.094)	0.18
7	0.5094(0.0066)	0.656(0.077)	0.2
8	0.495(0.026)	0.567(0.048)	0.11

Table B.7: Matrix Bayesian fit to the $^1P_1$ channel.

3×3 **Matrix Fits**

n_{exp}	aE_0	aE_1	aE_2	Q
4	0.26711(0.00022)	0.6268(0.0019)	0.9217(0.0027)	0
5	0.26703(0.00023)	0.6048(0.0028)	0.9116(0.0036)	0
6	0.2666(0.00023)	0.6223(0.0027)	0.889(0.011)	2.4e-05
7	0.26613(0.00024)	0.574(0.02)	0.785(0.049)	0.011
8	0.26618(0.00024)	0.59(0.015)	0.807(0.08)	0.036
9	0.26599(0.00026)	0.525(0.076)	0.599(0.09)	0.0019
10	0.26593(0.00027)	0.526(0.079)	0.588(0.089)	0.0058

Table B.8: Matrix Bayesian fit to the $^3S_1$ channel.

n_{exp}	$a(loc,1)$	$a(loc,2)$	Q
4	0.26592(0.00029)	0.222354(0.00148667)	0
5	0.26604(0.00029)	0.203863(0.00230431)	0
6	0.26266(0.00043)	0.248651(0.00201978)	2.4e-05
7	0.26104(0.00058)	0.196755(0.0243635)	0.011
8	0.26139(0.00052)	0.208823(0.0217143)	0.036
9	0.26022(0.00076)	0.11501(0.12902)	0.0019
10	0.26008(0.0009)	0.120341(0.15605)	0.0058

Table B.9: Matrix Bayesian fit to the $^3S_1$ channel.

n_{exp}	aE_0	aE_1	aE_2	Q
4	0.24528(0.00018)	0.6157(0.0017)	0.9001(0.0027)	0
5	0.24524(0.00019)	0.6163(0.0017)	0.9096(0.0035)	5.2e-38
6	0.2449(0.00019)	0.6013(0.0043)	0.887(0.015)	3.9e-05
7	0.24471(0.00019)	0.5925(0.0051)	0.871(0.015)	0.019
8	0.24457(0.0002)	0.549(0.025)	0.644(0.044)	0.00039
9	0.24464(0.00021)	0.522(0.089)	0.62(0.1)	0.024
10	0.24461(0.00022)	0.388(0.077)	0.58(0.11)	0.04

Table B.10: Matrix Bayesian fit to the ${}^1S_0$ channel.

n_{exp}	$a(loc, 1)$	$a(loc, 2)$	Q
4	0.29038(0.00027)	0.235593(0.00149196)	0
5	0.28925(0.0003)	0.24131(0.00155226)	5.2e-38
6	0.28559(0.00046)	0.255326(0.00245909)	3.9e-05
7	0.28502(0.00047)	0.241558(0.00583943)	0.019
8	0.28392(0.0006)	0.173811(0.0509899)	0.00039
9	0.28466(0.0007)	0.117777(0.128052)	0.024
10	0.2845(0.00083)	0.0163347(0.0229154)	0.04

Table B.11: Matrix Bayesian fit to the ${}^1S_0$ channel.

2×1 **Ratio Fits**

t_{min}/t_{max}	ΔaE_0	Q
7/31	.0085308(.000038)	0.000
9/31	.0085822(.000028)	0.000
10/31	.0084909(.000033)	0.000
11/31	.0084275(.000041)	0.275
12/31	.0084014(.000044)	0.853
13/31	.0084181(.000049)	0.861
14/31	.0084230(.000053)	0.796
15/31	.0084618(.000061)	0.846
16/31	.0084502(.000061)	0.782
17/31	.0084697(.000070)	0.732
18/31	.0085186(.000141)	0.682
20/31	.0085455(.000132)	0.769
21/31	.0085401(.000072)	0.862
22/31	.0085520(.000107)	0.760
23/31	.0085121(.000069)	0.557
25/31	.0074285(.012563)	0.824
26/31	.0072341(.017363)	0.693

Table B.12: Standard vector fit to the ${}^3S_1$ kinetic mass with $(a\mathbf{p})^2 = 1$.

B.3 MILC $n_f = 2$

2×2 **Matrix Fits**

n_{exp}	aE_0	aE_1	Q
4	0.29545(0.00028)	0.633(0.011)	0.82
5	0.29518(0.00037)	0.47(0.08)	0.84
6	0.29519(0.00038)	0.469(0.081)	0.86
7	0.29521(0.00037)	0.468(0.081)	0.87
8	0.29523(0.00037)	0.464(0.081)	0.87

Table B.13: Matrix Bayesian fit to the $^3S_1$ channel.

n_{exp}	aE_0	aE_1	Q
4	0.26873(0.00022)	0.618(0.012)	0.93
5	0.26871(0.00022)	0.619(0.012)	0.94
6	0.26853(0.00028)	0.44(0.082)	0.95
7	0.26852(0.00031)	0.393(0.07)	0.94
8	0.26853(0.00029)	0.433(0.081)	0.96

Table B.14: Matrix Bayesian fit to the $^1S_0$ channel.

n_{exp}	aE_0	aE_1	Q
4	0.5525(0.0052)	0.783(0.023)	0.9
5	0.5528(0.0051)	0.791(0.026)	0.91
6	0.548(0.011)	0.702(0.094)	0.88
7	0.548(0.011)	0.7(0.092)	0.89
8	0.531(0.026)	0.648(0.065)	0.85

Table B.15: Matrix Bayesian fit to the $^1P_1$ channel.

3×3 **Matrix Fits**

n_{exp}	aE_0	aE_1	aE_2	Q
4	0.29675(0.00025)	0.6643(0.0022)	0.9543(0.0032)	0
5	0.29614(0.00024)	0.6596(0.0023)	0.9422(0.0063)	9.4e-14
6	0.29577(0.00026)	0.6465(0.006)	0.875(0.023)	0.017
7	0.29553(0.00027)	0.616(0.018)	0.828(0.048)	0.11
8	0.29563(0.00026)	0.614(0.035)	0.726(0.069)	0.27
9	0.29528(0.00038)	0.434(0.068)	0.639(0.096)	0.41
10	0.29525(0.00039)	0.431(0.069)	0.626(0.097)	0.35

Table B.16: Matrix Bayesian fit to the $^3S_1$ channel.

n_{exp}	$a(loc, 1)$	$a(loc, 2)$	Q
4	0.28983(0.00033)	0.230658(0.00179046)	0
5	0.2892(0.00033)	0.245611(0.00187726)	9.4e-14
6	0.2861(0.00056)	0.255127(0.00328728)	0.017
7	0.28506(0.00063)	0.222701(0.0226464)	0.11
8	0.28569(0.00054)	0.180249(0.0815791)	0.27
9	0.2835(0.0016)	0.0495703(0.0200583)	0.41
10	0.2834(0.0016)	0.0466723(0.0304253)	0.35

Table B.17: Matrix Bayesian fit to the $^3S_1$ channel.

n_{exp}	aE_0	aE_1	aE_2	Q
4	0.26968(0.0002)	0.6504(0.0019)	0.9294(0.0031)	0
5	0.26939(0.0002)	0.6508(0.0019)	0.9358(0.0037)	1e-15
6	0.26903(0.0002)	0.6318(0.0057)	0.883(0.02)	0.13
7	0.26887(0.00021)	0.61(0.015)	0.853(0.05)	0.41
8	0.26894(0.0002)	0.6239(0.0059)	0.864(0.022)	0.77
9	0.26874(0.00026)	0.424(0.075)	0.6(0.11)	0.71
10	0.26879(0.00022)	0.568(0.072)	0.649(0.086)	0.68

Table B.18: Matrix Bayesian fit to the $^1S_0$ channel.

n_{exp}	$a(loc, 1)$	$a(loc, 2)$	Q
4	0.31873(0.00031)	0.24407(0.00178129)	0
5	0.31708(0.00035)	0.249616(0.00181999)	1e-15
6	0.31446(0.00054)	0.263142(0.00332973)	0.13
7	0.31358(0.0006)	0.243878(0.0164381)	0.41
8	0.31428(0.00051)	0.247758(0.00651559)	0.77
9	0.3127(0.0012)	0.0377495(0.0393483)	0.71
10	0.3131(0.00083)	0.157835(0.134325)	0.68

Table B.19: Matrix Bayesian fit to the $^1S_0$ channel.

2×1 **Ratio Fits**

t_{min}/t_{max}	ΔaE_0	Q
5/31	.0062805(.001646)	0.000
6/31	.0077890(.000299)	0.000
7/31	.0081866(.000088)	0.000
8/31	.0083170(.000054)	0.002
9/31	.0083627(.000045)	0.088
10/31	.0083918(.000042)	0.349
11/31	.0083891(.000038)	0.604
12/31	.0083932(.000038)	0.649
13/31	.0083884(.000037)	0.607
14/31	.0084100(.000042)	0.649

Table B.20: Standard vector fit to the ${}^3S_1$ kinetic mass with $(a\mathbf{p})^2 = 1$.

B.4 MILC $m_l = 0.01$

2×2 **Standard Matrix Fit**

t_{min}/t_{max}	$\Delta a E_0$	Q
2/31	.3050934(.000270)	0.002
3/31	.3049709(.000274)	0.027
4/31	.3048378(.000278)	0.107
5/31	.3047675(.000282)	0.194
6/31	.3047516(.000286)	0.248
7/31	.3047380(.000294)	0.276
8/31	.3047147(.000300)	0.401
9/31	.3046411(.000311)	0.387
10/31	.3046127(.000322)	0.346
11/31	.3046578(.000325)	0.294
12/31	.3047203(.000335)	0.240
13/31	.3047787(.000330)	0.212
14/31	.3048129(.000331)	0.136
15/31	.3046429(.000679)	0.000
16/31	.3046429(.000701)	0.000
17/31	.3046429(.000729)	0.000
18/31	.3046429(.000762)	0.000
19/31	.3046429(.000803)	0.000
20/31	.3046429(.000840)	0.000
21/31	.3046429(.000895)	0.000
22/31	.3046429(.000953)	0.000
23/31	.3046429(.001026)	0.000
24/31	.3046429(.001106)	0.000
25/31	.3046429(.001207)	0.000
26/31	.3046429(.001375)	0.000
27/31	.3046429(.001528)	0.000

Table B.21: Standard matrix fit to the ${}^3S_1$ channel.

2×2 **Bayesian Matrix Fits**

n_{exp}	aE_0	aE_1	Q
2	0.30556(0.00026)	0.7008(0.003)	1.4e-31
3	0.30535(0.00027)	0.704(0.0038)	3.9e-10
4	0.30475(0.00028)	0.6552(0.009)	0.37
5	0.30471(0.00031)	0.484(0.083)	0.38
6	0.30473(0.00029)	0.483(0.089)	0.42
7	0.30472(0.00029)	0.484(0.09)	0.45
8	0.30443(0.00047)	0.425(0.074)	0.38

Table B.22: Matrix Bayesian fit to the ${}^3S_1$ channel.

n_{exp}	aE_0	aE_1	Q
2	0.27391(0.0002)	0.6945(0.0032)	1.3e-30
3	0.27382(0.0002)	0.6934(0.0038)	4.1e-09
4	0.27354(0.00021)	0.6452(0.009)	0.51
5	0.27349(0.00024)	0.459(0.09)	0.5
6	0.27352(0.00021)	0.457(0.094)	0.54
7	0.27352(0.00021)	0.46(0.097)	0.57
8	0.27344(0.00028)	0.422(0.091)	0.5

Table B.23: Matrix Bayesian fit to the ${}^1S_0$ channel.

n_{exp}	aE_0	aE_1	Q
2	0.5985(0.0021)	0.8798(0.0051)	0.00056
3	0.579(0.01)	0.751(0.065)	0.0025
4	0.5831(0.004)	0.815(0.014)	0.59
5	0.579(0.011)	0.714(0.083)	0.5
6	0.575(0.015)	0.688(0.068)	0.54
7	0.564(0.028)	0.658(0.063)	0.47

Table B.24: Matrix Bayesian fit to the ${}^1P_1$ channel.

n_{exp}	aE_0	aE_1	Q
4	0.5679(0.0056)	0.791(0.026)	0.89
5	0.201(0.073)	0.568(0.074)	0.94
6	0.204(0.073)	0.569(0.074)	0.95
7	0.205(0.072)	0.57(0.074)	0.96
8	0.205(0.072)	0.57(0.074)	0.96

Table B.25: Matrix Bayesian fit to the ${}^3P_0$ channel.

n_{exp}	aE_0	aE_1	Q
4	0.5851(0.0058)	0.813(0.022)	0.92
5	0.5864(0.0065)	0.815(0.028)	0.93
6	0.5866(0.0065)	0.816(0.027)	0.93
7	0.57(0.025)	0.697(0.069)	0.88
8	0.567(0.027)	0.691(0.065)	0.89

Table B.26: Matrix Bayesian fit to the ${}^3P_1$ channel.

n_{exp}	aE_0	aE_1	Q
4	0.6004(0.0062)	0.801(0.032)	0.43
5	0.3(0.11)	0.6(0.12)	0.51
6	0.573(0.044)	0.678(0.06)	0.4
7	0.6004(0.008)	0.818(0.035)	0.5
8	0.29(0.12)	0.59(0.12)	0.48

Table B.27: Matrix Bayesian fit to the ${}^3P_{2E}$ channel.

n_{exp}	aE_0	aE_1	Q
2	0.3056(0.00026)	0.7017(0.003)	1.7e-37
3	0.30536(0.00027)	0.7031(0.0037)	5.3e-10
4	0.30473(0.00028)	0.6526(0.0083)	0.47
5	0.30474(0.00028)	0.478(0.087)	0.48
6	0.3047(0.00029)	0.473(0.089)	0.55
7	0.3047(0.00029)	0.483(0.089)	0.58
8	0.30469(0.00031)	0.443(0.087)	0.5

Table B.28: Matrix Bayesian fit to the $^3S_1$ channel with binned data.

n_{exp}	aE_0	aE_1	Q
4	0.7543(0.0075)	1.129(0.013)	0.0088
5	0.7453(0.0097)	0.967(0.079)	0.084
6	0.751(0.015)	0.973(0.077)	0.097
7	0.746(0.019)	0.94(0.11)	0.12
8	0.717(0.078)	0.83(0.083)	0.09

Table B.29: Matrix Bayesian fit to the $^1D_2$ channel.

n_{exp}	aE_0	aE_1	Q
4	0.7518(0.0079)	1.123(0.013)	0.013
5	0.7491(0.0086)	1(0.065)	0.099
6	0.75(0.022)	0.895(0.099)	0.061
7	0.245(0.052)	0.755(0.052)	0.22
8	0.247(0.052)	0.756(0.051)	0.23

Table B.30: Matrix Bayesian fit to the $^3D_{2E}$ channel.

n_{exp}	aE_0	aE_1	Q
4	0.7576(0.0084)	1.156(0.015)	0.3
5	0.7559(0.0088)	1.01(0.1)	0.56
6	0.7572(0.0082)	1(0.1)	0.59
7	0.71(0.11)	0.84(0.11)	0.56
8	0.5(0.15)	0.76(0.16)	0.64

Table B.31: Matrix Bayesian fit to the $^3D_{3A}$ channel.

3×3 **Matrix Fits**

n_{exp}	aE_0	aE_1	aE_2	Q
4	0.31881(0.00031)	0.7242(0.0018)	1.6262(0.0026)	nan
5	0.30573(0.00025)	0.6818(0.0022)	0.9587(0.0054)	4.1e-13
6	0.30513(0.00027)	0.636(0.02)	0.819(0.033)	7.8e-06
7	0.30521(0.00026)	0.6598(0.0043)	0.89(0.016)	0.019
8	0.30464(0.00044)	0.419(0.051)	0.647(0.073)	0.049
9	0.3044(0.00052)	0.41(0.046)	0.601(0.077)	0.045
10	0.30436(0.00056)	0.408(0.049)	0.609(0.082)	0.06

Table B.32: Matrix Bayesian fit to the $^3S_1$ channel.

n_{exp}	$a(loc,1)$	$a(loc,2)$	Q
4	0.31367(0.00039)	0.309884(0.0011094)	nan
5	0.30518(0.00037)	0.250321(0.00205843)	4.1e-13
6	0.30164(0.00073)	0.234389(0.0197417)	7.8e-06
7	0.30203(0.00055)	0.243619(0.00495925)	0.019
8	0.2983(0.0022)	0.0609257(0.016348)	0.049
9	0.2972(0.0027)	0.0682158(0.0207364)	0.045
10	0.2969(0.003)	0.0717079(0.019511)	0.06

Table B.33: Matrix Bayesian fit to the $^3S_1$ channel.

n_{exp}	aE_0	aE_1	aE_2	Q
4	0.27429(0.00019)	0.6725(0.0019)	0.942(0.0034)	nan
5	0.27404(0.00019)	0.67(0.0019)	0.9469(0.004)	4.4e-11
6	0.27376(0.0002)	0.6526(0.0043)	0.884(0.027)	5.9e-06
7	0.27377(0.0002)	0.6473(0.0041)	0.873(0.019)	0.12
8	0.2734(0.00031)	0.409(0.056)	0.656(0.078)	0.21
9	0.27343(0.0003)	0.407(0.061)	0.625(0.089)	0.2
10	0.2734(0.00031)	0.4(0.064)	0.6(0.1)	0.15

Table B.34: Matrix Bayesian fit to the $^1S_0$ channel.

n_{exp}	$a(loc,1)$	$a(loc,2)$	Q
4	0.33923(0.00032)	0.257299(0.00196724)	nan
5	0.33684(0.00039)	0.256759(0.00205153)	4.4e-11
6	0.33417(0.00062)	0.268066(0.00427595)	5.9e-06
7	0.33414(0.00056)	0.255499(0.00506919)	0.12
8	0.3311(0.0018)	0.0770899(0.0130068)	0.21
9	0.3313(0.0017)	0.0658921(0.0223324)	0.2
10	0.3311(0.0018)	0.0649533(0.021281)	0.15

Table B.35: Matrix Bayesian fit to the $^1S_0$ channel.

2×1 **Ratio Fits**

t_{min}/t_{max}	$\Delta a E_0$	Q
3/31	.0062262(.000456)	0.000
4/31	.0076718(.000111)	0.000
5/31	.0079874(.000061)	0.000
6/31	.0081576(.000044)	0.000
7/31	.0081958(.000039)	0.001
8/31	.0082059(.000035)	0.619
9/31	.0082435(.000036)	0.922
10/31	.0082496(.000035)	0.981
11/31	.0082586(.000036)	0.981
12/31	.0082566(.000037)	0.982
13/31	.0082739(.000039)	0.984
14/31	.0082637(.000040)	0.986
15/31	.0082636(.000041)	0.984
17/31	.0082325(.000053)	0.999
20/31	.0082343(.000069)	0.997
21/31	.0082585(.000171)	0.994

Table B.36: Standard vector fit to the $^3S_1$ kinetic mass with $(a\mathbf{p})^2 = 1$.

t_{min}/t_{max}	ΔaE_0	Q
9/31	.0165464(.000048)	0.000
10/31	.0165270(.000052)	0.000
11/31	.0165084(.000056)	0.000
12/31	.0164927(.000078)	0.984
13/31	.0165283(.000082)	0.985
14/31	.0165066(.000084)	0.986
15/31	.0165214(.000082)	0.991
16/31	.0165274(.000077)	0.958
17/31	.0164466(.000108)	0.999
19/31	.0164660(.000093)	0.996
20/31	.0164332(.000099)	0.996
22/31	.0164411(.000137)	1.000
23/31	.0165001(.000154)	1.000
24/31	.0165074(.000233)	0.998
26/31	.0165434(.000353)	0.991

Table B.37: Standard vector fit to the $^3S_1$ kinetic mass with $(a\mathbf{p})^2 = 2$.

t_{min}/t_{max}	ΔaE_0	Q
9/31	.0247973(.000075)	0.000
10/31	.0247680(.000080)	0.000
12/31	.0247087(.000124)	0.985
13/31	.0247626(.000131)	0.984
14/31	.0247286(.000133)	0.985
15/31	.0247559(.000130)	0.990
16/31	.0247634(.000123)	0.958
17/31	.0246272(.000176)	0.999
21/31	.0245829(.000169)	0.993
22/31	.0246196(.000225)	1.000
23/31	.0247192(.000330)	1.000
24/31	.0247146(.000273)	0.998
26/31	.0247341(.000274)	0.996

Table B.38: Standard vector fit to the ${}^3S_1$ kinetic mass with $(a\mathbf{p})^2 = 3$.

t_{min}/t_{max}	ΔaE_0	Q
9/31	.0329602(.000103)	0.000
10/31	.0329277(.000111)	0.000
12/31	.0328393(.000174)	0.976
13/31	.0329151(.000183)	0.975
14/31	.0328635(.000186)	0.979
15/31	.0328955(.000183)	0.984
17/31	.0327157(.000258)	0.997
18/31	.0328118(.000197)	0.991
21/31	.0327004(.000241)	0.950
22/31	.0327493(.000309)	0.996
23/31	.0329512(.000550)	0.995
24/31	.0329698(.000802)	0.982
26/31	.0330755(.000895)	0.942

Table B.39: Standard vector fit to the $^3S_1$ kinetic mass with $(a\mathbf{p})^2 = 4$.

t_{min}/t_{max}	ΔaE_0	Q
9/31	.0411806(.000134)	0.000
11/31	.0410360(.000224)	0.975
12/31	.0410133(.000229)	0.978
13/31	.0411060(.000242)	0.975
14/31	.0410401(.000247)	0.978
15/31	.0410930(.000241)	0.984
17/31	.0408270(.000354)	0.997
18/31	.0409703(.000261)	0.992
21/31	.0407971(.000321)	0.954
22/31	.0408759(.000430)	0.996
23/31	.0410922(.000649)	0.994
24/31	.0410994(.000871)	0.979

Table B.40: Standard vector fit to the ${}^3S_1$ kinetic mass with $(a\mathbf{p})^2 = 5$.

t_{min}/t_{max}	ΔaE_0	Q
4/31	.0453840(.000659)	0.000
9/31	.0493880(.000166)	0.000
11/31	.0491994(.000284)	0.973
12/31	.0491719(.000291)	0.975
13/31	.0492809(.000310)	0.968
14/31	.0492016(.000315)	0.971
15/31	.0492811(.000307)	0.980
17/31	.0489175(.000462)	0.995
21/31	.0488606(.000414)	0.945
22/31	.0489494(.000562)	0.993
23/31	.0492248(.000812)	0.990
24/31	.0490025(.000525)	0.956
26/31	.0493390(.000826)	0.864
27/31	.0493018(.000713)	0.745

Table B.41: Standard vector fit to the ${}^3S_1$ kinetic mass with $(a\mathbf{p})^2 = 6$.

t_{min}/t_{max}	ΔaE_0	Q
8/31	.0663444(.000217)	0.000
9/31	.0656849(.000238)	0.000
12/31	.0653657(.000431)	0.955
13/31	.0655129(.000467)	0.938
14/31	.0653951(.000473)	0.942
15/31	.0655310(.000460)	0.956
17/31	.0650008(.000675)	0.978
20/31	.0649851(.000591)	0.881
21/31	.0648966(.000639)	0.812
22/31	.0650954(.000978)	0.955
23/31	.0653435(.000953)	0.929
26/31	.0656964(.001357)	0.587

Table B.42: Standard vector fit to the $^3S_1$ kinetic mass with $(a\mathbf{p})^2 = 8$.

t_{min}/t_{max}	ΔaE_0	Q
8/31	.0746128(.000254)	0.000
12/31	.0734903(.000516)	0.928
13/31	.0736515(.000562)	0.900
14/31	.0735255(.000568)	0.897
15/31	.0737038(.000551)	0.925
20/31	.0730155(.000719)	0.808
21/31	.0728766(.000781)	0.723
22/31	.0731553(.001392)	0.897
23/31	.0736078(.001656)	0.848
24/31	.0731543(.001019)	0.693
25/31	.0733619(.001133)	0.528
26/31	.0733264(.098734)	0.550

Table B.43: Standard vector fit to the $^3S_1$ kinetic mass with $(a\mathbf{p})^2 = 9$.

t_{min}/t_{max}	ΔaE_0	Q
5/31	.1908982(.010038)	0.000
10/31	.0977170(.000753)	0.792
11/31	.0977884(.000792)	0.755
12/31	.0977227(.000824)	0.737
13/31	.0979282(.000908)	0.665
14/31	.0977758(.000923)	0.632
15/31	.0980816(.000962)	0.652
17/31	.0981070(.000937)	0.513
20/31	.0969717(.001230)	0.411
21/31	.0967024(.001356)	0.309
23/31	.0962561(.117817)	0.589
24/31	.0971718(.001840)	0.242
25/31	.0973902(.002070)	0.133

Table B.44: Standard vector fit to the $^3S_1$ kinetic mass with $(a\mathbf{p})^2 = 12$.

B.5 MILC $m_l = 0.02$

2×2 **Matrix Fits**

n_{exp}	aE_0	aE_1	Q
2	0.30191(0.00025)	0.6952(0.0031)	9.80909e-45
3	0.3017(0.00026)	0.6975(0.0038)	1.4e-17
4	0.30113(0.00027)	0.649(0.008)	0.025
5	0.30089(0.00036)	0.453(0.079)	0.028
6	0.30088(0.00037)	0.455(0.079)	0.035
7	0.30083(0.00041)	0.433(0.07)	0.033
8	0.30081(0.00044)	0.421(0.07)	0.032

Table B.45: Matrix Bayesian fit to the $^3S_1$ channel.

n_{exp}	aE_0	aE_1	Q
2	0.27095(0.0002)	0.6889(0.0033)	1.37327e-45
3	0.2709(0.0002)	0.6879(0.0037)	4.7e-15
4	0.27054(0.00021)	0.6395(0.0077)	0.13
5	0.27054(0.00021)	0.638(0.015)	0.15
6	0.27032(0.00029)	0.418(0.078)	0.19
7	0.27026(0.00032)	0.403(0.07)	0.18
8	0.27025(0.00034)	0.395(0.071)	0.17

Table B.46: Matrix Bayesian fit to the $^1S_0$ channel.

n_{exp}	aE_0	aE_1	Q
2	0.5896(0.002)	0.8737(0.0053)	4.4e-14
3	0.5658(0.0084)	0.77(0.057)	3.9e-11
4	0.5695(0.0039)	0.791(0.015)	0.0057
5	0.5693(0.0047)	0.79(0.023)	0.0071
6	0.5689(0.005)	0.788(0.034)	0.0077
7	0.557(0.018)	0.67(0.065)	0.0054
8	0.558(0.018)	0.671(0.067)	0.0058

Table B.47: Matrix Bayesian fit to the ${}^1P_1$ channel.

n_{exp}	aE_0	aE_1	Q
4	0.5526(0.0034)	0.787(0.015)	0.088
5	0.5524(0.0039)	0.784(0.023)	0.1
6	0.552(0.0042)	0.78(0.033)	0.11
7	0.542(0.014)	0.671(0.074)	0.084
8	0.522(0.041)	0.615(0.051)	0.066

Table B.48: Matrix Bayesian fit to the ${}^3P_0$ channel.

n_{exp}	aE_0	aE_1	Q
4	0.5794(0.0042)	0.806(0.015)	0.039
5	0.5794(0.0051)	0.803(0.026)	0.043
6	0.5789(0.0052)	0.801(0.033)	0.046
7	0.5785(0.0054)	0.795(0.04)	0.048
8	0.572(0.013)	0.713(0.088)	0.037

Table B.49: Matrix Bayesian fit to the ${}^3P_{2E}$ channel.

3×3 Matrix Fits

n_{exp}	aE_0	aE_1	aE_2	Q
4	0.30196(0.00024)	0.6722(0.0023)	0.9557(0.0033)	0
5	0.30183(0.00024)	0.6746(0.0023)	0.9598(0.0054)	4e-19
6	0.3013(0.00025)	0.6624(0.005)	0.988(0.012)	2e-08
7	0.30116(0.00025)	0.6506(0.0042)	0.873(0.02)	0.04
8	0.30111(0.00026)	0.624(0.031)	0.765(0.075)	0.031
9	0.30115(0.00026)	0.49(0.08)	0.65(0.11)	0.047
10	0.30094(0.00036)	0.434(0.073)	0.61(0.11)	0.035

Table B.50: Matrix Bayesian fit to the $^3S_1$ channel.

n_{exp}	$a(loc,1)$	$a(loc,2)$	Q
4	0.30266(0.00035)	0.234367(0.00193649)	0
5	0.30204(0.00036)	0.25012(0.00203506)	4e-19
6	0.29858(0.00059)	0.25893(0.00335654)	2e-08
7	0.29825(0.00058)	0.239582(0.00479502)	0.04
8	0.29811(0.00061)	0.194964(0.0587451)	0.031
9	0.2982(0.00065)	-0.000613433(0.0258167)	0.047
10	0.2969(0.0016)	-0.0370739(0.0399914)	0.035

Table B.51: Matrix Bayesian fit to the $^3S_1$ channel.

n_{exp}	aE_0	aE_1	aE_2	Q
4	0.27105(0.00019)	0.659(0.002)	0.9281(0.0033)	0
5	0.27097(0.00019)	0.66(0.002)	0.9419(0.004)	5.6e-23
6	0.27053(0.0002)	0.6375(0.004)	0.931(0.011)	2.9e-06
7	0.27055(0.0002)	0.6326(0.004)	0.83(0.033)	0.041
8	0.27051(0.0002)	0.576(0.075)	0.661(0.085)	0.02
9	0.27033(0.00028)	0.408(0.078)	0.62(0.11)	0.023
10	0.27026(0.00034)	0.368(0.056)	0.632(0.08)	0.055

Table B.52: Matrix Bayesian fit to the $^1S_0$ channel.

n_{exp}	$a(loc, 1)$	$a(loc, 2)$	Q
4	0.33527(0.00033)	0.249838(0.00193119)	0
5	0.33304(0.00039)	0.252932(0.00201999)	5.6e-23
6	0.32992(0.00056)	0.253466(0.0040749)	2.9e-06
7	0.3298(0.00057)	0.245609(0.00423288)	0.041
8	0.32967(0.00066)	0.13225(0.137903)	0.02
9	0.328(0.0015)	0.0505973(0.0320092)	0.023
10	0.3273(0.0021)	0.0518274(0.017661)	0.055

Table B.53: Matrix Bayesian fit to the $^1S_0$ channel.

2×1 **Ratio Fits**

t_{min}/t_{max}	ΔaE_0	Q
3/31	.0026259(.002039)	0.000
4/31	.0071656(.000323)	0.000
5/31	.0079731(.000091)	0.000
6/31	.0082144(.000054)	0.000
7/31	.0082887(.000044)	0.000
8/31	.0083123(.000041)	0.017
9/31	.0083237(.000040)	0.025
10/31	.0083317(.000038)	0.178
11/31	.0083304(.000038)	0.211
12/31	.0082985(.000040)	0.385
13/31	.0083026(.000039)	0.476
14/31	.0083060(.000040)	0.382
15/31	.0083009(.000042)	0.304
16/31	.0082919(.000053)	0.277
17/31	.0083078(.000039)	0.193
18/31	.0082957(.000041)	0.296
19/31	.0082974(.000043)	0.229
20/31	.0084573(.000278)	0.487

Table B.54: Standard vector fit to the $^3S_1$ kinetic mass with $(a\mathbf{p})^2 = 1$.

B.6 MILC $m_l = 0.03$

2×2 **Matrix Fits**

n_{exp}	aE_0	aE_1	Q
4	0.29826(0.00028)	0.631(0.014)	0.69
5	0.29809(0.00035)	0.476(0.083)	0.66
6	0.29808(0.00036)	0.476(0.083)	0.68
7	0.29809(0.00036)	0.475(0.083)	0.69
8	0.2918(0.0099)	0.3084(0.0075)	0.11

Table B.55: Matrix Bayesian fit to the ${}^3S_1$ channel.

n_{exp}	aE_0	aE_1	Q
4	0.26866(0.00021)	0.623(0.013)	0.38
5	0.26859(0.00025)	0.443(0.086)	0.36
6	0.26858(0.00025)	0.445(0.084)	0.39
7	0.26858(0.00025)	0.445(0.084)	0.4
8	0.26858(0.00025)	0.445(0.085)	0.4

Table B.56: Matrix Bayesian fit to the ${}^1S_0$ channel.

n_{exp}	aE_0	aE_1	Q
4	0.5601(0.0057)	0.782(0.034)	0.73
5	0.5604(0.0057)	0.786(0.035)	0.73
6	0.5602(0.0058)	0.786(0.035)	0.73
7	0.533(0.033)	0.643(0.066)	0.57
8	0.523(0.045)	0.634(0.05)	0.69

Table B.57: Matrix Bayesian fit to the $^1P_1$ channel.

3×3 **Matrix Fits**

n_{exp}	aE_0	aE_1	aE_2	Q
4	0.31218(0.0003)	0.7169(0.0016)	0.9949(0.0057)	nan
5	0.29931(0.00024)	0.6661(0.0023)	1.5706(0.0029)	2e-24
6	0.29877(0.00025)	0.6528(0.0057)	0.9309(0.0078)	1.6e-06
7	0.29849(0.00026)	0.6275(0.0089)	0.874(0.019)	0.0062
8	0.2984(0.00027)	0.615(0.022)	0.865(0.03)	0.006
9	0.29852(0.00026)	0.615(0.018)	0.79(0.061)	5.4e-06
10	0.29837(0.00028)	0.601(0.041)	0.628(0.045)	0.0086

Table B.58: Matrix Bayesian fit to the $^3S_1$ channel.

n_{exp}	$a(loc,1)$	$a(loc,2)$	Q
4	0.30721(0.00038)	0.311234(0.000935028)	nan
5	0.29906(0.00035)	0.242195(0.00205698)	2e-24
6	0.29554(0.00057)	0.254284(0.00356573)	1.6e-06
7	0.29447(0.00062)	0.224139(0.0108955)	0.0062
8	0.29382(0.00076)	0.220168(0.027831)	0.006
9	0.29478(0.00064)	0.146702(0.130903)	5.4e-06
10	0.29375(0.00092)	0.188795(0.0695487)	0.0086

Table B.59: Matrix Bayesian fit to the $^3S_1$ channel.

n_{exp}	aE_0	aE_1	aE_2	Q
4	0.26951(0.00019)	0.6558(0.0019)	0.9288(0.0032)	0
5	0.26937(0.00019)	0.6545(0.0019)	0.9317(0.0038)	3.5e-26
6	0.26906(0.00019)	0.6407(0.0032)	0.9184(0.0067)	7.3e-13
7	0.26885(0.0002)	0.6216(0.0062)	0.826(0.029)	0.0013
8	0.26868(0.00021)	0.504(0.044)	0.619(0.062)	0.017
9	0.26873(0.0002)	0.598(0.027)	0.718(0.071)	0.013
10	0.26868(0.00021)	0.501(0.042)	0.605(0.061)	0.017

Table B.60: Matrix Bayesian fit to the $^1S_0$ channel.

n_{exp}	$a(loc,1)$	$a(loc,2)$	Q
4	0.33237(0.00031)	0.250231(0.0018734)	0
5	0.32965(0.00039)	0.248061(0.00203199)	3.5e-26
6	0.32692(0.00052)	0.243799(0.00374693)	7.3e-13
7	0.32655(0.00055)	0.245891(0.00587783)	0.0013
8	0.32515(0.00083)	0.0273078(0.0284838)	0.017
9	0.32576(0.0007)	0.204644(0.0479708)	0.013
10	0.3253(0.0008)	0.0257371(0.0274137)	0.017

Table B.61: Matrix Bayesian fit to the $^1S_0$ channel.

2×1 **Ratio Fits**

t_{min}/t_{max}	ΔaE_0	Q
4/31	.0039649(.002288)	0.000
5/31	.0076301(.000229)	0.000
6/31	.0080733(.000087)	0.000
7/31	.0082108(.000055)	0.000
8/31	.0082818(.000043)	0.041
9/31	.0083015(.000038)	0.691
10/31	.0082947(.000037)	0.828
11/31	.0083091(.000037)	0.843
12/31	.0083253(.000038)	0.872
13/31	.0083339(.000038)	0.892
15/31	.0083434(.000042)	0.903
16/31	.0083611(.000048)	0.913
18/31	.0083534(.000040)	0.782
19/31	.0083622(.000043)	0.706

Table B.62: Standard vector fit to the $^3S_1$ kinetic mass with $(a\mathbf{p})^2 = 1$.

B.7 MILC $m_l = 0.05$

2×2 **Matrix Fits**

n_{exp}	aE_0	aE_1	Q
2	0.29586(0.00035)	0.6802(0.004)	9e-21
3	0.29529(0.00038)	0.642(0.033)	9e-09
4	0.29533(0.00038)	0.641(0.023)	0.0074
5	0.29533(0.00041)	0.473(0.095)	0.0062
6	0.29522(0.00043)	0.52(0.11)	0.0081
7	0.2906(0.0091)	0.3009(0.006)	2e-07
8	0.29525(0.00042)	0.425(0.081)	0.0065

Table B.63: Matrix Bayesian fit to the $^3S_1$ channel.

n_{exp}	aE_0	aE_1	Q
2	0.26664(0.00027)	0.6742(0.0042)	3.3e-20
3	0.26627(0.00029)	0.632(0.032)	1.5e-08
4	0.2664(0.00029)	0.64(0.019)	0.024
5	0.26627(0.00032)	0.499(0.091)	0.024
6	0.26628(0.00032)	0.503(0.099)	0.029
7	0.26637(0.0003)	0.47(0.1)	0.032
8	0.26626(0.00035)	0.389(0.076)	0.028

Table B.64: Matrix Bayesian fit to the $^1S_0$ channel.

n_{exp}	aE_0	aE_1	Q
2	0.5773(0.0028)	0.8516(0.0065)	3.1e-05
3	0.545(0.013)	0.731(0.056)	0.0021
4	0.5584(0.0061)	0.814(0.027)	0.014
5	0.223(0.064)	0.558(0.066)	0.022
6	0.23(0.063)	0.54(0.068)	0.021
7	0.233(0.063)	0.533(0.074)	0.014
8	0.224(0.066)	0.542(0.07)	0.026

Table B.65: Matrix Bayesian fit to the $^1P_1$ channel.

3×3 **Matrix Fits**

n_{exp}	aE_0	aE_1	aE_2	Q
4	0.29672(0.00033)	0.6627(0.003)	0.954(0.0044)	nan
5	0.29636(0.00033)	0.6569(0.0033)	0.9454(0.0089)	1.2e-09
6	0.29611(0.00033)	0.6512(0.0056)	0.925(0.019)	6.4e-05
7	0.29601(0.00034)	0.628(0.017)	0.795(0.06)	5.4e-05
8	0.29565(0.00038)	0.559(0.074)	0.637(0.089)	7.6e-06
9	0.29564(0.00038)	0.563(0.081)	0.661(0.098)	0.00026
10	0.29569(0.00038)	0.456(0.082)	0.59(0.11)	0.00025

Table B.66: Matrix Bayesian fit to the $^3S_1$ channel.

n_{exp}	$a(loc, 1)$	$a(loc, 2)$	Q
4	0.29573(0.00048)	0.23099(0.00245362)	nan
5	0.29492(0.00048)	0.243212(0.00269196)	1.2e-09
6	0.29232(0.00068)	0.252805(0.00339026)	6.4e-05
7	0.29176(0.00073)	0.223149(0.0274194)	5.4e-05
8	0.2891(0.0014)	0.15182(0.126055)	7.6e-06
9	0.2897(0.0013)	0.151852(0.108429)	0.00026
10	0.2898(0.0013)	-0.000821382(0.103282)	0.00025

Table B.67: Matrix Bayesian fit to the $^3S_1$ channel.

n_{exp}	aE_0	aE_1	aE_2	Q
4	0.26717(0.00025)	0.6498(0.0027)	0.9301(0.0043)	nan
5	0.26702(0.00026)	0.6481(0.0026)	0.9286(0.0051)	9e-11
6	0.26677(0.00026)	0.6329(0.0067)	0.909(0.021)	0.00062
7	0.26664(0.00027)	0.584(0.033)	0.771(0.06)	0.0022
8	0.26663(0.00027)	0.573(0.053)	0.731(0.072)	0.0034
9	0.26639(0.00034)	0.419(0.069)	0.576(0.099)	0.0023
10	0.26638(0.00034)	0.419(0.071)	0.58(0.1)	0.0052

Table B.68: Matrix Bayesian fit to the $^1S_0$ channel.

n_{exp}	$a(loc, 1)$	$a(loc, 2)$	Q
4	0.32726(0.00044)	0.246333(0.00244469)	nan
5	0.32465(0.00053)	0.246805(0.00268043)	9e-11
6	0.32256(0.00068)	0.259928(0.00431593)	0.00062
7	0.32187(0.00081)	0.194119(0.0454898)	0.0022
8	0.32172(0.0008)	0.167693(0.0787448)	0.0034
9	0.3194(0.0018)	0.0530236(0.0292727)	0.0023
10	0.3195(0.0018)	0.0519645(0.0335748)	0.0052

Table B.69: Matrix Bayesian fit to the $^1S_0$ channel.

2×1 **Ratio Fits**

t_{min}/t_{max}	ΔaE_0	Q
3/31	.0060538(.000765)	0.000
4/31	.0077516(.000175)	0.000
5/31	.0081339(.000076)	0.000
6/31	.0082447(.000054)	0.000
7/31	.0082947(.000048)	0.000
8/31	.0083317(.000045)	0.255
9/31	.0083612(.000049)	0.297
10/31	.0083342(.000047)	0.357
11/31	.0083492(.000048)	0.475
12/31	.0083893(.000056)	0.630
13/31	.0083940(.000058)	0.570
14/31	.0084155(.000059)	0.649
17/31	.0084263(.000052)	0.555
18/31	.0084186(.000055)	0.471
19/31	.0084325(.000060)	0.413

Table B.70: Standard vector fit to the $^3S_1$ kinetic mass with $(a\mathbf{p})^2 = 1$.

B.8 MILC Fine $M_b^0 = 1.95$

2×2 **Matrix Fits**

n_{exp}	aE_0	aE_1	Q
4	0.23251(0.00031)	0.4814(0.0041)	0.16
5	0.2324(0.00032)	0.478(0.006)	0.54
6	0.23232(0.0005)	0.345(0.06)	0.46
7	0.23219(0.00053)	0.322(0.055)	0.28
8	0.23212(0.00041)	0.305(0.044)	0.23

Table B.71: Matrix Bayesian fit to the ${}^3S_1$ channel.

n_{exp}	aE_0	aE_1	Q
4	0.20641(0.00024)	0.467(0.0041)	0.038
5	0.20628(0.00025)	0.465(0.0056)	0.15
6	0.20628(0.00035)	0.322(0.063)	0.11
7	0.20618(0.00042)	0.305(0.059)	0.053
8	0.2042(0.0021)	0.231(0.018)	0.014

Table B.72: Matrix Bayesian fit to the ${}^1S_0$ channel.

n_{exp}	aE_0	aE_1	Q
4	0.4268(0.0027)	0.6214(0.0046)	0.24
5	0.4234(0.0033)	0.537(0.052)	0.48
6	0.4233(0.0035)	0.545(0.052)	0.5
7	0.4232(0.0037)	0.54(0.054)	0.52
8	0.4231(0.0037)	0.542(0.053)	0.53

Table B.73: Matrix Bayesian fit to the $^1P_1$ channel.

n_{exp}	aE_0	aE_1	Q
4	0.23254(0.00033)	0.4788(0.0042)	0.046
5	0.23216(0.00039)	0.384(0.049)	0.12
6	0.23224(0.00048)	0.345(0.06)	0.2
7	0.23221(0.00047)	0.35(0.06)	0.22
8	0.2279(0.006)	0.247(0.011)	0.015

Table B.74: Matrix Bayesian fit to the $^3S_1$ channel.

3×3 **Matrix Fits**

n_{exp}	aE_0	aE_1	aE_2	Q
6	0.23372(0.00027)	0.502(0.0019)	0.727(0.012)	4.5e-08
7	0.23278(0.00029)	0.4801(0.0046)	0.699(0.013)	0.16
8	0.23251(0.00032)	0.452(0.024)	0.513(0.029)	0.29
9	0.23267(0.00031)	0.4794(0.0046)	0.583(0.045)	0.46
10	0.23249(0.00033)	0.428(0.026)	0.478(0.038)	0.31

Table B.75: Matrix Bayesian fit to the $^3S_1$ channel.

n_{exp}	$a(loc, 1)$	$a(loc, 2)$	Q
6	0.1788(0.00033)	0.142523(0.00157205)	4.5e-08
7	0.17593(0.00047)	0.137275(0.00356711)	0.16
8	0.17473(0.0007)	0.122089(0.0300264)	0.29
9	0.17551(0.00059)	0.141764(0.0067037)	0.46
10	0.17503(0.00073)	0.0629645(0.0528982)	0.31

Table B.76: Matrix Bayesian fit to the ${}^3S_1$ channel.

n_{exp}	aE_0	aE_1	aE_2	Q
6	0.20711(0.00021)	0.4869(0.0017)	0.694(0.013)	1.2e-11
7	0.20647(0.00022)	0.4645(0.0044)	0.667(0.015)	0.0055
8	0.20641(0.00024)	0.435(0.024)	0.477(0.03)	0.0081
9	0.20642(0.00024)	0.428(0.024)	0.474(0.032)	0.011
10	0.20638(0.00024)	0.433(0.025)	0.479(0.033)	0.011

Table B.77: Matrix Bayesian fit to the ${}^1S_0$ channel.

n_{exp}	$a(loc, 1)$	$a(loc, 2)$	Q
6	0.21405(0.00036)	0.159324(0.00165231)	1.2e-11
7	0.21152(0.00046)	0.150529(0.00416223)	0.0055
8	0.21096(0.00064)	0.113462(0.0480258)	0.0081
9	0.21102(0.00067)	0.096011(0.0474616)	0.011
10	0.21079(0.00068)	0.115241(0.0509165)	0.011

Table B.78: Matrix Bayesian fit to the ${}^1S_0$ channel.

2×1 **Ratio Fits**

t_{min}/t_{max}	ΔaE_0	Q
3/31	.0063519(.000020)	0.000
4/31	.0062741(.000012)	0.000
5/31	.0060866(.000015)	0.000
6/31	.0060649(.000016)	0.000
7/31	.0060316(.000018)	0.000
8/31	.0059970(.000020)	0.339
9/31	.0059870(.000022)	0.328
10/31	.0059652(.000025)	0.514
11/31	.0059654(.000026)	0.423
12/31	.0059630(.000028)	0.337
13/31	.0059830(.000028)	0.505
14/31	.0059826(.000030)	0.405
15/31	.0060065(.000041)	0.416
16/31	.0060121(.000039)	0.417
17/31	.0060035(.000036)	0.353
18/31	.0059977(.000029)	0.232
19/31	.0060202(.000045)	0.340
20/31	.0060353(.000038)	0.351

Table B.79: Standard vector fit to the ${}^3S_1$ kinetic mass with $(a\mathbf{p})^2 = 1$.

B.9 MILC Fine $M_b^0 = 2.1$

2×2 **Matrix Fits**

n_{exp}	aE_0	aE_1	Q
4	0.23656(0.00038)	0.4803(0.0052)	0.12
5	0.23612(0.00051)	0.373(0.056)	0.12
6	0.23609(0.00062)	0.332(0.052)	0.072
7	0.23614(0.00071)	0.337(0.057)	0.091
8	0.23616(0.00068)	0.337(0.057)	0.11

Table B.80: Matrix Bayesian fit to the $^3S_1$ channel.

n_{exp}	aE_0	aE_1	Q
4	0.21132(0.00029)	0.4678(0.0051)	0.062
5	0.21105(0.00038)	0.353(0.061)	0.06
6	0.21102(0.00047)	0.327(0.061)	0.031
7	0.21109(0.0005)	0.317(0.06)	0.043
8	0.2074(0.0048)	0.228(0.012)	0.0064

Table B.81: Matrix Bayesian fit to the $^1S_0$ channel.

n_{exp}	aE_0	aE_1	Q
4	0.4275(0.0038)	0.5995(0.0073)	0.63
5	0.4279(0.004)	0.6018(0.0089)	0.68
6	0.4265(0.0055)	0.578(0.037)	0.64
7	0.4278(0.0052)	0.579(0.035)	0.66
8	0.416(0.019)	0.503(0.049)	0.53

Table B.82: Matrix Bayesian fit to the ${}^1P_1$ channel.

2×1 **Ratio Fits**

t_{min}/t_{max}	ΔaE_0	Q
5/31	.0057450(.000017)	0.000
6/31	.0057133(.000019)	0.000
7/31	.0056762(.000021)	0.000
8/31	.0056394(.000023)	0.098
9/31	.0056321(.000026)	0.411
10/31	.0056166(.000029)	0.525
11/31	.0056242(.000030)	0.499
12/31	.0056239(.000033)	0.431
13/31	.0056285(.000032)	0.456
14/31	.0056416(.000036)	0.415
16/31	.0056589(.000040)	0.407

Table B.83: Standard vector fit to the $^3S_1$ kinetic mass with $(a\mathbf{p})^2 = 1$.

B.10 MILC $m_l = 0.01$, stability parameter $n = 8$

2×2 **Matrix Fits**

n_{exp}	aE_0	aE_1	Q
4	0.2939(0.00029)	0.6454(0.0089)	0.38
5	0.29388(0.0003)	0.475(0.084)	0.38
6	0.29388(0.00029)	0.471(0.09)	0.41
7	0.29386(0.00032)	0.472(0.087)	0.42
8	0.29359(0.00045)	0.416(0.073)	0.34

Table B.84: Matrix Bayesian fit to the $^3S_1$ channel.

n_{exp}	aE_0	aE_1	Q
4	0.26225(0.00021)	0.6352(0.0088)	0.55
5	0.2622(0.00024)	0.448(0.091)	0.52
6	0.2622(0.00025)	0.45(0.091)	0.55
7	0.26222(0.00021)	0.448(0.095)	0.59
8	0.26212(0.00029)	0.404(0.087)	0.47

Table B.85: Matrix Bayesian fit to the $^1S_0$ channel.

n_{exp}	aE_0	aE_1	Q
4	0.5726(0.0039)	0.807(0.013)	0.6
5	0.5732(0.0036)	0.808(0.014)	0.63
6	0.548(0.032)	0.644(0.052)	0.49
7	0.538(0.058)	0.627(0.056)	0.39
8	0.535(0.072)	0.618(0.055)	0.41

Table B.86: Matrix Bayesian fit to the $^1P_1$ channel.

3×3 **Matrix Fits**

n_{exp}	aE_0	aE_1	aE_2	Q
4	0.29528(0.00025)	0.6732(0.0022)	0.9528(0.0033)	0
5	0.29489(0.00025)	0.6708(0.0023)	0.9479(0.0054)	1.8e-13
6	0.29428(0.00027)	0.624(0.019)	0.806(0.032)	7e-06
7	0.29434(0.00026)	0.6473(0.0049)	0.88(0.016)	0.016
8	0.29407(0.00028)	0.525(0.045)	0.646(0.062)	0.006
9	0.29396(0.00031)	0.556(0.054)	0.641(0.075)	0.00056
10	0.29385(0.00032)	0.523(0.05)	0.599(0.068)	0.0066

Table B.87: Matrix Bayesian fit to the $^3S_1$ channel.

n_{exp}	$a(loc, 1)$	$a(loc, 2)$	Q
4	0.309(0.00035)	0.243985(0.00202806)	0
5	0.3079(0.00037)	0.253762(0.00210414)	1.8e-13
6	0.30427(0.00073)	0.236533(0.0198848)	7e-06
7	0.30466(0.00057)	0.246143(0.00545971)	0.016
8	0.30285(0.00084)	-0.0440343(0.0491545)	0.006
9	0.3022(0.0011)	0.143705(0.101967)	0.00056
10	0.3018(0.0012)	0.111288(0.101304)	0.0066

Table B.88: Matrix Bayesian fit to the $^3S_1$ channel.

n_{exp}	aE_0	aE_1	aE_2	Q
4	0.26299(0.00019)	0.6609(0.0019)	0.9279(0.0034)	nan
5	0.26275(0.00019)	0.6585(0.0019)	0.9339(0.004)	7.4e-11
6	0.26254(0.00019)	0.6486(0.0032)	0.9381(0.0062)	4.6e-05
7	0.26236(0.0002)	0.597(0.026)	0.705(0.034)	0.045
8	0.26233(0.00021)	0.502(0.049)	0.651(0.066)	0.19
9	0.26227(0.00021)	0.567(0.051)	0.645(0.07)	0.061
10	0.26228(0.00022)	0.484(0.046)	0.602(0.074)	0.12

Table B.89: Matrix Bayesian fit to the $^1S_0$ channel.

n_{exp}	$a(loc,1)$	$a(loc,2)$	Q
4	0.34341(0.00032)	0.262126(0.00202014)	nan
5	0.34098(0.00039)	0.261199(0.00212281)	7.4e-11
6	0.33919(0.00046)	0.258644(0.00362312)	4.6e-05
7	0.33741(0.0007)	0.234007(0.0383895)	0.045
8	0.33682(0.00092)	0.107059(0.0336827)	0.19
9	0.33665(0.00088)	0.192492(0.0836821)	0.061
10	0.3364(0.0011)	0.0846296(0.0475811)	0.12

Table B.90: Matrix Bayesian fit to the ${}^1S_0$ channel.

1×1 **Ratio Fits**

t_{min}/t_{max}	ΔaE_0	Q
3/31	0.008996(13)	0.00
4/31	0.008748(15)	0.00
5/31	0.008581(17)	3.40e-62
6/31	0.008466(18)	1.12e-16
7/31	0.008407(20)	2.24e-08
8/31	0.008357(22)	1.17e-04
9/31	0.008305(24)	0.63
10/31	0.008288(25)	0.81
11/31	0.008266(27)	0.97
12/31	0.008259(29)	0.96
13/31	0.008239(30)	0.99
14/31	0.008248(33)	0.99
15/31	0.008244(35)	0.99

Table B.91: Standard vector fit to the ${}^3S_1$ kinetic mass with $(a\mathbf{p})^2 = 1$.

Bibliography

[1] F. Mandl and G. Shaw, *Quantum Field Theory*, John Wiley and Sons, 1984

[2] D. Bailin and A. Love, *Introduction to Gauge Field Theory*, Adam Hilger, Bristol, 1986

[3] Y. Nir, *CP Violation*, SUSSP55 Proceedings 2001, hep-ph/0109090

[4] Y. Nir, *CP Violation: the CKM matrix and new physics*, 2002, hep-ph/0208080

[5] Online CLEO-c Project Description, *http://www.lns.cornell.edu/public/CLEO/spoke/CLEOc/ProjDesc.html.*

[6] R. S. Galik *et al.*, *CLEO and QCD: from Beauty to Charm*, Nucl.Phys.B.Proc.Suppl.119:22,2003

[7] R.P. Feynman, *Space-time approach to nonrelativistic quantum mechanics*, Rev.Mod.Phys.20:367-387,1948

[8] M.E. Peskin & D.V. Schroeder, *An Introduction to Quantum Field Theory*, Addison Wedley, 1995

[9] M. Kaku, *Quantum Field Theory - A Modern Introduction*, Oxford University Press 1993

[10] Jonathan L. Rosner, *The standard model in 2001*, SUSSP55 Proceedings 2001 hep-ph/0108195

[11] P.B. Schwinberg *et al.*, *New comparison of the positron and electron g factors*, Phys.Rev.Lett.47:1679-1682,1981

[12] R.M. Carey *et al.*, *New measurement of the anomalous magnetic moment of the positive muon*, Phys.Rev.Lett.82:1632-1635,1999

[13] Kenneth G. Wilson *et al.*, *Confinement of quarks*, Phys.Rev.D10:2445-2459,1974

[14] I. Montvay and G. Münster, *Quantum Fields on a Lattice*, Cambridge University Press, Cambridge, 1997

[15] C. Davies, *Lattice QCD*, SUSSP55 Proceedings 2001 hep-ph/0205181

[16] Heinz J. Rothe, *Lattice Gauge Theories: An Introduction*, World Scientific Lecture Notes in Physics - Vol.43, 1992

[17] Rajan Gupta, *Introduction to lattice QCD: course*, Lectures given at Les Houches Summer School in Theoretical Physics, hep-lat/9807028

[18] Massimo Di Pierro, *From Monte Carlo integration to lattice quantum chromodynamics: an introduction*, GSA Summer School proceedings, 2000 hep-lat/0009001

[19] K. Symanzik, *Continuum limit and improved action in lattice theories*, Nucl.Phys.B226:205,1983

[20] Mark G. Alford *et al.*, *Lattice QCD on small computers*, Phys.Lett.B361:87-94,1995 hep-lat/9507010

[21] G.Peter Lepage & Paul B. Mackenzie, *On the viability of lattice perturbation theory*, Phys.Rev.D48:2250-2264,1993 hep-lat/9209022

[22] Peter Lepage, *Lattice QCD for Novices*, lecture notes 1998

[23] Norman H. Shakespeare and Howard D. Trottier, *Mean link versus average plaquette tadpoles in lattice NRQCD*, Nucl.Phys.Proc.Suppl.73:342-344,1999 hep-lat/9809116

[24] N. Metropolis *et al. Equation of State Calculations by Fast Computing Machines* J.Chem.Phys.21:1087,1953

[25] Kenneth G. Wilson, *Quarks and strings on a lattice*, Subnucl.Phys.1975:0069

[26] Holger Bech Nielsen, M. Ninomiya, *No go theorem for regularizing chiral fermions*, Phys.Lett.B105:219,1981

[27] B. Sheikholeslami, R. Wohlert, *Improved continuum limit lattice action for QCD with Wilson fermions*, Nucl.Phys.B259:572,1985

[28] Martin Luscher, *Advanced lattice QCD*, Talk given at Les Houches Summer School in Theoretical Physics, hep-lat/9802029

[29] Martin Luscher, *Nonperturbative determination of the axial current normalization constant in $\mathcal{O}(a)$ improved lattice QCD*, Nucl.Phys.B491:344-364,1997, hep-lat/9611015

[30] Leonard Susskind, *Lattice fermions*, Phys.Rev.D16:3031-3039,1977

[31] G.Peter Lepage, *Flavor symmetry restoration and Symanzik improvement for staggered quarks*, Phys.Rev.D59:074502,1999 hep-lat/9809157

[32] S. Naik, Nucl.Phys.B316:238,1989 hep-lat/0110175

[33] S. Gottlieb *et al.*, *Hybrid molecular dynamics algorithms for the numerical simulation of quantum chromodynamics*, Phys.Rev.D35:2531-2542,1987

[34] M.A. Clark *et al.*, *Comparing the R algorithm and RHMC for staggered fermions*, hep-lat/0209035

[35] William A. Bardeen *et al.*, *Light quarks, zero modes, and exceptional configurations*, Phys.Rev.D57:1633-1641,1998 hep-lat/9705008

[36] Christine Davies, *The heavy hadron spectrum*, 36 IUKT proceedings, 1997 hep-ph/9710394

[37] B.R. Martin and G. Shaw, *Particle Physics*, John Wiley and Sons, 1992

[38] W.R. Innes *et al.*, *Observation of structure in the Upsilon region*, Phys.Rev.Lett.39:1240,1977, Erratum-ibid.39:1640,1977

[39] F. Pauss *et al.*, *Observation of chi - b production in the exclusive reaction Upsilon-prime → gamma chi - b → gamma gamma Upsilon → gamma gamma (e+ e- or mu+ mu-)*, Phys.Lett.B130:439,1983

[40] G. Eigen *et al. Evidence for chi(b)-prime production in the exclusive reaction Upsilon-prime-prime → gamma chi(b)-prime → (gamma gamma Upsilon-prime or gamma gamma Upsilon)*, Phys.Rev.Lett.49:1616-1619,1982

[41] K. Han *et al.*, *Observation of p wave b anti-b bound states*, Phys.Rev.Lett.49:1612-1616,1982

[42] S.E. Csorna *et al.*, *First observation of Upsilon (1d) states*, ICHEP 2002 hep-ex/0207060

[43] B.A. Thacker and G.Peter Lepage, *Heavy quark bound states in lattice QCD*, Phys.Rev.D43:196-208,1991

[44] Waikwok Kwong *et al.*, *Heavy quark systems*, Ann.Rev.Nucl.Part.Sci.37:325,1987

[45] G. S. Bali, K. Schilling and A. Wachter, *Complete* $\mathcal{O}(v^2)$ *corrections to the static interquark potential from SU(3) gauge theory*, Wuppertal preprint WUB 97-11, hep-lat/9703019

[46] F. Hussain *et al*, *An Introduction to the Heavy Quark Effective Theory* Trieste HEP Cosmology 1994:0045-115, hep-ph/9502241

[47] Michele Della Morte *et al*, *Lattice HQET with exponentially improved statistical precision*, hep-lat/0307021

[48] *Massive fermions in lattice gauge theory*, By Aida X. El-Khadra (Illinois U., Urbana), Andreas S. Kronfeld, Paul B. Mackenzie (Fermilab). FERMILAB-PUB-96-074-T, ILL-TH-96-1, Apr 1996. 54pp. Published in Phys.Rev.D55:3933-3957,1997 e-Print Archive: hep-lat/9604004

[49] X. Liao, T. Manke, *Relativistic bottomonium spectrum from anisotropic lattices*, Phys.Rev.D65:074508,2002, hep-lat/0111049

[50] X. Liao, T. Manke, *Excited charmonium spectrum from anisotropic lattices*, hep-lat/0210030

[51] G. Peter Lepage *et al.*, *Improved Nonrelativistic QCD for Heavy Quark Physics*, Phys.Rev.D46:4052-4067,1992 hep-lat/9205007

[52] C Itzykson & J.B. Zuber, *Quantum Field Theory*, McGraw-Hill, 1980

[53] C. T. H. Davies and B. A. Thacker, *Heavy Quark Renormalization Parameters in Non-relativistic QCD,* Phys.Rev.D45,915,1992

[54] Laurence Marcantonio, *Unquenched Lattice Upsilon Spectroscopy*, Phd. Thesis , University of Glasgow , 2001

[55] C. T. H. Davies *et al.*, *Precision Upsilon spectroscopy from nonrelativistic lattice QCD*, Phys.Rev.D50:6963-6977,1994 hep-lat/9406017

[56] C.T.H. Davies *et al.*, *Scaling of the Upsilon spectrum in lattice NRQCD*, Phys.Rev.D58:054505,1998 hep-lat/9802024

[57] B.H. Bransden and C.J. Joachain, *Introduction to Quantum Mechanics*, John Wiley & Sons Inc. New York, 1989

[58] S.M. Catterall *et al.*, *Radial excited states for heavy quark systems in NRQCD*, Phys.Lett.B321:246-253,1994 hep-lat/9311006

[59] Paul McCallum, *Upsilon Spectroscopy using Lattice QCD*, Phd. Thesis , University of Glasgow , 1997

[60] Press, Teukulsky, Vetterling, Flannery, *Numerical Recipies in Fortran 77*, Cambridge University Press, 1986-1992

[61] J. Shau, and D. Tu, *The Jackknife and Bootstrap*, Springer , New York, 1995

[62] G. P. Lepage *et al.*, *Constrained curve fitting*, Nucl.Phys.Proc.Suppl.106:12,2002 hep-lat/0110175

[63] C. W. Bernard *et al.*, *The QCD spectrum with three quark flavors*, Phys.Rev.D64:054506,2001 hep-lat/0104002

[64] see e.g. D.H. Perkins, *Introduction to High Energy Physics* , 4th ed. Cambridge University Press 2000

[65] A. Gray *et al.*, *The Upsilon spectrum from lattice QCD with 2+1 flavors of dynamical quarks*, Nucl.Phys.B.Proc.Suppl.119:592,2003 hep-lat/0209022

[66] R. Sommer, *A new way to set the energy scale in lattice gauge theories and its applications to the static force and alpha-s in su(2) yang-mills theory*, Nucl.Phys.B411:839-854,1994 hep-lat/9310022

[67] E. Eichten *et al.*, *Charmonium: comparison with experiment*, Phys.Rev.D21:203,1980

[68] John L. Richardson, *The heavy quark potential and the Upsilon, J/Psi systems*, Phys.Lett.B82:272,1979

[69] C.T.H. Davies, A. Gray *et al. High precision lattice QCD confronts experiment*, hep-lat/0304004

[70] Stefan Scherer, *Introduction to chiral perturbation theory*, Submitted to Adv.Nucl.Phys. hep-ph/0210398

[71] C.T.H. Davies *et al.*, *Further precise determinations of alpha-s from lattice QCD*, Phys.Rev.D56:2755-2765,1997 hep-lat/9703010

[72] Belle Collaboration, presented at FPCP Conference, Philadelphia, PA, May 16-18, 2002

[73] L. Marcantonio *et al.*, *The unquenched Upsilon spectrum*, Nucl.Phys.Proc.Suppl.94:363-366,2001 hep-lat/0011053

[74] C.T.H. Davies, private communication.

[75] C. J. Morningstar and J. Shigemitsu, *Perturbative matching of lattice and continuum heavy light currents with NRQCD heavy quarks*, Phys.Rev.D59:094504,1999 hep-lat/9810047

[76] B.D. Jones and R.M. Woloshyn, *Mesonic decay constants in lattice NRQCD*, Phys.Rev.D60:014502,1999 hep-lat/9812008

[77] C.T.H. Davies *et al.*, *A precise determination of alpha-s from lattice QCD*, Phys.Lett.B345:42-48,1995 hep-ph/9408328

[78] R.N. Mohapatra, *Supersymmetric grand unification*, Lectures at TASI 97 hep-ph/9801235

[79] C. T. H. Davies, A. Gray *et al.*, *The determination of alpha_s from lattice QCD with 2+1 flavors of dynamical quarks*, Nucl.Phys.B.Proc.Suppl.119:595,2003 hep-lat/0209122

[80] H. Trottier & Q. Mason, *Third-order perturbation theory for* α_V *and small Wilson loops for three lattice actions*, Collaboration internal notes 2003

[81] MILC, private communication.

[82] G.P. Lepage, *A New Algorithm for Adaptive Multidimensional Integration*, J.Comput.Phys.27:192,1978

[83] C.T.H. Davies *et al.*, *Renormalization of bilinears in nonrelativistic QCD*, Phys.Rev.D48:1329-1336,1993

[84] I.T. Drummond *et al.*, *One loop calculation of the renormalized anisotropy for improved anisotropic gluon actions on a lattice*, Phys.Rev.D66:094509,2002 hep-lat/0208010

[85] G. Von Hippel, Ph.D. Thesis in preparation.

[86] K. Hagiwara *et al.*, [Particle Data Group] *Review of Particle Physics*, Phys.Rev.D66:010001,2002